Title

Treatment Monitoring in Nervous System Disorders With Functional Ultrasound Imaging

Author

Agyeman, Kofi Afriyie

Publication Date

2023

UNIVERSITY OF CALIFORNIA
RIVERSIDE

Treatment Monitoring in Nervous System Disorders With Functional Ultrasound Imaging

A Dissertation submitted in partial satisfaction of
the requirements for the degree of

Doctor of Philosophy

in

Bioengineering

by

Kofi Afriyie Agyeman

March 2024

Dissertation Committee:

Dr. Vasileios Christopoulos, Chairperson
Dr. Xiaoping P. Hu
Dr. Victor Rodgers

The Dissertation of Kofi Afriyie Agyeman is approved:

Committee Chairperson

University of California, Riverside

Acknowledgments

My gratitude to the dissertation committee composed of Dr. Victor Rodgers, Dr. Xiaoping Hu, and Dr. Vasileios Christopoulos, all from the department of Bioengineering at the University of California, Riverside, for their guidance and feedback.

I would like to acknowledge the tremendous contribution of our research collaborators at the Keck School of Medicine, and the Neuro Restoration Center at the University of Southern California, USA who provided access to preclinical and clinical data.

Notably, my sincere utmost appreciation to Dr Charles Liu, Dr Darin Lee, Dr. Reggie Edgerton, and the rest of the USC medical and research team.

Thank you to Dr. Vasileios Christopoulos, my advisor, for the opportunities, guidance, and support. And to my colleagues at the Systems Neural Engineering Laboratory at the University of California, Riverside.

Gratitude to Alexis Weatherspoon my biggest cheer leader.

This dissertation is dedicated to my mother, Dr. Josephine Larbi-Apau for all the encouragement, support and being there always.

ABSTRACT OF THE DISSERTATION

Treatment Monitoring in Nervous System Disorders With Functional Ultrasound Imaging

Kofi Afriyie Agyeman

Doctor of Philosophy, Graduate Program in Bioengineering
University of California, Riverside, March 2024
Dr. Vasileios Christopoulos, Chairperson

Neurological disorders affect millions of people worldwide, with devastating health and cost burdens. Therapeutic neuromodulation has received tremendous attention due to its promise as a viable alternative for treating drug-resistant neurological conditions. While promising, clinical outcomes are sub-optimal and patient specific because the mechanisms of actions of neuromodulation remain speculative at best. Primarily because the functional architecture of the brain and spinal cord is not well understood due to intrinsic challenges associated with existing neuroimaging and monitoring modalities. Functional ultrasound imaging (fUSI) is a recently developed minimally invasive neuroimaging technique that can record blood flow dynamics at a level of sensitivity, spatial and temporal precision previously not available. Here we leverage fUSI to investigate hemodynamic responses as a proxy to neural activity modulations in the brain and spinal cord induced by drug, neurological disease, and neuromodulation. In animal preclinical studies, we find that MK-801 and ketamine NMDA antagonists cause specific spatiotemporal changes to cerebral blood volume (CBV), and subsequent MSN theta-frequency deep brain stimulation has strong effect on hippocampal CBV in a MK-801 drug induced hypoperfusion brain. In human clinical work, we predict spinal cord hemodynamic responses to epidural electrical stimulation of the spinal cord at a single trial-level, with high accuracy. Additionally, we decode bladder-pressure state – a physiological function solely from spinal cord fUSI signal acquired during filling and emptying of the bladder. Given these outcomes we extend our results to show that aberrant epileptic-seizure brain state causes distinct changes to local brain connectivity and network activity. We found a strong reduction in cross-correlation coefficients of local interictal fUSI signal acquired from neighboring healthy brain regions after surgical resection of aberrant seizure brain foci. Importantly, we demonstrate that non-invasive common peroneal nerve stimulation (PNS) disrupts local brain network-connectivity by reducing fUSI interictal signal correlation coefficients below a threshold when the PNS stimulator is turned on. Our ability to characterize and decode brain and spinal cord states in response to drug, disease, and neuromodulation in-vivo opens avenues to understand spinal cord and brain function, dysfunction, and effects of neuromodulation – ultimately vital for translational development of real-time closed-loop neurorehabilitation systems.

Table of Contents

List of Figures

to zero rapidly moving away from the electrodes, demonstrating that the volume of activation is confined within a diameter of about 1 millimeter. C) The voltage amplitude plotted along a single axis. The voltage decay profile moving away from the electrode is very similar along all three axes and the volume of activation can be modeled as a sphere. The "equivalent diameter" for the volume affected by stimulation is approximated by choosing points where the slope is approaching zero (green circles), which determines the current density generated at that location. Thresholding can also be used to visualize the points where the target voltage amplitude is maintained. The red circles label the coordinates at which an amplitude of 1 Volt or more is observed. C+ and C- labels mark the centers of the positive and negative electrodes, respectively.

2.12 Functional ultrasound imaging (fUSI) of the mouse brain. A) 3D mouse brain model with fUSI probe positioning (white bar) and ROIs – hippocampus (HPF), medial prefrontal cortex (mPFC), hypothalamus (HYT), thalamus (TLM), pallidum (PDM), and striatum (STM), superimposed onto a mean grayscale fUSI vascular map of the sagittal mouse brain. B) pD image of cerebral blood volume (CBV) in a sagittal plane (max-min normalized relative scale)

3

3.1 Surgical procedure, fUSI acquisition and epidural electrical spinal cord stimulation protocol. A) Patients undergo a T10 partial laminectomy for standard-of-care implantation of an epidural electrical spinal cord stimulator (PentaTM model 3228), under general anesthesia. B) Laminectomy and X-ray imaging of the spine lamina. A 15 MHz functional ultrasound probe (inner panel) is inserted into a sterilized cover to reduce the level of microbial contamination. The probe is mounted onto a retractor surgical arm and inserted into the lamina for fUSI. C) Functional ultrasound imaging and ESCS Protocol. Continuous fUSI recording protocol consists of 3 min (n=4) or 30 s (n=2) baseline signal acquisition, followed by acquisition during 10 cycles of ESCS consisting of 30 s stimulation ON and 30 s stimulation OFF trials. D) ESCS parameters. All patients were stimulated at 40 Hz burst-frequency with 250µs pulse-width stimulation. Patients received either 10 cycles all at 3.0 mA (n=4), or 10 cycles consisting of 5 cycles at 3.0 mA followed by 5 cycles at 4.5 mA (n=2).

3.2 Functional ultrasound imaging of the spinal cord in a transverse plane. A) Schematic representation of spinal cord fUSI through a laminar window and cross section of spinal cord anatomy. The green area illustrates approximately the field of view of fUSI acquisition in patient 1. B-G) Power Doppler-based ultrafast ultrasound image showing the transverse section of the spinal cord of patients. The field of view captures part of the anatomical vascularization of the spinal cord with the dorsal surface highlighted with white discontinuous dash lines (and dura in patient 2).

3.3 Hemodynamic response of the spinal cord induced by epidural electrical spinal cord stimulation within a trial in a typical patient. A) Spatiotemporal spinal cord blood volume change (ΔSCBV) greater than 30% relative to reference activity, color coded on the reference grayscale mean pD images at several time points starting 5 seconds before onset of the stimulation (Patient 4). The reference activity was computed as the average fUSI signal for 20 s prior to stimulation onset. B) Spinal cord temporal mean %pD signal change from trial-to-trial corresponding to pseudo global regions (activated regions with %pD signal change greater than 30%) that exhibit increase (red) and decrease (blue) in SCBV.

3.4 Statistical parametric map and event-related average waveforms (Four patients). A) Statistical map shows localized areas with significantly higher or lower SCBV with respect to reference activity during stimulation OFF (two-sided t test of area under the curve, $p < 0.05$, false discovery rate [FDR] corrected for number of pixels in image). SPM overlaid on grayscale baseline mean pD intensity images. The top panels illustrate approximately the field of view of the fUSI acquisition for each patient. B) ERA waveforms of selected regions of interest (ROIs) [as indicated with boxes and letters in SPMs – panels A] that exhibit strong increased changes of blood perfusion (red and yellow curves – red and orange boxes) or that exhibit strong decrease change of blood perfusion (blue curves – cyan boxes), after turning on the stimulator. The ERA waveforms corresponding to control ROIs that do not show significant changes in blood perfusion (gray curves – white boxes) after the stimulator is turned on are also displayed. Notice that some ROIs exhibit stronger changes of blood perfusion than others. The background grayscale vascular images in row A illustrate the average power Doppler signal of the spinal cord over the baseline acquisition. C) ERA waveforms of the pseudo-global activated pixels that exhibit strong increased changes of blood perfusion (reddish) or that exhibit strong decrease change of blood perfusion (blueish) in SPMs, after turning on the stimulator. The pseudo-global ERA waveform is determined as the mean %pD signal change across the SPM activated pixels above a threshold (z-score ≥ 0.7) with respect to the reference activity during stimulation OFF trials. D) ERA waveforms of the global SCBV changes of the 4 patients. The global SCBV is determined as percentage change in pD from reference activity of the total recorded spinal cord region recorded. The shaded regions around the curves on panels A, B and C correspond to the standard error (SEM) of the power Doppler signal change for averaged over the indicated ROIs across the 10 stimulation trials.

3.5 Spatial and temporal response to low and high ESCS current amplitudes (Two patients). A-D) Statistical parametric maps that show localized areas with significantly higher or lower SCBV with respect to reference activity during low (3.0 mA – panels A, C) or high (4.5 mA – panels B, D) ESCS (two-sided t test of area under the curve, $p < 0.05$, false discovery rate [FDR] corrected for number of pixels in image). SPMs overlaid on

cord was decoded from single trials based on a cPCA dimensionality reduction algorithm and a LDA classification model built by the training pD spinal cord imaging data with the corresponding class labels (i.e., C0: OFF stimulation, C1: ON stimulation).

3.8 Single-trial decoding of the spinal cord state. A) Average decoding accuracy across patients as a function of the amount of data used to train the classifier – i.e., time after the stimulation onset - training window. Indicated are the decoding accuracies of each patient, when 30 s of stimulation ON and 30 s of stimulation OFF data, across the 10 trials, is used for the decoding algorithm (P1=87.1, P2=73.2, P3=82.7, P4=94.4 % – point plots). B) Decoding accuracy of the spinal cord state using pD images acquired at specific time points after turning on the stimulation (with time step 1 s) as a function of the amount of data used to train the classifier (i.e., training window). For instance, we train the classifier using a set of pD images between t=1-5 s and evaluate the decoding accuracy of each second – 1s, 2s, 3s, 4s, and 5s. C) Decoding accuracy of the spinal cord state for pD images acquired between 1s and 20s after turning on the stimulator – i.e., training window of 20s. Different traces correspond to the decoding accuracy of different spatial resolutions (100 μm, 200 μm and 400 μm) of the pD images, averaged across patients (n=4) The shaded regions around the curves correspond to the standard error of the decoding accuracy curves averaged across patients. Inner panel: Mean decoding accuracy as a function of spatial resolution determined over the 100 μm resolution interval of peak accuracy (14:17 s test time instants within the training window). The mean decoding accuracies across patients over this interval were compared. The 100 μm resolution pD images perform significantly better than the 200 μm (p = 0.0463) and 400 μm (p = 0.000183) resolution images over the selected interval. D) Representative decoder weighting maps (patient 1). The top 10% most heavily weighted pixels are illustrated as a function of space and time after the stimulation onset, overlaid on grayscale mean pD baseline intensity vascular map.

3.9 Effects of mean pD intensity in single-trial decoding analysis. A) A vascular map of patient 4 with contours dividing the image into deciles of mean pD intensity. B) Mean decoding accuracy (Stimulation ON vs. Stimulation OFF) as a function of deciles (pD intensity sub-divisions) across all patients (shaded area represents standard error [SEM]). Decoding accuracy peaks around quantile 4, which mostly contains small vasculature within the spinal cord. Smaller vessels and primary unit vasculature (i.e., deciles 1 and 10, respectively) carry less information about the effect of the ESCS on spinal cord blood flow. Mean decoding accuracy of decile-ranges (1-2, 3-5, 6-8, and 9-10: smallest, small-medium, medium-large, and largest vessels). The decoding accuracy of the 3rd to 5th deciles (small-medium vessels) is significantly greater than the mean accuracy of the largest vessels – 9th to 10th deciles (p = 0.0041)

3.S.1 Statistical parametric maps without correcting for washout effects from the electrical stimulation. Statistical map shows localized areas with significantly higher SCBV during stimulation ON with respect to all 30 s of stimulation OFF reference activity (two-sided t-test of area under the curve, $p < 0.05$, false discovery rate [FDR] corrected for number of pixels in image). We do not correct for potential washout effect from the electrical stimulation – i.e., all 30 s of acquisition were used from the stimulation OFF trials.

3.S.2 Variance of pD signal during baseline periods (i.e., 6 seconds prior to stimulation onset) in pre- and post-motion correction. A) Pixelwise standard deviation in unfiltered fUSI pD intensity signal during baseline periods (patient 1) B) Pixelwise standard deviation in filtered fUSI pD intensity signal during baseline periods (patient 1). Motion correction algorithms reduce the standard deviation of the power Doppler intensity signal during baseline, indicating that most of the motion artifacts are significantly removed from the fUSI image.

3.S.3 Statistical parametric map and event-related average waveforms. A) Statistical map shows localized areas with significantly higher or lower SCBV with respect to baseline – mean of 6 s signal activity before ESCS. SPMs are overlaid on grayscale baseline mean pD intensity images. B) ERA waveforms of selected ROIs [as indicated with boxes and letters in SPMs – panels A] that exhibit strong increased changes of blood perfusion (red curves – orange boxes) or that exhibit strong decrease change of blood perfusion (blue curves – cyan boxes), after turning on the stimulator. The ERA waveforms corresponding to control ROIs that do not show significant changes in blood perfusion (gray curves – white boxes) after the stimulator is turned on are also displayed. C) Baseline and trial-to-trial ERA waveforms.

3.S.4 Patient decoding accuracy for time-data amount and vessel-content analysis. A) Data-amount analysis decoding accuracy for each patient (n=4) as a function of the amount of data used to train the classifier – i.e., time after the stimulation onset - training window. The accuracy increases with increasing data amount, peaks, and then decreases after various amounts of training window in all patients. B) Vessel-content analysis decoding accuracy (Stimulation ON vs. Stimulation OFF) as a function of deciles (pD intensity sub-divisions) for each patient (n=4). Decoding accuracy peaks around quantile 4 or 5 and then decreases in all patients. Deciles 4 and 5 mostly contain small to medium vasculatures within the spinal cord. The smaller vessels and primary unit vasculature (i.e., deciles 1 and 10, respectively) appear to carry less information about the effect of ESCS on spinal cord blood flow.

4

5.4 PNS protocol and flowchart for dynamic local connectivity modulation detection from the fUSI signal. A) Peroneal nerve stimulation protocol. A continuous fUSI recording protocol consisting of 3 min baseline signal recording, followed by acquisition during 3 cycles of PNS consisting of 2 min stimulation ON and 1 min stimulation OFF trials was utilized. This is followed by an additional 1 min of fUSI recording after offset of stimulation. B) fUSI brain images acquired from aberrant seizure onset regions during baseline, stimulation OFF and stimulation ON were time-aligned and discretized into equal 6 x 6 ROIs to extract mean pD signals across time. Using a sliding window, 180 s long with 10 s steps, changes to the mean and medium cross-correlation coefficients were assessed between the ROIs for each step.

5.5 Statistical parametric map and event-related average waveforms. A) Statistical map shows localized areas with significantly higher or lower CBV with respect to reference activity during stimulation OFF (two-sided t test of area under the curve, $p < 0.05$, FDR corrected for number of pixels in image). The SPMs are overlaid on grayscale baseline mean pD intensity images. B) ERA waveforms of the pseudo-global activated pixels in the SPMs that exhibit strong increased changes of blood perfusion (red curve) or that exhibit strong decrease change of blood perfusion (blue curve), after turning on the stimulator. The pseudo-global ERA waveform is determined as the mean %pD signal change across the SPM activated pixels above a threshold (z-score ≥ 0.6) with respect to the reference activity during stimulation OFF trials.

5.6 Dynamic local connectivity of the brain evoked by PNS (N=3). A) Representative local connectivity Pearson's cross-correlation matrix. A 36 x 36 matrix that shows the CCs for the cross-correlation calculation between the 36 ROIs in the fUSI brain image space. B) Changes of the local brain connectivity, measured as CCs over time – at each sliding window of data step. There is a drop in CCs going from baseline and PN stimulation OFF to ON trial periods below a threshold ($r < 0.5$). The image space was discretized into equal 6 x 6 ROIs in the 3D (image x time) matrix which is transformed into a 2D space consisting of each ROI's mean pD intensity signal across time. A sliding window consisting of 180 s long data, with 10 s steps, was used to derive a Pearson's cross-correlation coefficient for each section of data, at each step across time.

List of Abbreviations

DBS – Deep brain stimulation
TMS - Transcranial magnetic stimulation
NMDA - N-methyl-D-aspartate
MSN - Medial septal nucleus
CBV - Cerebral blood volume
i.p. – Intraperitoneal
FDA - Food and drug administration
MOA - Mechanism of action
PPS - Poly-population spiking
MK-801 – Dizocilpine
SWA - Slow wave activity
mPFC - Medial prefrontal cortex
ROI – Regions of interest
ANOVA – Analysis of variance
rmANOVA – repeated measures analysis of variance
ERA – Event related average
Fig. – Figure
ECT – Electroconvulsive therapy
RCA – Ray column array
fUSI – Functional ultrasound imaging
PBS – Phosphate buffer saline
AM- Admittance method
WM – White matter
CSF – Cerebrospinal fluid
FOV – Field of view
PRF – Pulse repetition frequency
SVD – Singular-value-decomposition
pD – Power Doppler
HPF – Hippocampus
HYT – Hypothalamus
TLM – Thalamus
PDM – Pallidum
STM – Striatum
fMRI – Functional magnetic resonance imaging
sEEG – stereoelectroencephalography
NHP – Non-human primates
ESCS – Epidural spinal cord stimulation
SCBV – Spinal cord blood volume

SPM – Statistical parametric maps
dSPM – Dynamic Statistical parametric maps
FDR – False discovery rate
SEM – Standard error
cPCA – Class-wise principal component analysis
LDA – Linear discriminant analysis
STD – Standard deviation
FBSS – Failed back surgery syndrome
USC – University of Southern California
MRI – Magnetic resonance imaging
SE – Standard error
SVM – Support vector machine
posC – Positive correlation
negC – Negative correlation
CC – Cross-correlation coefficient
all-D – All data
Optm-D – Optimum data amount
ML – Machine learning
UI – Urinary incontinence
SCI – Spinal cord injury
TSCS – Transcutaneous spinal cord stimulation
ECoG – Electrocorticography
EPhys – Electrophysiology
EEG – Electroencephalography
fNIRS – functional near-infrared spectroscopy
PET – Positron emission tomography
SNR – Signal-to-noise ratio
RBC – Red blood cells
cD – Color Doppler
RNS – Responsive neurostimulation
PNS – Peroneal nerve stimulation

Chapter 1

Introduction

1.1 Functional ultrasound imaging

Functional ultrasound imaging (fUSI) represents a fast-growing breakthrough modality for large-scale recording of neural activity that is indirectly coupled to blood flow and volume dynamics [1–3]. It is minimally invasive and provides a unique combination of great spatial coverage: ~ 10 cm, high spatiotemporal resolution: ~100 µm, up to 10 ms and sensitivity: ~ 1 mm/s velocity. The enhanced sensitivity and spatiotemporal properties of fUSI permit a closer connection to underlying neuronal signal compared to other hemodynamic methods. These properties establish fUSI potentially as a fundamental tool to investigate and unravel changes to brain and spinal cords states caused by function, stimuli, disease, chemical, and/or therapeutic neuromodulation.

1.1.1 Strengths and limitations

The capability to detect brain or spinal cord neural activation in response to stimuli or function is of vital importance to researchers and clinicians in their pursuit to unravel the fundamentals of science and mechanisms of therapeutic intervention respectively. Direct access to neuronal activation via measurement of electrical activity signals from neurons is possible with techniques such as electrophysiology (EPhys)[4–6], electroencephalography (EEG) [7,8], Electrocorticography (ECoG) [9,10], or calcium imaging [11,12]. Alternatively, by measuring hemodynamic properties in vessels in the proximity of neurons, the activity and location of neurons can be detected indirectly via neurovascular coupling utilizing acquisition modalities such as functional magnetic resonance imaging (fMRI) [13,14], functional near-infrared spectroscopy (fNIRS) [15], positron emission tomography (PET) [16,17], or photo acoustic imaging [18,19] (Fig. 1.1). While the utilization of each of these functional signal acquisition modalities are widespread in research and clinical settings, their application is dictated by strengths and limitations pertaining to their intrinsic properties – spatiotemporal resolution, sensitivity, coverage, cost, portability, invasiveness, etc. (Fig. 1.1). Although fMRI is non-invasive, enables whole brain 2D and 3D imaging and is considered the gold standard of functional neuroimaging for preclinical and clinical studies, it is not without important limitations. Its size, high cost associated with obtaining the system, operator training and operation, as well as acoustic noise during operation and its susceptibility to electromagnetic interference make its adoption prohibitive for certain preclinical or clinical applications.

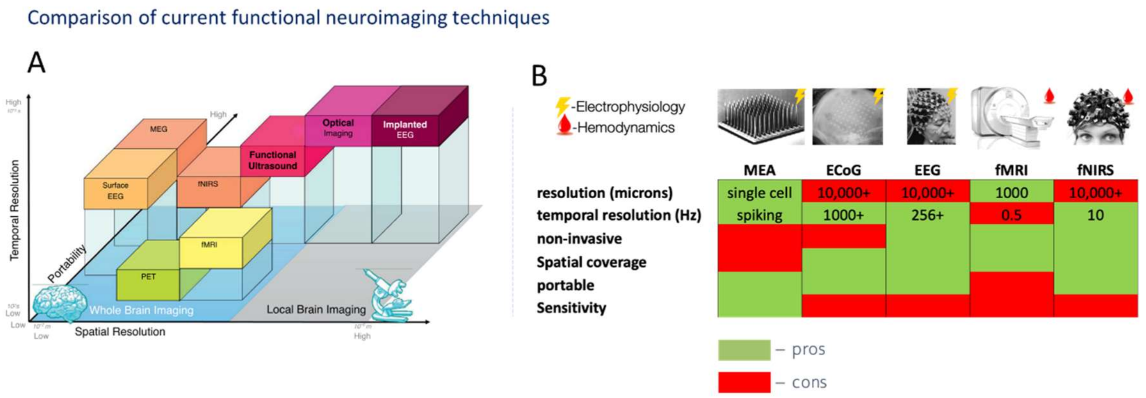

Comparison of current functional neuroimaging techniques

	MEA	ECoG	EEG	fMRI	fNIRS
resolution (microns)	🟩 single cell	🟥 10,000+	🟥 10,000+	🟩 1000	🟥 10,000+
temporal resolution (Hz)	🟩 spiking	🟩 1000+	🟩 256+	🟥 0.5	🟩 10
non-invasive	🟥	🟥	🟩	🟩	🟩
Spatial coverage	🟥	🟩	🟩	🟩	🟩
portable	🟩	🟩	🟩	🟥	🟩
Sensitivity	🟩	🟥	🟥	🟥	🟥

🟩 – pros

🟥 – cons

Figure 1.1 Functional neuroimaging modalities A) Temporal, spatial and portability comparison (Courtesy: Deffieux, et. al, [20]) of existing functional neuroimaging modalities. B) Electrophysiological (direct neural activity measurements) and hemodynamic (indirect measurement of neural activity via vascular coupling) based techniques (Courtesy: Mace E, et. al. [1]).

Thus, the development of novel neuroimaging modalities such as fUSI with its associated improvements in sensitivity, spatiotemporal and compatibility properties is imperative to address some of the challenges associated with other functional neuroimaging modalities or serve as a complimentary technique. FUSI is portable, minimally invasive and has a low cost of operation. It has been shown to be less susceptible to electromagnetic interference, a strength that enables simultaneous operation with other imaging modalities or neuromodulation stimulation devices [21,22].

1.1.2 Theory and principles

Although there is widespread utilization of conventional ultrasound in clinical settings for pre-natal assessments and investigation of blood-circulation in many important internal organs (liver, heart, kidneys, and uterus), its low signal-to-noise ratio (SNR), coupled with its low sensitivity properties, severely limits its potential application for functional neuroimaging studies. Generally, the application of conventional clinical ultrasound is restricted to potentially capturing functional changes only in major brain arteries, even with the cranial bone obstruction removed, compared to other hemodynamic-based neuroimaging techniques.

While sharing underlying principles with conventional ultrasound, fUSI is faster and approximately fifty times more sensitive. Akin to conventional doppler ultrasound, fUSI detects the motion of red blood cells (RBC) by capturing backscattered pulsatory wave transmissions from the RBCs [2,23]. Conversely, the utilization of planar waves in fUSI in contrast to focused waves in conventional clinical ultrasound, enables faster acquisition rates leading to signals with better resolution and signal-to-contrast ratios – as planar waves cover entire 2D imaging planes in a single transmission, compared to focused waves that must be transmitted sequentially across an imaging plane to generate a single 2D image (Fig. 1.2) [2].

Specifically, to acquire a fUSI image, a sequence of ultrafast plane sound waves is transmitted at high frame rates (up to 38 kHz) to capture motion dynamics in blood vessels from the back-scattered wave reflections as ultra-Doppler information (Fig. 1.2 a). Each plane wave transmission produces an out-of-focus ultra-sonic image with a signal reflected from each image-pixel/point in the imaging field-of-view (FOV) of the tissue. Refocusing of the image is achieved via coherent compounding – a process that combines a set of backscattered signals acquired from plane waves transmitted at "n" different angles ($3 < n < 17$, typical) to form a compound image (Fig. 1.2 b) [1,2]. A compound image typically has higher quality compared to an image produced with conventional ultrasound generated with similar parameters and requires less than 1 ms to produce. Thus, in theory a thousand compound images are possible in a second. To augment sensitivity, the compound images can be sampled at a rate up to 1 kHz and integrated into a single image – with each pixel signal represented as a mean intensity (I) power Doppler (pD) value (Equation 1).

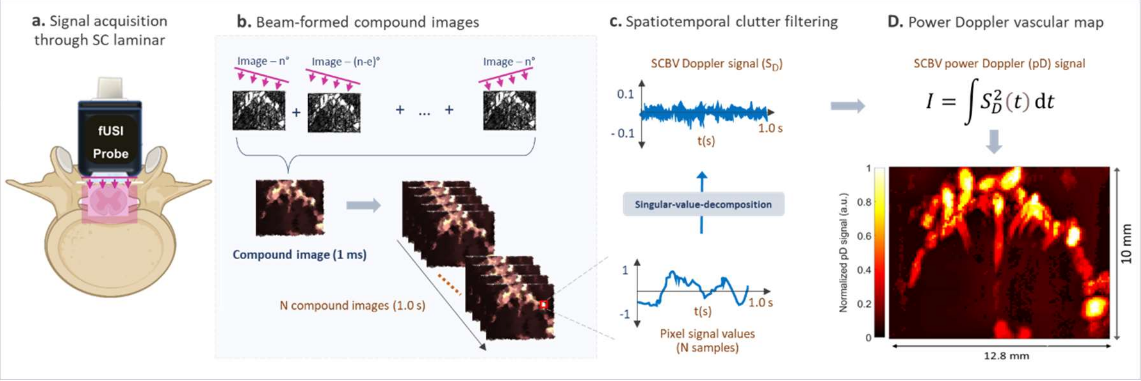

Figure 1.2 Flowchart of functional ultrasound imaging. A) FUSI signal acquisition through a human spinal cord laminar. B) Coherent compounding of backscattered acoustic signals to form time-aligned compound images. C) Clutter filtering of each pixel's signal to separate static tissue signal from blood volume motion signal using singular-value-decomposition or high frequency filters. D) Pixelwise-signal summation of filtered signals across compound images to generate a vascular map based on power Doppler intensity.

Prior to integration of compound images to extract the pD intensity-based image, a high frequency or singular value decomposition (SVD)[24,25] clutter filter is applied to the series of signal values acquired from each pixel from each compound image to remove the stationary tissue signal from blood-motion signal (Fig.1.2 c). The mean pD intensity is proportional to the vascular blood volume.

$$I(x,y) = \frac{1}{N}\sum_{i=1}^{N} |s_F(x,y,t_i)|^2 \tag{1}$$

Where N = total number of samples, S_F = filtered signal value at each image pixel, y = depth axis, x = axis along the fUSI transducer, and t = time. The resulting pD signal intensity can be tracked across time to capture functional activations on the order of 1 s scale in functional imaging studies. For a more comprehensive overview of the theory and principles of fUSI, see [1,2,20]. Note that the axial blood velocity at each pixel can also be extracted from the clutter filtered signal from the central frequency of the resulting frequency density spectrum and can be visualized as a color Doppler (cD) image. While color Doppler images have utility in certain applications, all the fUSI signal analyzed in this thesis were acquired as mean pD intensity-based images.

1.1.3 Applications of fUSI

The capability of fUSI to record evoked cerebral blood volume (CBV) changes associated to functional alterations *in vivo*, was first demonstrated in 2011 in the rat whole-brain during whisker stimulation [1]. Subsequently, fUSI has been extended to capture intrinsic connectivity *in vivo* in the rat brain [26] as well as detect brain activity in freely moving rodents [22]. In addition, fUSI has been applied to non-human primates (NHP) to reveal propagations of task related brain activity [27] and to decode movement intentions at a single-trial level from brain activity [28]. In clinical studies, fUSI has successfully been employed intraoperatively during surgery for functional and vascular brain mapping and to record brain activity in both anesthetized and awake adult patients [29,30]. It was also applied to study brain function and dynamic connectivity in human neonates and newborns [31,32]. Recent studies that investigated the effects of epidural spinal cord stimulation revealed that fUSI can capture responses of spinal cord hemodynamics to electrical stimulation in rats [33].

Overall, while these studies demonstrate the potential of fUSI as a useful investigative tool for research and clinical applications, it remains a novel technology with tremendous potential. As such, it's potential can be leveraged to illuminate several unanswered questions and gaps in the fields of neuroscience, bioengineering, and medicine pertaining to our understanding of functional neural responses, the effects, and mechanisms of action of stimuli, neurological conditions, and neuromodulation in the spinal cord and brain.

1.2 Thesis overview

Thus far fUSI has been employed mostly for preclinical animal studies and few basic human-applications. It has yet to be fully applied for clinical guidance and human application. Therefore, the objective of this dissertation is to explore the potential of fUSI as a technology that can assess responses of the human brain and spinal cord in real-time, towards closed-loop application to disease conditions and neuromodulation in a clinical setting.

Herein this dissertation we leverage the enhanced sensitivity and spatiotemporal properties of fUSI to illuminate how and where ensemble neurons in the brain and spinal cord activate and/or deactivate in response to various chemical, disease, and electromagnetic interventions, both in animal and human studies.

In preclinical animal studies, we investigate the effects of ketamine and dizocilpine (MK-801) N-methyl-D-aspartate (NMDA) drugs on cerebral blood volume (CBV) in rat and mice brains respectively. In the MK-801 drug study, we also assess the response of cerebral hemodynamics to deep brain stimulation (DBS) of the medial septal nucleus at different stimulation frequencies – post MK-801 drug injection to induce hypoperfusion in the brain.

In clinical human studies, we investigate neural response to function, disease and stimulation in the brain and spinal cord. Utilizing fUSI, we characterize and decode responses of the human spinal cord hemodynamics to invasive and non-invasive electrical stimulations. Furthermore, we correlate bladder pressure signal to fUSI recording of the spinal cord hemodynamic response to an end-organ physiological function during a controlled-urodynamics bladder filling and emptying process, and subsequently decode the bladder pressure state solely from fUSI spinal cord signal. Finally, we extend our application of fUSI to characterize modulations to brain hemodynamics induced by aberrant seizure condition in patients suffering from chronic severe pharmaco-refractory focal epilepsy, and subsequently assess how a non-invasive electrical stimulation of the common peroneal nerve of the lower limb evokes specific changes to cortical network-activity.

Chapter 2

Pharmacological and Deep Brain Stimulation Effects on Cerebral Hemodynamics in Rodents as Measured by Functional Ultrasound Imaging

Reprinted with permission from Crown L. and Agyeman K, et. al.

2.1 Abstract

Deep brain stimulation (DBS) and transcranial magnetic stimulation (TMS) have shown remarkable success in treating neurological and psychiatric disorders such as Parkinson's disease, essential tremor, dystonia, epilepsy, cognitive motor-dysfunction – post stroke, and obsessive-compulsive disorder. Despite this success, the underlying mechanism of action remains unknown. DBS is now being explored as a means to improve cognition and functional outcomes in other psychiatric conditions, such as those characterized by reduced

N-methyl-D-aspartate (NMDA) function (i.e. schizophrenia). While most DBS treatments for movement disorders require continuous stimulation, there is evidence that intermittent stimulation in cognitive and psychiatric conditions may have persisting effects beyond the period of stimulation. This suggests that the effects of DBS on brain activity last beyond the time of its acute electrical effects, necessitating a broader exploration of how neuromodulation alters brain networks. In this study, we utilize functional ultrasound imaging to characterize the spatial and temporal dose effects of ketamine on cerebral hemodynamics and determine the fUSI signatures of slow-wave activity (SWA) and poly-population spiking (PPS) activity in the rat brain. Furthermore, we assess the cerebrovascular impact of medial septal nucleus (MSN) DBS under conditions of NMDA antagonism (pharmacologically using Dizocilpine [MK-801]) in anesthetized mice. Imaging from a sagittal plane across a variety of brain regions, we find that MSN theta-frequency (7.7Hz) DBS had a larger effect on hippocampal cerebral blood volume (CBV) after stimulation offset. This was observed following an intraperitoneal (i.p.) injection of either saline vehicle or MK-801 (1 mg/kg). This effect was not present using standard high frequency DBS stimulation parameters (i.e. gamma [100Hz]). These results indicate the MSN DBS increases circuit-specific hippocampal neurovascular activity in a frequency-dependent manner and does so in manner that continues beyond the period of electrical stimulation.

2.2 Introduction

There is growing interest in utilizing neuromodulation to treat cognitive impairment associated with neurological, psychiatric disorders and brain injury. Many of these disorders involve aberrant electrophysiology and cerebral blood perfusion [34,35]. Recent evidence demonstrates that electrical neuromodulation can improve functional outcomes [36,37].

Particularly, deep brain stimulation (DBS) has shown remarkable success in treating neurological diseases such as movement disorders and epilepsy, and there is increasing evidence for its efficacy in cognitive and psychiatric conditions. Similarly, transcranial magnetic stimulation (TMS) has been shown to be effective for motor dysfunction and cognitive rehabilitation after stroke [38–43]. It is non-invasive – an additional advantage. Repetitive TMS has also shown success in the control of medically refractory epileptic-seizures [44].

Despite this growing utility, the underlying mechanism of DBS and TMS for motor and cognitive outcomes remain largely unknown. Pre-clinical studies have been hindered by technological limitations, such as the inability to record electrical brain activity during stimulation and the low spatial resolution of electrographic measures. Functional ultrasound imaging is a relatively new neuroimaging modality that enables large-scale estimates of neural activity through measures of cerebral blood volume (CBV). fUSI provides a unique combination of high spatiotemporal resolution and high sensitivity to slow blood flow across a large field of view. In fact, fUSI has already proven to be an effective tool for imaging large-scale brain activity and pharmacodynamics [1,2,28,45]. As such, it is well-positioned to improve our understanding of the impacts of DBS and TMS on large-scale brain networks during and after stimulation.

Ketamine is a fast-acting N-methyl D-aspartate (NMDA) receptor antagonist that has received considerable attention due to its salubrious effects for treating depressive disorders and suicidal ideation at subanesthetic dosage [46–49]. (S)-ketamine is now approved by the food and drug administration (FDA) for treating major depressive disorder. While its non-competitive antagonism at the glutamatergic NMDA receptor is believed to mediate the antidepressant activity, the mechanism of action (MOA) at brain systems-level remains speculative at best. Beyond its therapeutic applications, ketamine is also widely employed as an anesthetic and a model in preclinical studies to investigate the pathophysiology of psychosis [50,51], disruptions to network connectivity in sensory and prefrontal cortex, as well as modulation of cortical oscillations within and across brain regions with respect to memory function [52–56]. However, these effects are predominantly studied under subanesthetic or anesthetic doses – with little consideration for the high dose effects of ketamine. While ketamine is known to induce loss of responsiveness [54], slow-wave activity (SWA) and poly-population spiking (PPS) [52]activity at high dose levels, knowledge on the dose effects on brain hemodynamics and cerebral networks remain limited. Presently, little is known about the MOA and spatiotemporal dynamics of SWA and PPS activity in the brain. A better understanding of PPS propagation in preclinical studies may serve as a proxy to model epileptic-seizure characteristics and propagation dynamics in humans.

Furthermore, in many disorders, cognitive dysfunction is accompanied by altered septohippocampal network activity. For instance, neural oscillatory patterns within the septohippocampal network, such as gamma- and theta-band activity, are characteristically altered in disorders such as schizophrenia and Alzheimer's disease and are often correlated with impaired memory [34,57–59]. Alterations in specific neurotransmitter signal transduction pathways also play an important role in modulating neural oscillatory activity. In particular, the glutamatergic NMDA receptor is crucial to regulating hippocampal theta and gamma oscillations and is the predominant molecular control for synaptic plasticity and memory function [60–62]. Consequently, pharmacologic NMDA receptor antagonism through drugs such as dizocilpine (MK-801) results in characteristic changes to neural oscillatory patterns and memory dysfunction [50,63–66].

The medial septal nucleus (MSN) is a key structure in the septohippocampal network that modulates sensory-motor processing and acts as a "pacemaker" for hippocampal theta oscillations via dense glutamatergic, cholinergic, and GABAergic projections to the hippocampus [67,68]. This makes the MSN a promising target for DBS in cognitive disorders involving memory impairments [69]. Our recent work as well as that of others suggest that modulating the septohippocampal network via MSN DBS can restore cognitive impairment and memory dysfunction in preclinical models of epilepsy, traumatic brain injury, Alzheimer's disease, and schizophrenia [69–74].

Herein we leverage fUSI to investigate the effects of MK-801 on CBV in the septohippocampal network (Fig. 2.1 A) including the hippocampus, and medial prefrontal cortex (mPFC). Within the same sagittal plane, we also image CBV changes (ΔCBV) to regions of interest (ROIs) outside this network including the striatum, thalamus, hypothalamus, and pallidum. Note that other regions that are connected to the MSN, such as amygdala, habenula, or raphe nucleus were not recorded, since they were not accessible from the selected 2D image plane. We also determined the effect of direct MSN stimulation on blood flow in these areas using two distinct frequencies, theta (7.7Hz) and gamma (100Hz). Finally, we test the hypothesis that MSN theta-frequency-specific stimulation can improve blood flow under conditions of reduced NMDA function.

Additionally, we extend the current study to characterize the spatial and temporal effects of high dose ketamine on brain hemodynamics utilizing fUSI pD signal acquired from cortical motor-sensory, mid-brain and brain stem regions of the rat, within the same sagittal plane (Fig. 2.7 B). While SWA and PPS activity evoked by ketamine have been demonstrated from multi-array electrode (MEA) electrophysiological single-unit and local field potential (LFP) recordings by our team [52], here we characterize fUSI signal correlates of ketamine evoked SWA and PPS activity responses and onset dynamics.

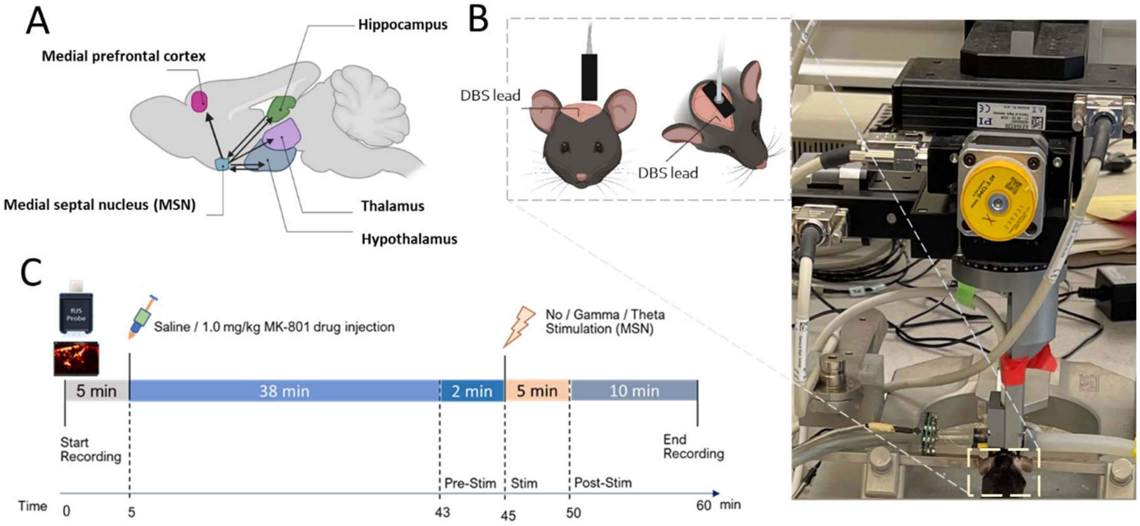

Figure 2.1 Experimental setup and fUSI recording protocol. A) Schematic illustration of connectivity between the MSN and ROIs. Arrowheads represent axonal projections to and/or from MSN. B) Experimental set-up showing the anesthetized mouse in a stereotaxic frame under the Iconeous One motorized probe mount. DBS stimulating electrodes were implanted on the left hemisphere and a sagittal plane of the right hemisphere was imaged. C) Diagram of the protocol for 60 minutes of continuous fUSI acquisition consisting of saline or 1.0 mg/kg MK-801 drug injection (at the 5-minute mark) and 5 minutes of gamma- or theta-frequency DBS (at the 45-minute mark).

2.3 Results

2.3.1 NMDA antagonist MK-801 reduced blood perfusion

We analyzed 40 minutes of pD signal from the septohippocampal circuit (hippocampus, mPFC) as well as surrounding structures (hypothalamus, thalamus, pallidum, and striatum) to assess the effects of MK-801 on cerebral hemodynamics (Fig. 2.2 A). We quantified changes in CBV (ΔCBV) as a percent change relative to baseline activity (average of 2 minutes pD signal acquired prior to drug injection). A repeated measures ANOVA (factors treatment × ROI; where treatment is saline vs. MK-801 and ROI is the 6 recorded brain areas) revealed that there was a statistically significant effect over time (F (2519, 56406) = 8.76, p = 6.3 x 10^{-5}) after Greenhouse-Geiser approximation correction. To quantify the effect of MK-801 on CBV, we computed the percentage change (i.e., ΔCBV) relative to baseline using the last two minutes before stimulation onset (38-40 minutes after drug injection) and found a reduction of ΔCBV (mean ± SEM) in the hippocampus (-3.6 ± 1.1 %), mPFC (-4.1 ± 0.61 %), hypothalamus (-1.0 ± 0.2 %), pallidum (-1.5 ± 0.4 %), striatum (-1.7 ± 0.3 %), and thalamus (-3.0 ± 0.5 %). For saline-treated animals these values were: hippocampus (-0.7 ± 0.6 %), mPFC (-0.1 ± 0.2 %), hypothalamus (-0.7 ± 0.6 %), pallidum (0.9 ± 0.4 %), striatum (-0.3 ± 0.4 %), and thalamus (0.2 ± 0.4 %) (Fig. 2.2 A-F, radar chart, insert). The mean effect-size difference in ΔCBVs and Cohen's d analysis comparing mean ΔCBV induced by saline and MK-801 over a 2-minute interval (38 – 40 minutes post-drug injection), revealed that MK-801 induces greater decreases in CBV than saline control in all ROIs investigated (Fig. 2.2 A-F, radar chart insert) - i.e., mPFC (ΔCBV mean difference between saline and MK-801 animals ± confidence, Cohen's d; 3.96 ± 0.38 %, d= 0.42), thalamus (3.17 ± 0.23 %, d= 0.55), hippocampus (2.82 ± 0.42 %, d= 0.27), pallidum (2.42 ± 0.20 %, d= 0.49), hypothalamus (1.72 ± 0.12 %, d= 0.59) and striatum (1.33 ± 0.18 %, d= 0.29). Together, these results indicate that MK-801 reduces CBV both within and outside of the septohippocampal network.

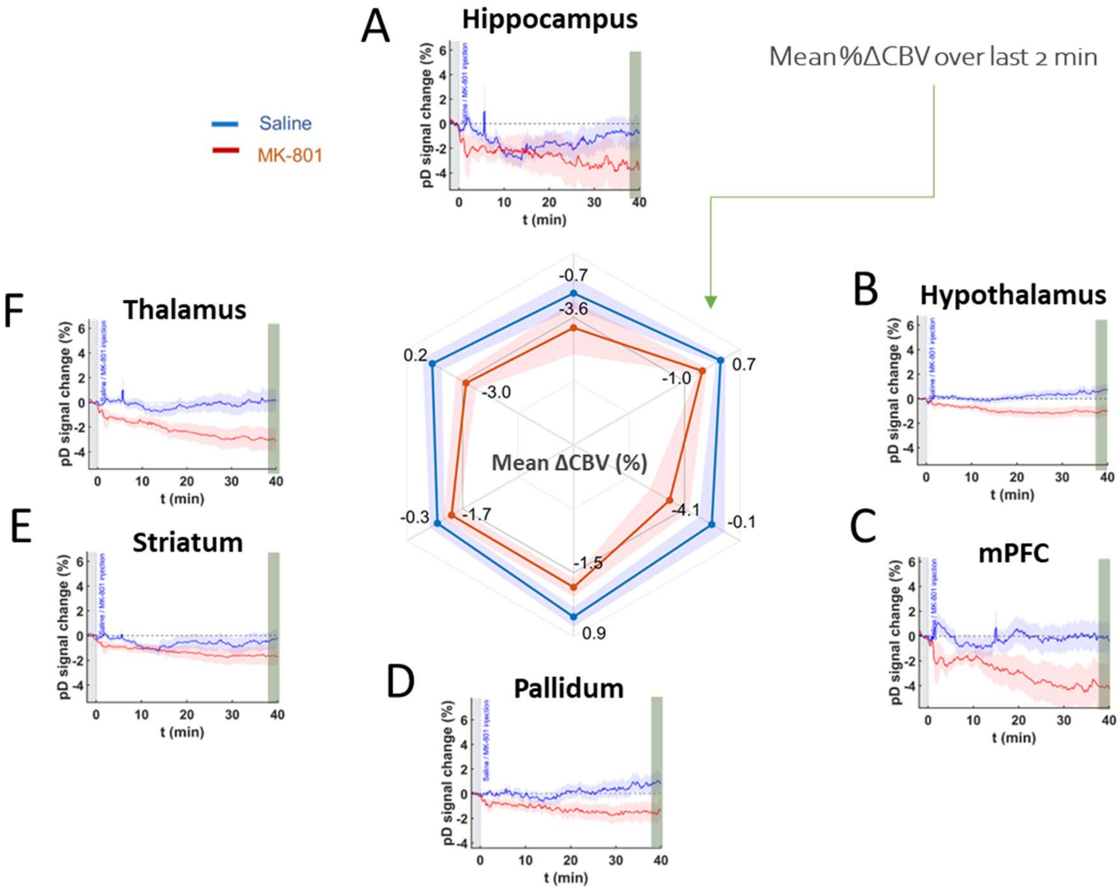

Figure 2.2 Event related average (ERA) temporal course curves prior to stimulation onset and mean ΔCBVs during the last 2 minutes in saline and MK-801 treated animals. A – F) Temporal course (42 minutes) of ΔCBV relative to baseline (2-minute average pD signal before saline or MK-801 drug injection) in the A) hippocampus, B) hypothalamus, C) mPFC, D) pallidum, E) striatum, and F) thalamus after saline [blue] and 1.0 mg/kg MK-801 [1] injection. The radar chart insert, shows MK-801-induced decreases in CBV in all ROIs compared to saline over the last 2 minutes interval from 38-40 minutes post injection.

2.3.2 MSN stimulation increases CBV in saline control animals in a frequency- and region- dependent manner

We assessed whether theta- and gamma-frequency MSN stimulation has disparate impacts on CBV measures in saline-treated control mice. ERAs of ΔCBV reflect the temporal responses to theta, gamma, and no stimulation during and post stimulation time periods (Figs. 2.3, 2.4). A three-way repeated measures ANOVA (factors, treatment × ROI × DBS; where treatment is saline vs. MK-801, ROI is the 6 recorded brain areas, and DBS is theta frequency vs. gamma frequency vs no DBS) was utilized to examine the effects and interactions of drug, stimulation, and ROIs during the 5 minutes period after onset of MSN stimulation. The two-minute baseline period pre-stimulation was included in the analysis. We found significant effects of drug over time (F (419, 186036) = 7.35, p = 1.85 x 10^{-8}), stimulation over time (F (823, 186036) = 2.71, p = 7.20 x 10^{-4}), as well as interaction of drug and stimulation over time (F (838, 186036) = 1.96, p = 1.95 x 10^{-2}) during the 5 minutes stimulation interval, after Greenhouse-Geisser approximation correction. To further quantify the effects of DBS, we computed the mean ΔCBV in the last 2 minutes during stimulation across animals in each stimulation category and compared the mean-effect size differences in ΔCBVs between no stimulation and stimulation in each ROI. We found that MSN theta stimulation increased CBV compared to no-stimulation only in the mPFC (mean ΔCBV difference between theta- and no-stimulation ± confidence, Cohen's d; 0.82 ± 0.12 %, d= 0.45) and hippocampus (0.39 ± 0.12 %, d= 0.21). The effect size magnitude was either very small (i.e., Cohen's d <0.08) or theta-frequency stimulation caused further reduction in CBVs compared to no-stimulation, in the other ROIs. On the other hand, MSN gamma stimulation caused increases in CBV compared to no-stimulation in the mPFC (0.60 ± 0.11 %, d= 0.36), pallidum (0.38 ± 0.09 %, d= 0.30) and striatum (0.22 ± 0.06 %, d= 0.26). For the rest of the ROIs the effect size magnitude was either very small (i.e., Cohen's d < 0.095) or gamma-frequency stimulation resulted in further reduction in CBVs compared to no-stimulation. When comparing the ΔCBV induced by the theta and gamma stimulation in mPFC – the only ROI that exhibited moderate effect on both types of stimulations – we found very small effect size on ΔCBV between the two types of stimulations (mean ΔCBV differences between theta- and gamma-stimulation ± confidence, Cohen's d; 0.22 ± 0.10, d= 0.14).

The next step was to assess the effects of DBS after stimulation offset (i.e., post-stimulation). To do so, we conducted a three-way repeated measures ANOVA (factors, treatment × ROI × DBS; where treatment is saline vs. MK-801, ROI is the 6 recorded brain areas, and DBS is theta frequency vs. gamma frequency vs no DBS) over the 10 minutes period after the offset of MSN stimulation. We found significant effects of drug over time (F(1019, 452436) = 5.28, p = 1.27 x 10^{-4}), stimulation over time (F(2038, 452436) = 3.67, p = 1.17 x 10^{-4}), as well as, interaction of drug and stimulation over time (F(2038, 186036) = 3.09, p = 9.40 x 10^{-4}), after Greenhouse-Geisser approximation correction, across the 10 minutes post-stimulation interval. We further quantified the post-effects of DBS by computing the mean ΔCBV in the last 2 minutes of the acquisition – i.e., 8-10 minutes post-stimulation and comparing the mean-effect size differences on ΔCBV between no stimulation and stimulation in each ROI. The results showed that MSN theta stimulation causes increases in CBV compared to no-stimulation in the hippocampus (mean ΔCBV differences between theta- and no-stimulation ± confidence, Cohen's d; 1.30 ± 0.21, d= 0.42), mPFC (1.20 ± 0.22 %, d= 0.37) and thalamus (0.97 ± 0.11 %, d= 0.58) (Fig. 2.4 A, F – radar chart). On the other hand, MSN gamma stimulation resulted in an increase in CBV compared to no stimulation in the mPFC (2.01 ± 0.22 %, d= 0.60), striatum (0.77 ± 0.14 %, d= 0.37) and pallidum (0.61 ± 0.16 %, d= 0.25). When comparing the differences in ΔCBVs induced by theta and gamma stimulation in the mPFC – the only ROI that exhibited medium to moderate effect on both types of stimulations – we found that gamma induces higher ΔCBV than theta stimulation with medium effect size difference (mean ΔCBV differences between gamma- and theta-stimulation ± confidence, Cohen's d; 0.81 ± 0.17, d= 0.31).

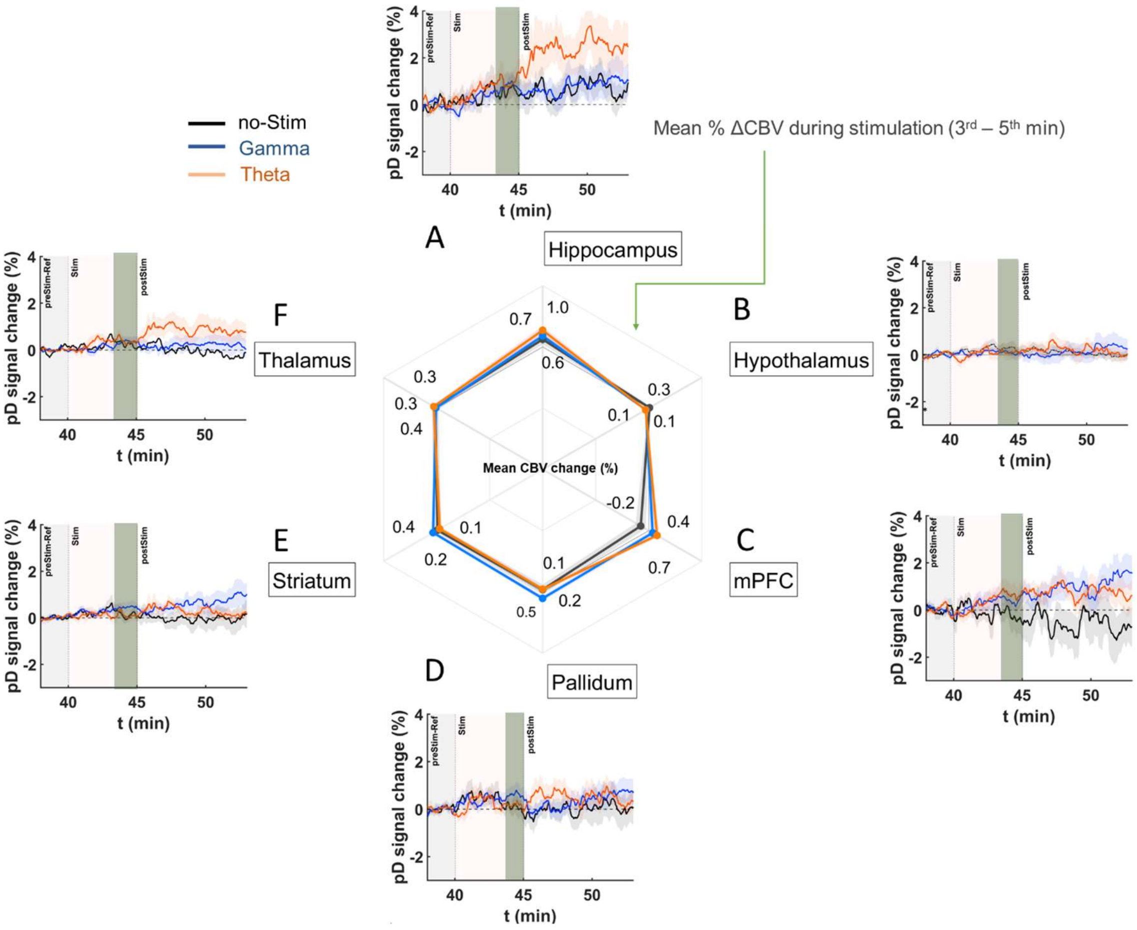

Figure 2.3 DBS ERA curves after stimulation onset and mean ΔCBVs in saline mice during the last 2 minutes of stimulation period. A – F) Temporal course (theta [orange], gamma [blue], no-stimulation [black]) of mean ΔCBV relative to baseline (2 minutes average pD signal prior to DBS) for the A) hippocampus, B) hypothalamus, C) mPFC, D) pallidum, E) striatum, and F) thalamus regions in the saline-treated animals. Radar chart insert gives the mean percentage ΔCBVs during stimulation for theta [orange], gamma [blue], and no-stimulation [dark gray] animals in the ROIs investigated. Means were calculated utilizing the last 2 minutes of pD signals acquired during stimulation (3rd – 5th minute after stimulation onset) across animals in each stimulation category.

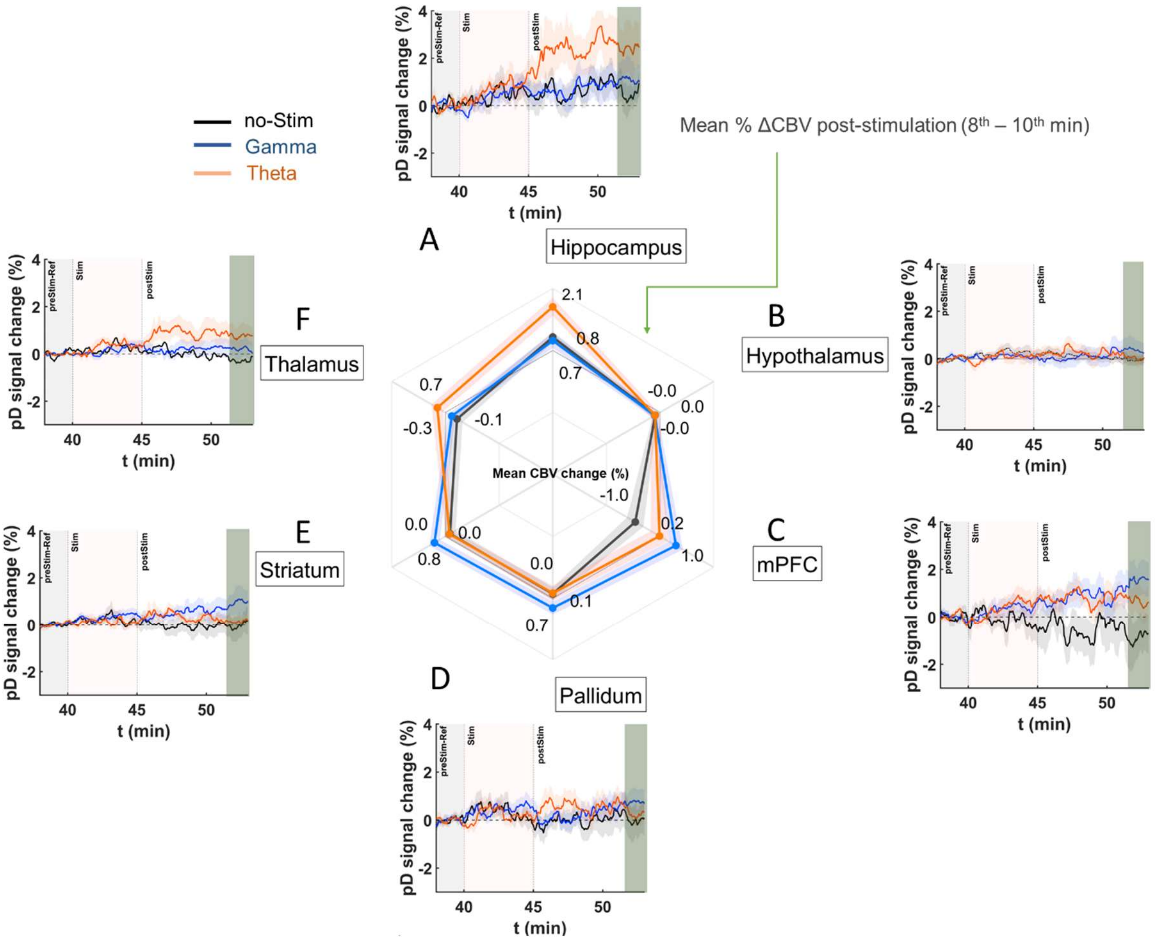

Figure 2.4 DBS ERA curves after stimulation onset and mean ΔCBVs in saline mice during the last 2 minutes of recordings in the post-stimulation period in 6 ROIs. Akin to Figure 2.3, but the radar chart gives the mean percentage ΔCBVs during post-stimulation for theta [orange], gamma [blue], and no-stimulation [dark gray] for the A) hippocampus, B) hypothalamus, C) mPFC, D) pallidum, E) striatum, and F) thalamus regions in the saline-treated animals. Means were calculated utilizing the last 2 minutes of pD signals acquired post stimulation (8th – 10th minute after stimulation offset) across animals in each stimulation category.

2.3.3 Theta-frequency stimulation elicits stronger CBV increases than gamma-frequency stimulation in MK-801 treated animals.

Recently, our group showed that theta, but not gamma frequency DBS of the MSN improves spatial memory in MK-801 treated rats [74]. Therefore, we sought to determine if MSN theta and gamma frequency stimulation had differing impacts on neurovascular activity measures within memory-associated regions including the mPFC and hippocampus as well as neighboring regions outside the septohippocampal network (striatum, pallidum, thalamus, hypothalamus) following MK-801 drug-administration. Again, we assessed the mean effect-size differences in ΔCBV between MSN theta-, gamma-, and no-stimulation in each of the selected ROIs, relative to 2 minutes of pD signal recordings just prior to stimulation onset. The analysis was performed after repeated measures ANOVA over the stimulation and post-stimulation time intervals to examine the effects and interactions of drug, stimulation, and ROI (results presented in previous section). Figures 2.5 and 2.6 display the ERA curves for ROIs in response to theta, gamma, and no DBS during and post stimulation periods in the MK-801 group. We found that MSN theta stimulation in the MK-801 treated group caused increased ΔCBV with respect to no-stimulation group with medium to large effect size in all ROIs except mPFC – i.e., hippocampus (mean ΔCBV differences between theta- and no-stimulation ± confidence, Cohen's d; 2.01 ± 0.20 %, d= 0.78), thalamus (0.49 ± 0.07 %, d= 0.54), pallidum (0.36 ± 0.07 %, d= 0.43), striatum (0.18 ± 0.04 %, d= 0.31) and hypothalamus (0.14 ± 0.04 %, d= 0.30) (Fig. 2.5). Intriguingly, we only found a medium effect-size increase in ΔCBV for the pallidum (0.60 ± 0.08 %, d= 0.53) and striatum (0.23 ± 0.05 %, d= 0.38) between MSN gamma- stimulation and no-stimulation groups, during the stimulation period. For the rest of the ROIs, the effect-size was very small.

Importantly, we found that ΔCBV increased in theta- relative to no-stimulation animals after stimulation offset with medium to larger effects in the pallidum (1.26 ± 0.15 %, d=0.66), hippocampus (2.8 ± 0.37 %, d=0.60) and thalamus (1.24 ± 0.17 %, d= 0.57) and small to medium effects in the striatum (0.50 ± 0.13 %, d= 0.31), hypothalamus (0.21 ± 0.06 %, d= 0.28) and mPFC (0.64 ± 0.22 %, d= 0.22) (Fig. 2.6). Importantly, we found only small to medium effects of gamma MSN stimulation on ΔCBV in the pallidum, relative to stimulation animals, and after stimulation offset (mean ΔCBV differences between gamna- and no-stimulation ± confidence, Cohen's d; 0.66 ± 0.13 %, d=0.39) (Fig. 2.6). For the rest of the ROIs, the effect-size was either very small (i.e., Cohen's d < 0.1 in hippocampus, striatum, and thalamus) or gamma-frequency stimulation resulted in further CBV reduction (i.e., in hypothalamus and mPFC) compared to no-stimulation.

Additionally, our results showed medium or large mean effect-size differences in ΔCBVs between the theta and gamma stimulated MK801 groups after stimulation offset in the hippocampus (2.67 ± 0.28 %, d= 0.70), mPFC (1.83 ± 0.23 %, d= 0.59), and thalamus (1.15 ± 0.14 %, d= 0.56) (Fig. 2.6). Together these results demonstrate that theta-frequency stimulation elicits the strongest CBV response in MK-801-treated mice in the hippocampus and pallidum, while gamma stimulation had almost no effect on hippocampal CBV (Cohen's d = 0.03) and decreased CBV in the mPFC compared to no-stimulation mice.

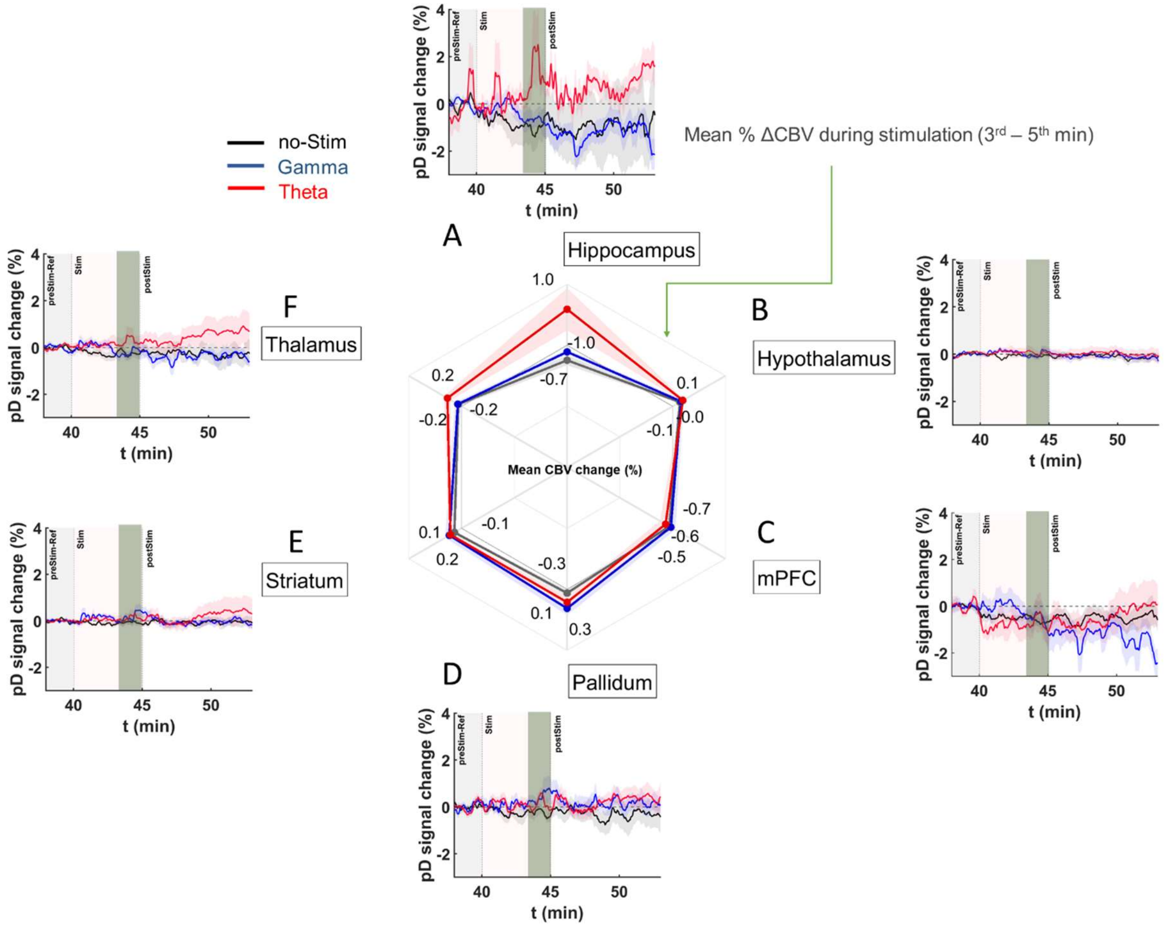

Figure 2.5 DBS ERA curves after stimulation onset and mean ΔCBVs in MK-801 treated mice during the last 2 minutes of stimulation period A – F) Temporal course (theta [1], gamma [blue], no-stimulation [black]) of mean ΔCBV relative to baseline (2 minutes average pD signal prior to DBS) for A) hippocampus, B) hypothalamus, C) mPFC, D) pallidum, E) striatum, and F) thalamus regions in the MK-801 drug injected mice. Radar chart insert gives the mean percentage ΔCBVs during stimulation for theta [1], gamma [blue], and no-stimulation [dark gray] animals in the ROIs investigated. Means were calculated utilizing the last 2 minutes of pD signals acquired during stimulation (3rd – 5th minute after stimulation onset) across animals in each stimulation category.

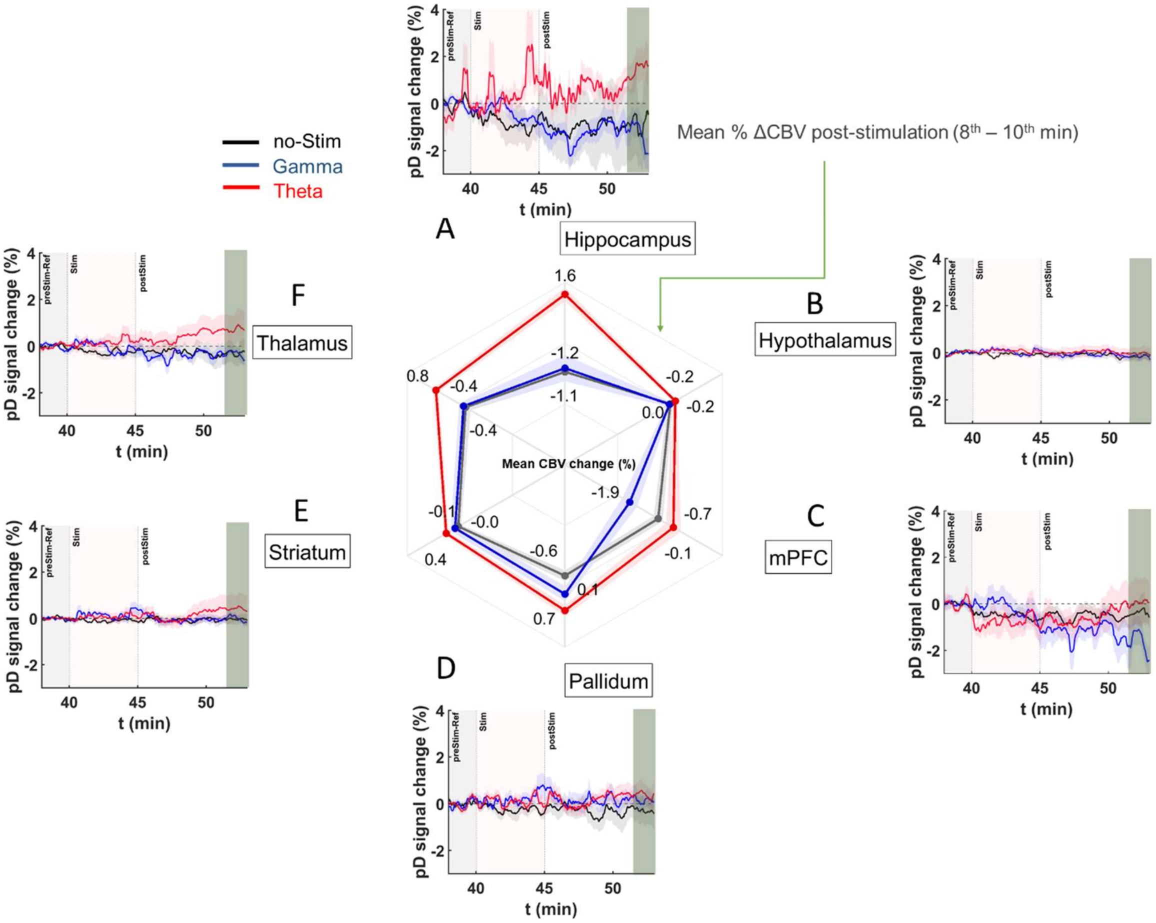

Figure 2.6 DBS ERA curves after stimulation onset and mean ΔCBVs in MK-801 treated mice during the last 2 minutes of recordings in the post-stimulation period. Akin to Figure 2.5, but the radar chart gives the mean percentage ΔCBVs in post-stimulation period for theta [1], gamma [blue], and no-stimulation [dark gray] for the A) hippocampus, B) hypothalamus, C) mPFC, D) pallidum, E) striatum, and F) thalamus regions in the MK-801 treated animals. Means were calculated utilizing the last 2 minutes of pD signals acquired post stimulation (8th – 10th minute after stimulation offset) across animals in each stimulation category.

2.3.4 Spatiotemporal effects of ketamine on brain hemodynamics

To assess the effects of high dose ketamine on brain hemodynamics we acquired 2D sagittal fUSI signal of the rat whole brain through a cranial window in one hemisphere (Fig. 2.8 A), combined with simultaneous electrophysiological multi-array electrode (MEA) single-unit and LFP recordings of electrical activity signal in sensory-motor (S1, M1) regions in the opposite brain hemisphere (Fig. 2.7 A-B). A silicone (64-channel, Neuronexus A8 x 8, Ann Arbor MI, USA) was implanted in M1 (layer 5) and S1 (layer 4-5) to acquire brain LFP activity signal. The rats underwent craniotomy surgery to expose the S1 and M1 brain regions after removal of the dura. Three (n=3, female, 220 – 250 g) Sprague-Dawley rats received three doses of ketamine – the first dose (40 mg/kg) to anesthetize the rats and two additional non-anesthetic high-dose concentrations (45 mg/kg) at the 3- and 13-min marks. Ketamine was injected intraperitoneally to induce slow-wave activity (SWA) and poly-population spiking (PPS) activity respectively (Fig. 2.7 C).

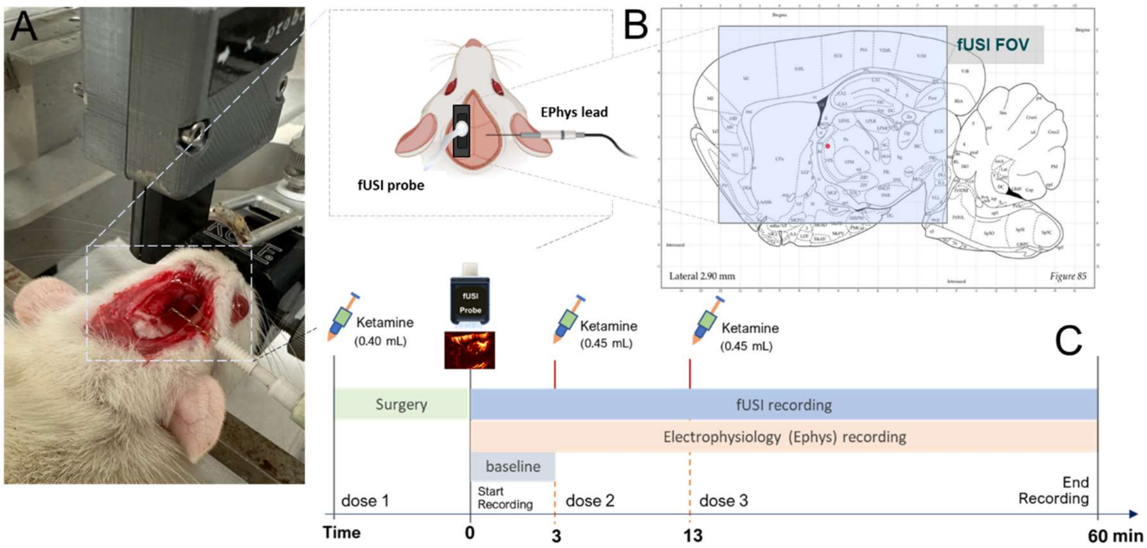

Figure 2.7 Experimental setup and fUSI recording protocol. A) Experimental set-up showing the low-dose ketamine anesthetized rat in a stereotaxic frame under a motorized probe mount. Single-unit and LFP electrophysiological recording electrodes were implanted in the left hemisphere and fUSI signals were acquired in a sagittal plane of the right hemisphere. C) Diagram of the protocol for 60 minutes of continuous and simultaneous electrophysiological LFP and single-unit activity and fUSI acquisition, accompanied by 2 doses of (45 mg/kg) ketamine drug injection (at the 3- and 13-minute mark).

To characterize how slow-wave activity evoked by high-dose ketamine affects brain hemodynamics, we compute statistical parametric maps (SPM) based on two-sided Student's t-test with false discovery rate correction (FDR). The SPMs were generated by comparing fUSI brain signal acquired after injection of the first, but before the second non-anesthetic dose of ketamine (10 min fUSI signal) to the last 60 s of baseline signal activity. The SPMs identify regions recorded within the brain that are strongly affected by SWA. The results showed that SWA causes strong spatial and local hemodynamic changes in the rat brain (Fig. 2.8 B). We detect changes to CBV within the sensory-motor cortical and mid-brain regions of the rat. To assess the temporal dynamics of the activated brain regions, we also generate event related average waveforms. The waveforms represent the brain cerebral blood volume changes, that is derived as a percent change relative to the 60 s mean baseline activity and averaged across all rats (n=3). They illuminate the temporal patterns of the hemodynamic changes of the rat brain post injection of the first non-anesthetic dose of ketamine. The ERA time course curves represent the combined (pseudo-global, i.e., the mean activity across activated pixels) response of the activated rat brain regions. They show that ketamine-evoked SWA causes strong changes in blood flow in all rats, with notable rising (red) and falling (blue) curves after ketamine injection – peaking around the 20 min mark and plateauing after 30 min mark (Fig. 2.8 C).

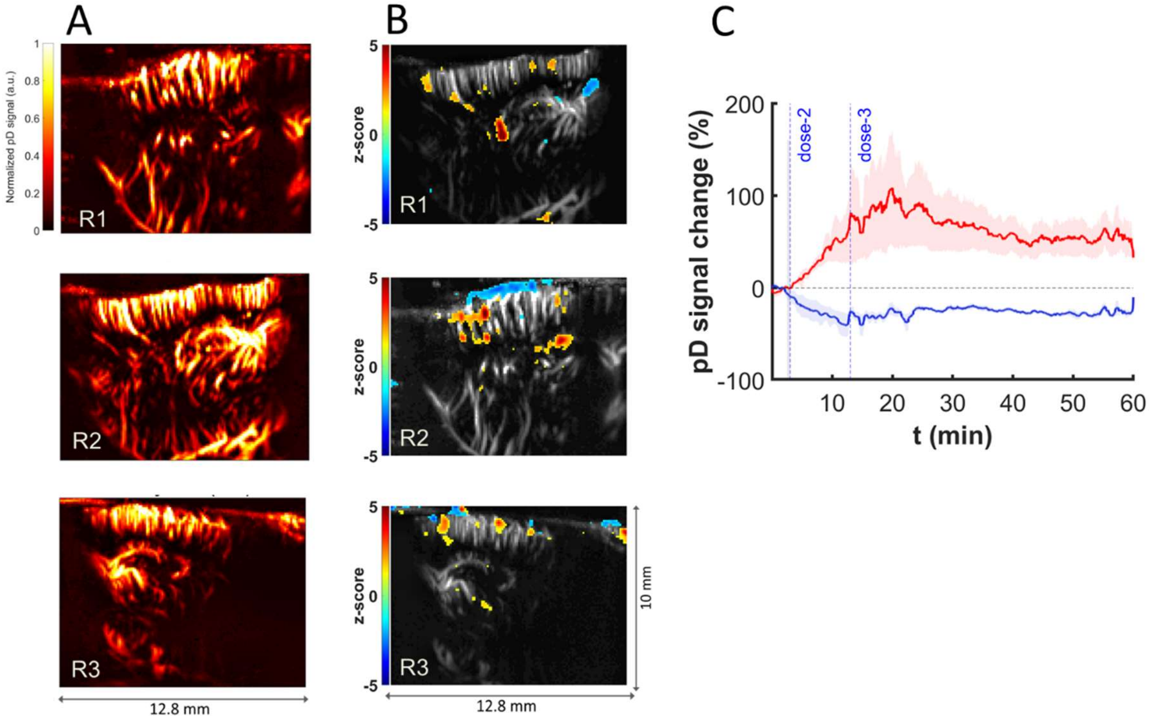

Figure 2.8 fUSI of the rat brain, statistical parametric map, and event-related average waveform. A) fUSI pD intensity-based vascular map of the rat brain in a sagittal plane. B) Statistical map shows localized areas with significantly higher or lower SCBV with respect to reference activity after the first and before the second non-anesthetic ketamine drug injection (10 min signal, two-sided t test of area under the curve, $p < 0.05$, false discovery rate [FDR] corrected for number of pixels in image). SPMs are overlaid on grayscale baseline mean pD intensity images. C) ERA waveforms of the pseudo-global activated pixels (panel B) averaged across all rats. They exhibit strong increased changes of blood perfusion (reddish) or that exhibit strong decrease change of blood perfusion (blueish) in SPMs, after ketamine injection. The pseudo-global ERA waveform is determined as the mean %pD signal change across the SPM activated pixels above a threshold (z-score ≥ 0.7) with respect to 1 min of baseline activity.

2.3.5 Effects of PPS activity on brain hemodynamics and fUSI signature

Next, we characterize and discriminate ketamine evoked poly-population spiking activity effects on brain hemodynamics from the SWA effects. To do so we first determine the characteristic fUSI signature of PPS based on the electrophysiological guided PPS onset and duration timing. fUSI signal acquired during the SWA and PPS activity periods were extracted and integrated into two separate mean 3D image x time matrices, based on the timing of the electrophysiological LFP recordings. We determined the average SWA and PPS activity durations (T_{SWA} = 11.48 ± 0.60 s, mean ± SE) and (T_{PPS} = 4.50 ± 0.08 s, mean ± SE) respectively across all rats. To discriminate ketamine evoked PPS activity effects from SWA effects on brain hemodynamics, we compute statistical parametric maps based on two-sided Student's t-test with FDR correction. The SPMs were generated by comparing brain fUSI signal acquired during PPS activity to the signal acquired during SWA and demonstrate that PPS causes strong regional changes to brain hemodynamics that are consistent across all rats (Fig. 2.9 A, E, I). We detect changes to CBV within the sensory-motor cortical and mid-brain regions of the rat.

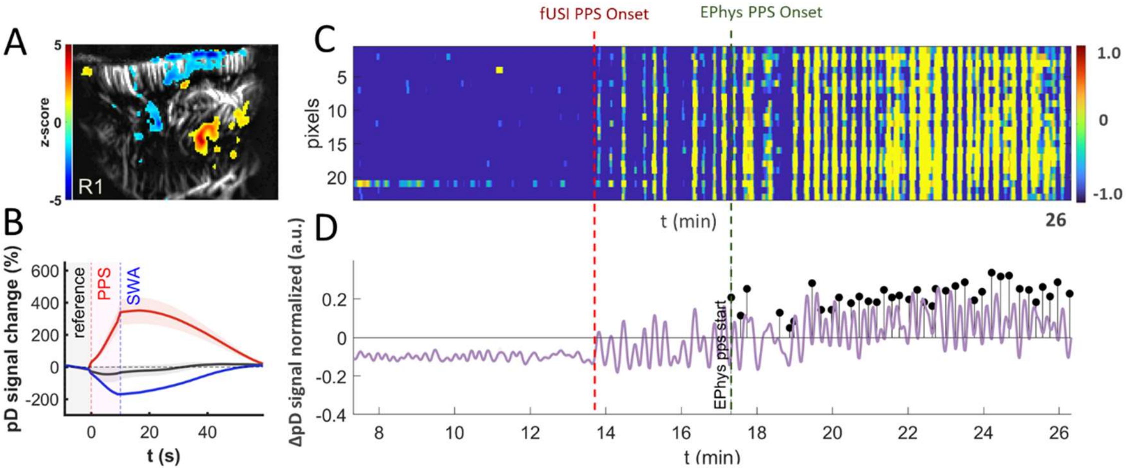

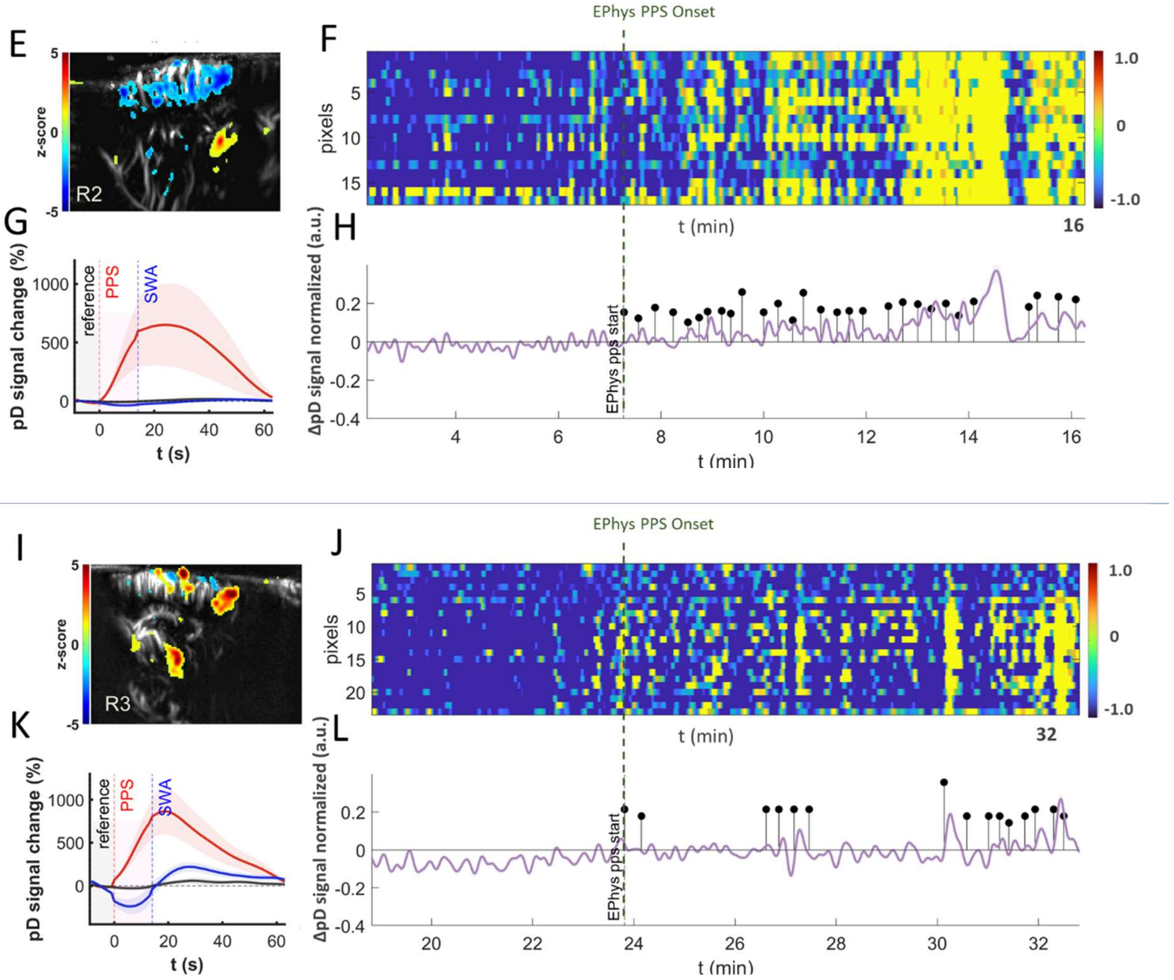

Figure 2.9 Statistical parametric maps, fUSI spectrograph, and event-related average waveform. A, E, I) Statistical map shows localized areas with significantly higher or lower SCBV during poly-population spiking (PPS) activity with respect to reference slow wave activity after injection of high dose of ketamine (two-sided t test of area under the curve, $p < 0.05$, false discovery rate [FDR] corrected for number of pixels in image). SPMs are overlaid on grayscale baseline mean pD intensity images. B, G, K) ERA waveforms of the pseudo-global activated pixels (panels A, E, I) that exhibit strong increased changes of blood perfusion (reddish) or that exhibit strong decrease change of blood perfusion (blueish) in SPMs, comparing slow wave activity to poly-population spiking activity. The pseudo-global ERA waveform is determined as the mean %pD signal change across the SPM activated pixels above a threshold (z-score ≥ 0.7) during PPS with respect to SWA signal. C, F, J) fUSI spectrograph of PPS onset after injection of high dose ketamine. D, H, L) Cerebral temporal mean %pD signal change from before and after the onset of PPS corresponding to selected region-of-interest within the regions of activation regions with significant %pD signal change (A, E, I). Electrophysiological markers of the onsets of PPS are indicated as stem plots.

The ERA time course curves (Fig. 2.9 B, G, K) reveal a strong increase (red curves) and decrease (blue curves) in CBV during PPS activity and a return to the reference activity level at the end of the SWA period in the SPM activated brain regions. The ERAs represent the combined mean %pD signal change over the SPM activated regions across time with respect to the reference activity (last 10 s activity during the SWA periods). The onset of PPS activity (yellow bands) is captured in the normalized mean %pD signal change curve and the corresponding pixelwise activity pD intensity spectrograph across time (Figs. 2.9 C, F, J and D, H, L). Note that the onset times correspond to the start of PPS activity in the fUSI recording brain hemisphere, opposite to the brain hemisphere with implanted electrophysiological electrodes. The time onsets of PPS activity determined from the electrophysiological LFP recordings in the motor and sensory regions are presented as stem plots (black) and indicate the start-time of each PPS activity for each rat after injection of the second non-anesthetic dose of ketamine (Figs. 2.9 D, H, L). Interestingly, the results show that fUSI captured earlier onsets of PPS activity in other brain regions compared to the onset times determined from LFP signal acquired with electrophysiological MAEs in the opposite brain hemisphere (Fig. 2.9 C-D). Together the results demonstrate the capability of fUSI to characterize and differentiate between SWA and PPS activity effects on brain hemodynamics. Furthermore, due to larger spatial coverage, fUSI could detect PPS onset earlier and characterize the PPS propagation dynamics across different brain regions. This finding could have important clinical implications for early epileptic-seizure onset detection.

2.4 Discussion

2.4.1 MK-801 reduced cerebral blood volume in all ROIs

MK-801 and other NMDA antagonists have been widely used in preclinical models to mimic the behavioral and electrophysiological deficits associated with schizophrenia [50,65,75,76]. However, the regionally specific effects of MK-801 on CBV in such models is not well known. We observed that MK-801 reduced CBV across all ROIs. Importantly, previous fMRI studies have observed reduced BOLD signals in hippocampal and prefrontal areas in schizophrenia patients [77–79]. In this context, our findings support the use of MK-801 as a neurovascular model of schizophrenia. Furthermore, our study demonstrates the feasibility of using fUSI to identify network-specific hemodynamic changes as an additional modality for studying neurocognitive disorders.

2.4.2 MSN theta stimulation was relatively specific to cognitive networks.

We observed that theta frequency MSN DBS resulted in an increase to CBV in the hippocampus in both the saline- and MK-801-treated animals. Importantly, this effect was greatest in the hippocampus, which receives direct projections from the MSN, and is a primary target for neuro-modulatory interventions to treat memory dysfunction [70–72,74]. In saline control animals, significant increases to CBV were also observed in the mPFC (during and after stimulation) and thalamus (after stimulation), both of which play important roles in memory function and receive direct projections from the MSN (Fig. 2.1 A) [69]. Interestingly, gamma stimulation did not alter hippocampal CBV, but did increase regions of the brain that were anatomically closer to the MSN. Specifically, mPFC CBV was increased in saline- treated animals, while the pallidum and striatum were increased to a lesser degree in MK-801-treated animals. This suggests that MSN gamma stimulation may have a local response to stimulation but is less specific to the neural circuitry being stimulated.

2.4.3 MSN theta stimulation increased hippocampal CBV during and after stimulation despite NMDA antagonism.

A leading hypothesis is that reduced N-methyl-D-aspartate (NMDA) receptor-mediated glutamatergic transmission underlies psychiatric conditions involving cognitive and memory dysfunction [50,65,75,76,80,81]. Reductions to NMDA activity either pharmacologically or through genetic manipulation have been shown to decrease theta activity, increase gamma activity and lead to deficits in spatial navigation and memory [50,64,74,82,83]. Research by our group has found that acute (<5 minutes) theta frequency (7.7 Hz), but not gamma frequency (100 Hz) stimulation of the MSN during the Barnes maze task improves spatial memory in rodents following pharmacological NMDA antagonism [74]. Interestingly, previous studies have also demonstrated that MSN theta stimulation prior to the task can also improve spatial memory [70]. However, the question remains open as to how MSN DBS mediates these improvements.

2.4.4 MSN theta stimulation may drive high frequency or spiking activity via hippocampal interneurons.

Several studies utilizing various modalities in combination with fUSI have found a strong relationship between pD signal and neuronal activity [84–86]. This relationship was also true for high frequency oscillatory activity (~100Hz) but was much weaker for lower frequency oscillations[86] . This suggests that the theta-induced increases to hippocampal CBV may reflect increased hippocampal gamma or spiking activity, rather than increases to theta oscillatory activity itself. However, given that gamma band activity is often correlated with spiking activity, differentiating between changes in oscillatory dynamics and spiking activity is not possible in the present study [87].

GABAergic interneurons in the hippocampus play an important role in synchronizing hippocampal oscillatory activity. Indeed, inhibitory neurons are hypothesized to be a primary source of dysfunction in pathologies involving NMDA dysfunction (for review see [88]) and are inhibited by NMDA-antagonists [89,90]. One possibility is that theta frequency MSN stimulation may, by briefly stimulating afferent populations at theta-frequency, act as a 'reset' and allow synchronous innervation of hippocampal interneurons that regulate the activity of glutamatergic pyramidal cells. Indeed, it has been previously shown that optogenetic stimulation of GABAergic neurons decreases spontaneous neural activity and leads to an increase in local blood flow [91]. This hypothesis is further supported by a recent study by Nunez-Elizadle and colleagues who observed that the relationship between the fUSI signal and firing rates were greatest for putative interneurons [86]. Future studies combining single unit activity and fUSI could test this hypothesis.

2.4.5 MSN gamma stimulation did not affect hippocampal CBV

Our previous work suggests that MSN theta, but not gamma stimulation can improve spatial memory in MK-801-treated rodents [74]. While MSN theta stimulation increased hippocampal CBV during and after stimulation in MK-801-treated animals, this was not true of MSN gamma stimulation. Gamma stimulation resulted in delayed increases to mPFC CBV in saline-treated animals and had no effect on MK-801-treated animals in any of the ROIs. These results suggest that MSN gamma stimulation is not sufficient to engage hippocampal activity and highlights the importance of frequency parameters in DBS paradigms for spatial memory. This is further supported by our previous study demonstrating no improvement to spatial memory in MK-801 treated animals with MSN gamma stimulation [74].

2.4.6 Implications for neuromodulation

We observed that theta-frequency stimulation of the MSN increased blood perfusion in the hippocampus following cessation of the stimulus. These effects were not observed using gamma stimulation and were still present even under conditions of pharmacologic NMDA antagonism. It is worth noting that arguably the most effective form of neuromodulation is still electroconvulsive therapy (ECT), which is performed under anesthesia and results in increases to cerebral blood flow [92,93]. However, ECT is very non-specific, this lack of specificity may well contribute to its detrimental effect on memory [94]. Alternatively, transcranial magnetic stimulation (TMS) is most effective when applied focally to awake, alert patients [95,96]. Because DBS can combine a relatively high degree of modulation in deep structures with the spatial specificity of TMS, it is plausible that DBS may have more benefits beyond that of ECT or TMS in treating disorders of cognitive function.

2.4.7 Limitations and future directions

While the current study was performed in anesthetized animals, futures studies will investigate the effects of reduced NMDA function and MSN DBS in awake, behaving animals during memory-associated behavioral tasks (e.g., novel object recognition and Barnes Maze). The goal will be to determine if the observed ΔCBV within the septo-hippocampal network following theta- frequency MSN DBS is also associated with improved memory function, linking the present study with our previous study demonstrating improved memory following MSN DBS in MK-801 treated animals [74].

Another limitation of our study is that fUSI recordings performed using the conventional 1-dimensional linear ultrasound transducer array necessarily generate 2-dimensional pD vascular maps of the animals' CBV. As a result, other regions connected with the MSN besides the hippocampus and mPFC (e.g., amygdala, habenula, raphe nucleus) were not accessible from the selected sagittal 2-dimensional image plane. Recent studies are tackling this challenge using whole-brain 3-dimensional fUSI with either moving linear arrays (comparable to the array used in our study), matrix arrays or raw column arrays (RCAs) [97–99]. Future studies can use these probes to cover volumes rather than slices of the mouse brain providing access to all areas of the septohippocampal network. Overall and regardless of these limitations, our findings demonstrate the feasibility of using fUSI to characterize network-specific neurovascular changes in disease models as well as understand what parameters in neuro-modulatory techniques most impact cerebral perfusion dynamics.

2.5 Materials and Methods

2.5.1 Animals and surgical procedures

82 male 8–12-week-old C57BL/6 mice (Charles River Laboratories; Hollister, CA) were used in this study. fUSI data from two animals were excluded due to extreme values (Grubbs test for outliers, 98th percentile of all maximum change in pD intensities) that did not appear physiological [100,101]. The animals were divided into two main groups: saline vehicle control (n=46) and MK-801 drug-administered (n=34). Each group was then sub-divided into three categories: no stimulation (saline: n=14; MK-801: n=10), theta stimulation (saline: n=16, MK-801: n=12), and gamma stimulation (saline: n=14, MK-801: n=14).

Mice were anaesthetized with 5% isoflurane in O2/N2O (1:2) carrier gas and then maintained at a constant rate (1.5 - 2%) through surgery and data acquisition. Body temperature was kept constant throughout recordings by placing animals on an electric heating pad. Hair was removed from the mouse's head for fUSI using a commercially available depilatory cream (Nair, Pharmapacks).

To implant DBS electrodes, mice were head-fixed in a stereotaxic frame (David Kopf instruments, Tujunga, CA) and a midline incision of the scalp was made to expose the skull. A 2mm burr hole was then drilled to implant bipolar stimulating electrodes (E363T/2/SPC ELEC .008"/.2MM, Plastics One Inc., Roanoke, VA) targeting the midline MSN (AP: +0.7mm, ML: -0.9mm, from bregma. Z: -4.39mm at 11.8 degrees) from the left hemisphere. Prior to implantation, the electrodes were connected to an electronic interface board (Neuralynx Inc., Bozeman, MT) and bent at 4.5mm from the tip to maximize the proximity of the fUSI probe to the skull. All procedures were approved by the University of Southern California, Institutional Animal Care and Use Committee (IACUC #21006).

2.5.2 Histology

Mice were euthanized immediately after the fUSI recording by isoflurane overdose followed by transcardial perfusion using 50 mL of 0.1M sodium phosphate buffer saline (PBS) and 50 mL of 4% paraformaldehyde. Brains were harvested and stored in phosphate buffered saline at 4°C. To confirm electrode positioning within the MSN, coronal sections were cut at 100μm thickness with a vibratome (Leica VT 1200; Leica Biosystems, Buffalo Grove, IL) and then Nissl stained with Cresyl Violet (Fig. 2.7 A, B).

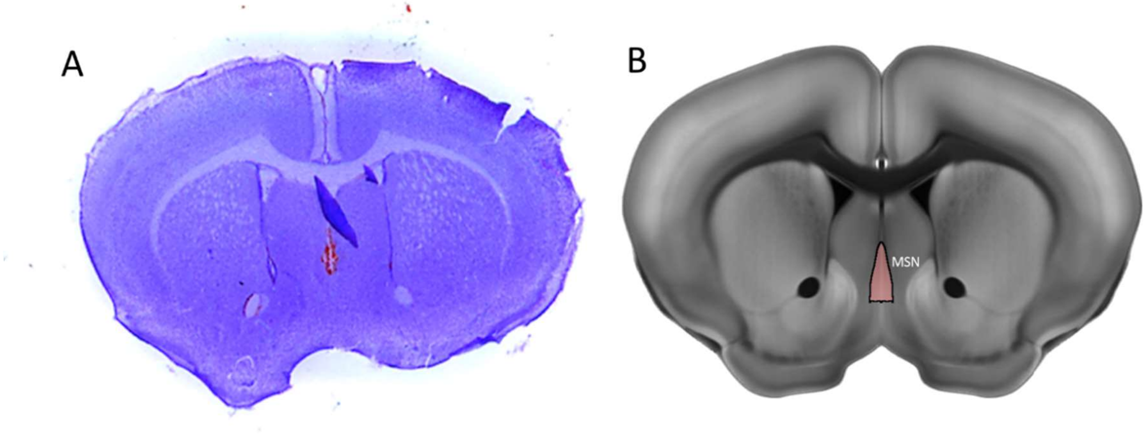

Figure 2.10 Histological mapping of electrode placement in the MSN. A) Representative Nissl stain of the mouse brain with a blood mark indicating the electrode placement B) Annotation of the MSN from the Allen Reference Atlas – Mouse Brain in the same slice position as A.

2.5.3 Computational Modeling of the Induced Voltages: Volume of Tissue Activation

Our group has developed a computational analysis method for applications in electrophysiology and bioelectromagnetic interactions, namely the Admittance Method (AM) [102]. AM discretizes a bulk tissue model into cuboid voxels, where each voxel is represented by an equivalent circuit of lumped passive elements. The admittance value at each voxel is calculated using the material properties such as conductivity and permittivity. A set of linear equations using iterative methods are used to calculate the induced voltage at each node of the voxelized network. Here, a 3-D bulk tissue model with the desired electrode configuration was constructed, a current-controlled stimulation pulse was applied through the electrodes and the induced voltages at each voxel were calculated. A mouse head model (Fig. 2.11 A) was used for this study where three types of tissue were considered (grey matter, white matter (WM) and cerebrospinal fluid (CSF). Electrodes were set as platinum and the medium surrounding the mouse head was set as air. The locations and geometries of the WM and CSF with respect to the septal medial nucleus were approximated using an interactive online mouse brain atlas (http://labs.gaidi.ca/mouse-brain-atlas/). The output from AM was then processed using a MATLAB script to produce an illustration of the voltage mapping in the mouse head (Fig. 2.11 B). A one-dimensional voltage profile in the proximity of the electrodes was plotted to estimate the volume of tissue that was electrically affected/activated (Fig. 2.11 C).

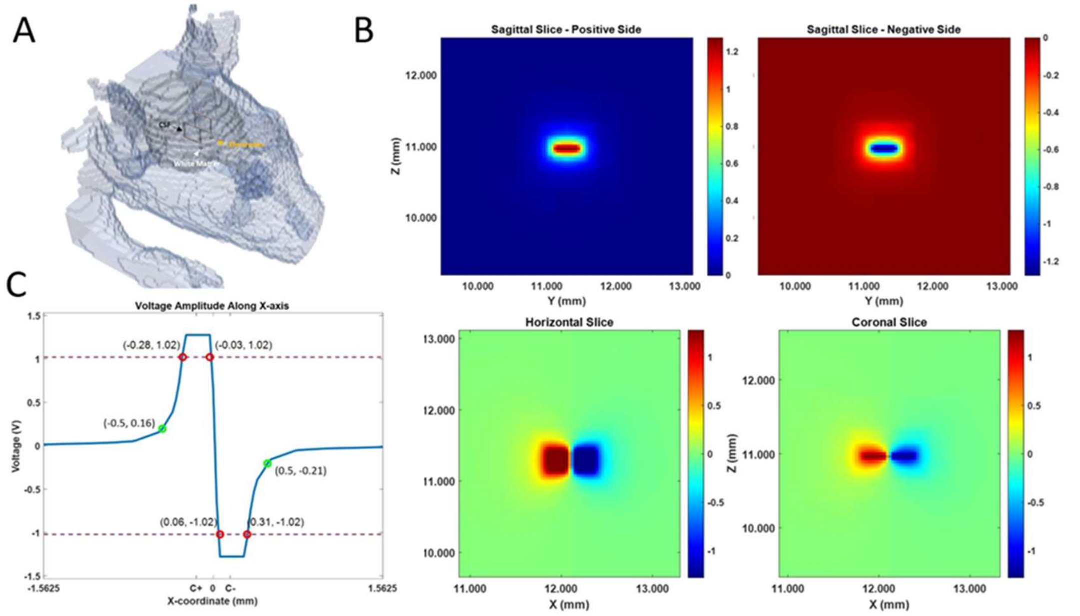

Figure 2.11 A) 3-D illustration of the discretized mouse head model. The bulk tissue model is divided into voxels at a resolution of 31.25 µm. Each voxel represents an equivalent electrical circuit according to its material type. The brain model is mostly uniform as grey matter. The proximity of the medial septal nucleus, where the electrodes are placed, also contains areas of white matter and CSF modeled as basic geometries. B) The voltage mapping near the medial septal nucleus when stimulated with a bipolar electrode configuration. Top row: two sides of the sagittal slice, looking into both the positively and negatively polarized electrodes. Bottom row: the horizontal and coronal slices capturing the voltage distribution around both electrodes. The absolute voltage decays to zero rapidly moving away from the electrodes, demonstrating that the volume of activation is confined within a diameter of about 1 millimeter. C) The voltage amplitude plotted along a single axis. The voltage decay profile moving away from the electrode is very similar along all three axes and the volume of activation can be modeled as a sphere. The "equivalent diameter" for the volume affected by stimulation is approximated by choosing points where the slope is approaching zero (green circles), which determines the current density generated at that location. Thresholding can also be used to visualize the points where the target voltage amplitude is maintained. The red circles label the coordinates at which an amplitude of 1 Volt or more is observed. C+ and C- labels mark the centers of the positive and negative electrodes, respectively.

2.5.3 Data Acquisition

fUSI data were acquired using the *Iconeus One* system (Iconeus, Paris, France). Image acquisition was performed using 128-channel linear ultrasound transducer array, with 15 MHz center frequency and 0.1 mm pitch. This technique enables a large field of view (12.8 mm width, 10 mm depth and 400 μm plane thickness) while maintaining high spatial resolution (100 μm x 100 μm in-plane). The transducer was placed on the intact skull and skin along a sagittal plane on the right side, contralateral to the implanted stimulating electrodes (Fig. 2.1 B). A 60-minute continuous fUSI signal acquisition protocol was employed (Fig. 2.1 C), after 5 minutes, an intraperitoneal (i.p) injection of either 0.2cc of saline or MK-801 (1mg/kg) was given. At the 45-minute mark, mice received either 5 minutes theta (7.7Hz), 5 minutes gamma (100Hz), or no stimulation in the MSN, followed by an additional 10 minutes of fUSI recording (Fig. 2.1 B). This timepoint was chosen as the maximal concentration of MK-801 in the brain when given systemically occurs 40-60 minutes after injection [103]. The MSN was electrically stimulated at gamma and theta under the following parameters: 100 msec square wave pulse width, and current of 80μA using a STG 4008 (Multi-Channel Systems, Baden-Württemberg, Germany). These parameters were chosen because they have previously been shown to improve memory function in animal models of spatial memory impairment [70,72,74].

The target image plane was determined by co-registering a 3D whole-brain fUSI image of each mouse with a standard Allen Mouse Common Coordinates Framework brain atlas utilizing dedicated software available with the Iconeus One system (Fig. 2.9 A) [104]. The probe was fixed steadily throughout experiments on a motorized system with the field of view (FOV) transverse and intersecting the co-registered sagittal plane. Images were obtained from 200 compounded frames acquired with a 500Hz frame rate, using 11 tilted plane waves separated by 2° (from -10° to +10° increment by 2°). These were acquired at a 5500Hz pulse repetition frequency (PRF) using a real-time continuous acquisition of successive blocks of 400ms (with 600ms pause between pulses) of compounded plane wave images.

2.5.4 Data Preprocessing

The Iconeus One acquisition system generates power Doppler (pD) images pre-processed with built-in phase-correlation based sub-pixel motion registration and singular-value-decomposition (SVD) based clutter filtering algorithms [105]. These algorithms were used to separate tissue signal from blood signal to obtain pD images (Fig. 2.12 B). To correct potential physiological and motion artifacts, we adopted rigid motion correction techniques that have successfully been used in fUSI and other neuroimaging studies [105–107]. These were combined with high frequency filtering algorithms to eliminate noise artifacts. We employed a low-pass filter with normalized passband frequency of 0.02 Hz, with a stopband attenuation of 60 dB that compensates for delay introduced by the filter, to remove high-frequency fluctuations in the pD signals.

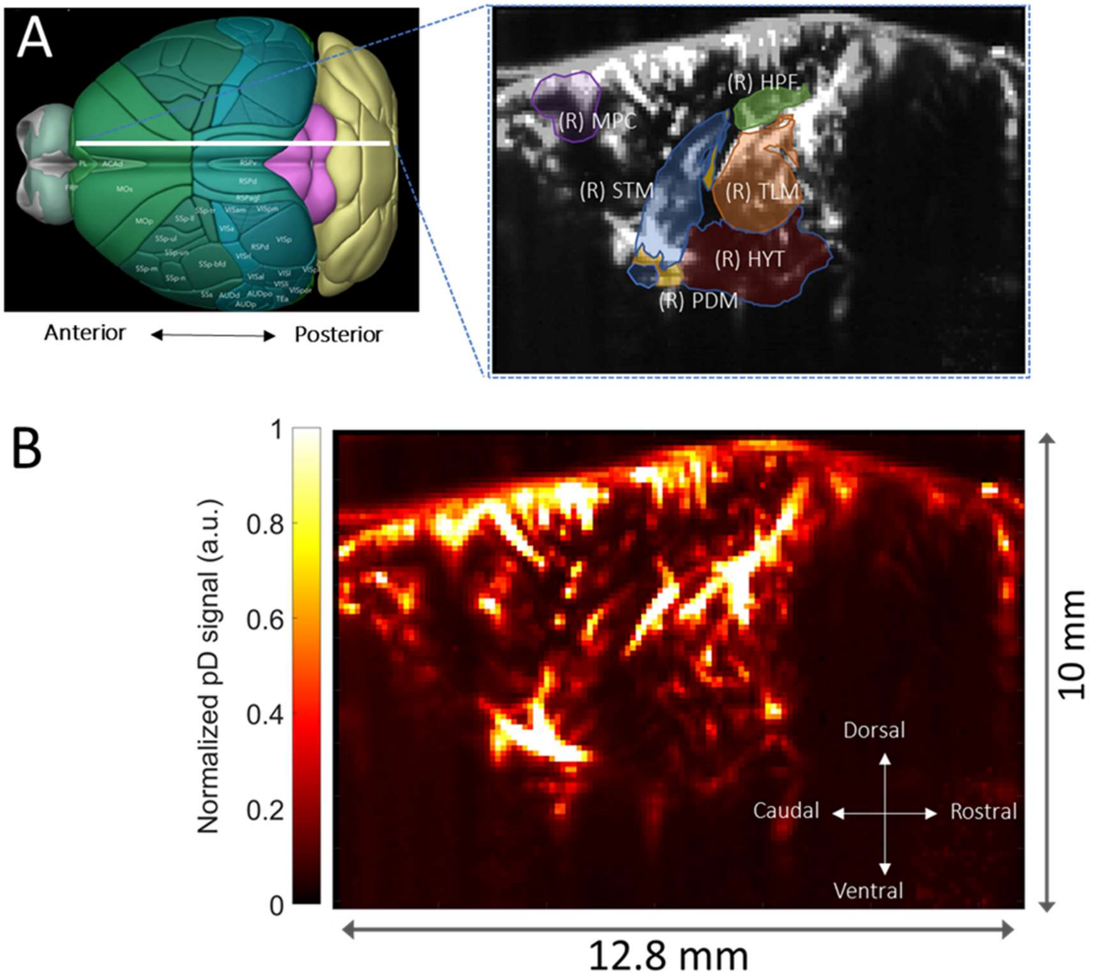

Figure 2.12 Functional ultrasound imaging (fUSI) of the mouse brain. A) 3D mouse brain model with fUSI probe positioning (white bar) and ROIs – hippocampus (HPF), medial prefrontal cortex (mPFC), hypothalamus (HYT), thalamus (TLM), pallidum (PDM), and striatum (STM), superimposed onto a mean grayscale fUSI vascular map of the sagittal mouse brain. B) pD image of cerebral blood volume (CBV) in a sagittal plane (max-min normalized relative scale).

2.5.5 Effects of MK-801 on CBV

We investigated the temporal effects of intraperitoneal MK-801 administration on the septohippocampal circuit (hippocampus, mPFC) and surrounding regions (striatum, pallidum, thalamus, hypothalamus). To do so, we generated event-related average (ERA) time course curves of the CBV changes (ΔCBV) as a percentage change of the pD signal from baseline activity for the selected ROIs. The average pD signal from 2 minutes prior to the saline or drug injection was used as the baseline. We utilized a repeated measures analysis of variance (rmANOVA) to assess the effects and interactions between drug (saline and MK801) and ROI factors over time. We fitted a repeated measures 'within-design' model to the CBV percentage change signals over 42-min interval (including 2 minutes just before the drug injection and the 40 minutes after injection) for each mouse and ROI for the rmANOVA analysis. To further quantify the relative differences in ΔCBV between saline-vehicle and MK-801-treated mice in various ROIs, we used the last 2 minutes of recordings to compute the mean effects-size differences in ΔCBVs and the 95% confidence interval of the effect size (if 95% confidence interval contains zero, then the effect is not significant at the 0.05 level) in each ROI. We also computed the Cohen's d value in each ROI as a measure of the drug effect size that describes the standardized difference between the means of ΔCBVs in the two groups of animals [108]. A Cohen's d value of 0.2 represents a small effect size, 0.5 represents a moderate effect size, 0.8 represents a large size and greater than 0.8 represents a very large size.

2.5.6 Effects of MSN DBS during stimulation on brain hemodynamics

We computed the ΔCBV for each ROI to investigate effects of MSN theta- and gamma-frequency stimulation on the cerebral hemodynamics following saline control or MK-801 injection. We observed ERA time-series of the ΔCBV of each selected ROI relative to the average pD signal acquired 2 minutes prior to stimulation onset to visualize the temporal dynamics of DBS effects to CBVs of the ROIs. We utilized a three-way rmANOVA to assess the effects and interactions between drug (saline and MK801), stimulation (gamma, theta, no-stimulation) and ROI factors across time during the stimulation process. Here, we fit a repeated measures 'within-design' model to the ΔCBV signals over the 7-min period (including 2 minutes prior to stimulation, 5 minutes during stimulation) for each animal and ROI. Subsequently, we computed the mean effects-size differences in ΔCBVs, the 95% confidence interval of the effect size, and the Cohen's d value in each ROI as a measure of the stimulation effect size. We measured the mean ΔCBVs during stimulation in theta [saline: n=16, MK-801: n=12], gamma [saline: n=14, MK-801: n=14], and no-stimulation [saline: n=14; MK-801: n=10] animal groups. The mean ΔCBVs were calculated utilizing the last 2 minutes of pD signal during stimulation across animals in each of the three stimulation categories.

2.5.7 Effects of MSN DBS after stimulation offset brain hemodynamics

We are also interested in assessing the effects of MSN DBS after stimulation offset. To do so, we repeated the same analysis described above, but we used the 10 minutes of pD signal after stimulation offset, plus 2 minutes prior to stimulation onset as a baseline. The mean ΔCBVs were calculated utilizing the last 2 minutes of pD signal after stimulation offset across animals in each of the three stimulation categories. Our goal is to identify whether MSN DBS causes persistent and delayed changes in CBVs within and/or outside the septohippocampal network.

2.5.8 Effects of high dose ketamine on brain hemodynamics

To investigate the capability of fUSI to detect and characterize effects of ketamine-evoked SWA and PPS activity on rat brain hemodynamics, we determine the ΔCBVs for all pixels in the fUSI image, as %pD signal change with-respect-to the last 60 s of baseline activity. We then derive statistical parametric maps to characterize the spatial and temporal responses to SWA and PPS activity. The SPMs provide visualization of regions with significant cerebral blood volume changes caused by SWA and PPS activity. The SPMs are generated based on a pixelwise Student's *t*-test (two-sided with false discovery rate correction) comparison between the two fUSI image groups. To assess the SWA effects, we compare fUSI signal acquired after injection of the first non-anesthetic and before the second injection of non-anesthetic dose of ketamine to the baseline reference activity. On the other hand, to investigate the effects of PPS activity on brain CBV, the SPMs were derived by comparing fUSI signal acquired during the PPS activity periods to signal acquired during SWA periods. We extracted and condensed the fUSI signal acquired during SWA and PPS activity periods into two separate mean 3D image x time matrices, based on the timing of the electrophysiological LFP recordings. Note, to account for potential washout effect – uncertainty in how long it takes for the signal to return to baseline, we use only the last 10 s of the SWA period-signals as reference activity. To assess the temporal evolution of the CBV changes in the activated rat brain regions, we generate ERA time course curves as a percentage change with respect to the baseline reference activity.

2.5.9 Statistical analysis of drug and stimulation effects on ΔCBVs

All the analysis was performed using Matlab Version 9.13.0.2193358 (R2022b). We assessed the drug and stimulation effects and interactions utilizing the Matlab functions 'fitrm' and 'ranova' for the repeated measures model fitting and the rmANOVA respectively. We utilized the Greenhouse-Geisser approximation to correct for the possibility of non-compound symmetry (same variance in means and shared common correlation in paired responses) in the ROI-time series assessed. The mean effect-size differences and the Cohen's d values for the mean difference in ΔCBVs between saline and MK801, as well as the between no-stimulation-gamma, no-stimulation-theta, and gamma-theta were computed with the 'meanEffectSize' Matlab function.

Chapter 3

Functional Ultrasound Imaging of the Human Spinal Cord Under Electrical Stimulation

Reprinted with permission from Agyeman A. K., et. al.

3.1 Abstract

The integration of functional responses in the human spinal cord into the nervous system is not well understood. Herein we demonstrate the first in-human functional ultrasound imaging of spinal cord response to epidural and transcutaneous electrical stimulation. fUSI is a minimally invasive neuroimaging technique that can record blood flow at a level of sensitivity, spatial and temporal precision not previously achieved in the human spinal cord. By leveraging fUSI and electrical spinal cord stimulation in patients who underwent surgery, we recorded and characterized hemodynamic responses of the human spinal cord to an electrical neuro-modulatory intervention commonly used for treating pain, and increasingly used for sensory-motor and autonomic functions. We found that the hemodynamic response to epidural and transcutaneous stimulation reflects a spatiotemporal modulation of the spinal cord circuitry not previously recognized. The impact of this analytical

capability is significant for several reasons. It offers a mechanism to assess blood flow changes with a new level of precision which can be obtained in vivo conditions. Additionally, we demonstrate that fUSI can successfully decode the spinal cord state in a single trial, which is of fundamental importance for developing real-time closed-loop neuromodulation systems. Overall, our work is a critical step towards developing a vital technique to study spinal cord function and understand the potential effects of clinical neuromodulation for spinal cord and other neurological disorders.

3.2 Introduction

The spinal cord is a major sensorimotor integration center within the nervous system. It receives and monitors the kinetics, kinematics, and relative position of all parts of the body [109–113]. Based on this constant bidirectional flow of information the spinal networks provide a function in controlling most movements. Interruption of the bidirectional flow of information within the spinal cord secondary to traumatic injury or disease, at any level of severity, can lead to negative impacts [114]. Deleterious effects include exaggerated reflex activity, chronic pain, partial to complete loss of motor and/or sensory function, bowel/bladder dysfunction, and adverse changes to sexual function [115]. The cumulative effect of these dysfunctions severely impacts millions of individuals world-wide, leading to an immense burden on healthcare systems and national economies [116–120].

Despite the important role of the human spinal cord in sensory, motor, and autonomic functions, little is known about its functional architecture. While functional brain imaging (e.g., fMRI, stereoelectroencephalography [sEEG]) has been studied extensively (motor, sensory, language, memory), research on the functional anatomy of the spinal cord has been limited. The first fMRI studies of the human spinal cord were reported in the late 1990s [121,122].

Since then, a growing but limited number of fMRI studies have attempted to reveal the functional organization of the spinal cord [123–128]. Most importantly, the validity of BOLD signals as a hemodynamic proxy of spinal neural activity was only recently confirmed in non-human primates (NHPs), as signal variations were shown to correlate with electrophysiological activity (i.e., local field potentials) [129]. The paucity of research could be attributed to technical challenges that arise when imaging the human spinal cord, including the small cross-sectional dimension of the cord (10-15 mm in diameter) [130], and susceptibility artifacts due to local magnetic field inhomogeneities created by interfaces between the surrounding bone, ligaments, soft tissues, and cerebrospinal fluid (CSF). Motion artifacts can also arise from the proximity to the thorax, lungs, and neck muscles [131–133]. Optical and electrophysiological techniques that could potentially overcome some of these challenges face inherent limitations in penetration depth and large-scale recordings – i.e., monitoring simultaneously activity from multiple spinal cord areas [134,135]. Given this context, the development of an imaging technology that can illuminate the hemodynamic response of the spinal cord with high spatiotemporal resolution, sensitivity, and penetration depth is imperative. Until recently, no modality has been developed to successfully monitor the spinal cord with these criteria. Recently, functional ultrasound imaging was introduced as a breakthrough modality for simultaneously monitoring hemodynamic activity over large areas of the rodent brain [1–3,23]. It is a minimally invasive technique that provides a unique combination of great spatial coverage, high spatiotemporal resolution, and sufficient sensitivity to detect relative hemodynamic changes of only 2% without averaging over multiple trials. While fUSI is a hemodynamic technique, its enhanced spatiotemporal performance and sensitivity offer substantially closer connection to the underlying neuronal signal than achievable with other hemodynamic methods such as fMRI. Since the first *in vivo* proof-of-concept of fUSI in 2011, successfully imaged cerebral blood volume changes in the micro-vascularization of a rat brain during whisker stimulation [1], fUSI has been utilized in a variety of preclinical and clinical studies to measure brain activity in animals and human under anesthetized and awake conditions [22,27–32]. By combining electrophysiology with fUSI in awake mice, a recent study showed that low-frequency fluctuations (below 0.3 Hz) in pD signal is strongly correlated with neuronal activity [87]. This study established for the first time the direct association between neuronal activity and functional ultrasound signal. Recently fUSI was expanded to image rodent and swine spinal cord responses to different electrical response patterns [33,136–138], providing evidence that fUSI can detect C-fiber-evoked spinal cord hemodynamic responses elicited by activation of either natural noxious mechanical stimulations or electrically activated C fibers [137].

In this study we leverage fUSI to quantify functional hemodynamic changes of the human spinal cord in response to epidural electrical spinal cord stimulation (ESCS) and transcutaneous spinal cord stimulation (TSCS). We monitored the hemodynamic activity of the spinal cord in 7 patients who underwent standard-of-care implantation of an ESCS device under general anesthesia for chronic back pain treatment. By acquiring fUSI of spinal cord activity at the level of the 10th thoracic vertebra (T10) during ESCS (T8-9) or TSCS, we show that stimulation causes strong local hemodynamic changes in the spinal cord. This finding provides evidence that fUSI can capture and characterize evoked changes in human spinal cord blood volume hemodynamics.

We extend these results to accurately predict the effectiveness of a stimulation protocol to evoke hemodynamic changes of the spinal cord at the single-trial level. By utilizing machine learning techniques to extract the most informative signals from the spinal cord that are associated with stimulation, we successfully predict the effects of electrical stimulation on spinal cord hemodynamics. Overall, our findings open avenues to understand spinal cord function and provide a window into understanding the effects and potential of neuromodulation for neurological disorders.

3.3 Results

To assess how electrical stimulation evokes specific changes in spinal cord hemodynamics, we acquired fUSI images from 6 patients who underwent ESCS surgery (T10 partial laminectomy) for chronic back pain treatment (Fig. 3.1 A-B). We used a miniaturized 15-MHz linear array transducer, inserted through a laminar opening onto the dura of the spinal cord with transverse field of view (Fig. 3.2 A). We also acquired fUSI spinal cord signal from one additional patient who received a non-invasive transcutaneous spinal cord stimulation (TSCS) protocol (Fig. 3.1 D). The recordings produced pD ultrasound images of the spinal cord with a spatial resolution of 100 μm x 100 μm in-plane, slice thickness of about 400 μm and field of view (FOV) 12.8 mm x 10 mm. The pD signal intensity images from all patients illustrate part of the anatomical vascularization of the spinal cord with the dorsal surface highlighted with white discontinuous dash line (Fig. 3.2 B–G, 3.6 A).

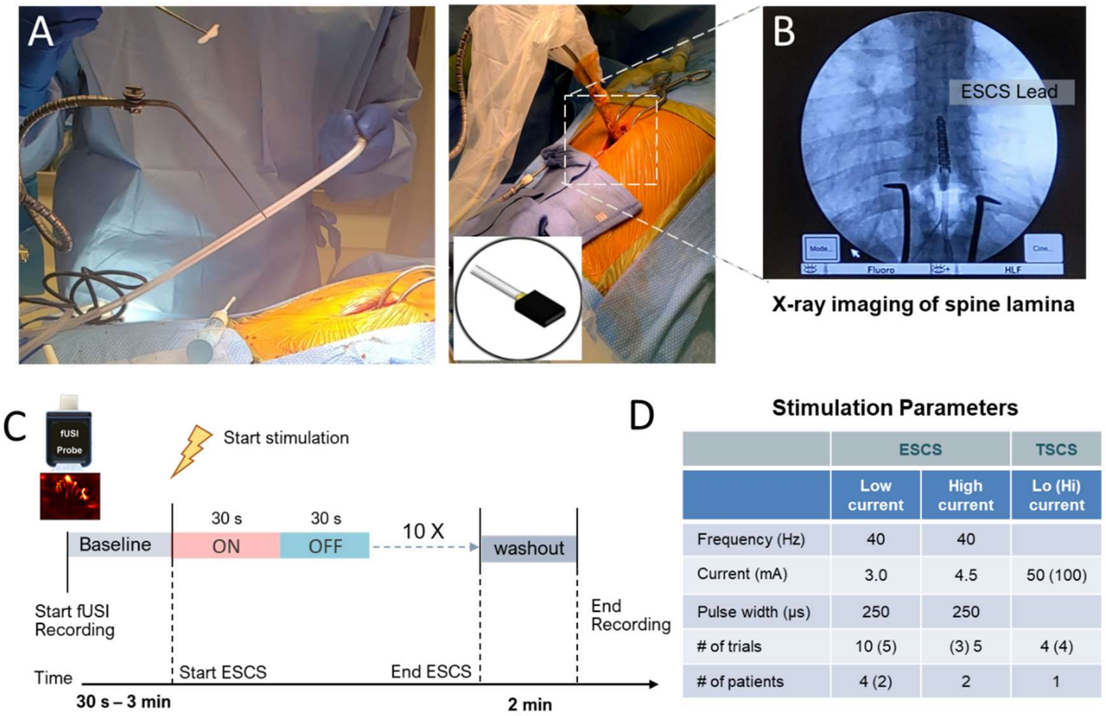

Stimulation Parameters

	ESCS		TSCS
	Low current	High current	Lo (Hi) current
Frequency (Hz)	40	40	
Current (mA)	3.0	4.5	50 (100)
Pulse width (µs)	250	250	
# of trials	10 (5)	(3) 5	4 (4)
# of patients	4 (2)	2	1

Figure 3.1 Surgical procedure, fUSI acquisition and epidural electrical spinal cord stimulation protocol. A) Patients undergo a T10 partial laminectomy for standard-of-care implantation of an epidural electrical spinal cord stimulator (PentaTM model 3228), under general anesthesia. B) Laminectomy and X-ray imaging of the spine lamina. A 15 MHz functional ultrasound probe (inner panel) is inserted into a sterilized cover to reduce the level of microbial contamination. The probe is mounted onto a retractor surgical arm and inserted into the lamina for fUSI. C) Functional ultrasound imaging and ESCS Protocol. Continuous fUSI recording protocol consists of 3 min (n=4) or 30 s (n=2) baseline signal acquisition, followed by acquisition during 10 cycles of ESCS consisting of 30 s stimulation ON and 30 s stimulation OFF trials. D) ESCS and TSCS parameters. All ESCS patients were stimulated at 40 Hz burst-frequency with 250μs pulse-width stimulation. Patients received either 10 cycles all at 3.0 mA (n=4), or 10 cycles consisting of 5 cycles at 3.0 mA followed by 5 cycles at 4.5 mA (n=2). One (n=1) patient received 8 cycles consisting of 4 cycles at 50 mA followed by 4 cycles at 100 mA non-invasive TSCS.

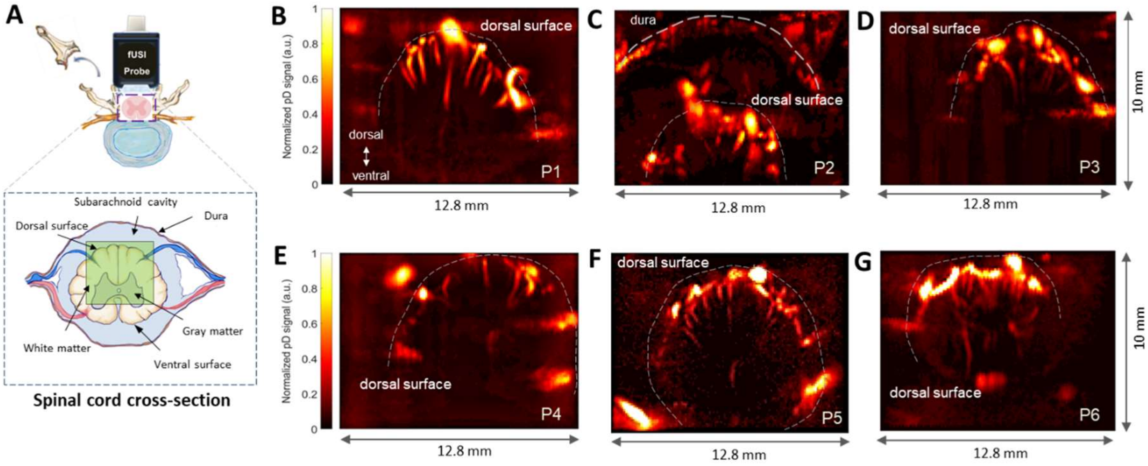

Figure 3.2 Functional ultrasound imaging of the spinal cord in a transverse plane. A) Schematic representation of spinal cord fUSI through a laminar window and cross section of spinal cord anatomy. The green area illustrates approximately the field of view of fUSI acquisition in patient 1. B-G) Power Doppler-based ultrafast ultrasound image showing the transverse section of the spinal cord of patients. The field of view captures part of the anatomical vascularization of the spinal cord with the dorsal surface highlighted with white discontinuous dash lines (and dura in patient 2).

3.3.1 Hemodynamic responses evoked by epidural electrical stimulation

To resolve ESCS-specific hemodynamic changes, we employed a stimulation protocol in which electrodes were placed to span the T8-9 spinal interspace location to deliver 10 ON-OFF cycles, with each cycle containing a 30 s ON period (stimulation ON) and a 30 s OFF period (stimulation OFF) (Fig. 3.1 C). Placement of the stimulator lead in the spinal interspace was confirmed with x-ray imaging (Fig. 3.1 B). A burst frequency of 40 Hz and 250-μs pulse width were utilized. Four patients (P1, P2, P3, and P4) received the same ESCS protocol consisting of 10 ON-OFF cycles of low (3.0 mA) current stimulation. Two patients (P5 and P6) received 2 successive 5 ON-OFF stimulation cycles consisting of low (3.0 mA) and high (4.5 mA) current amplitudes, with 3 minutes pause between the two stimulation protocols (see details, Fig. 3.1 D). A typical hemodynamic response to ESCS in a single stimulation cycle (30 s

OFF, 30 s ON) of patient 4 is illustrated in Fig. 3.3 A (see movie S-vid. 3.1 in the supplementary materials). The mean pD signal (average fUSI activity across the simulation OFF periods) is represented as grayscale image and overlaid with color coded changes of the spinal cord blood volume (ΔSCBV) relative to the baseline activity (i.e., average fUSI activity for 20 seconds preceding the onset of stimulation ON trial for the first time – i.e., 1st cycle of stimulation). The stimulation causes regional changes (mainly increase) in blood flow after stimulation onset (Fig. 3.3 A). Once the stimulator is turned off, blood flow response returns progressively to the pre-stimulation condition. The mean %pD signal averaged across the activated regions relative to the reference (mean of 20 s pD signal preceding onset of ESCS) activity in patient 4 show strong trial-to-trial increases (red) or decreases (blue) in SCBV over time during the stimulation ON periods. After ESCS the pD signal returns to the baseline activity level (Fig. 3.3 B).

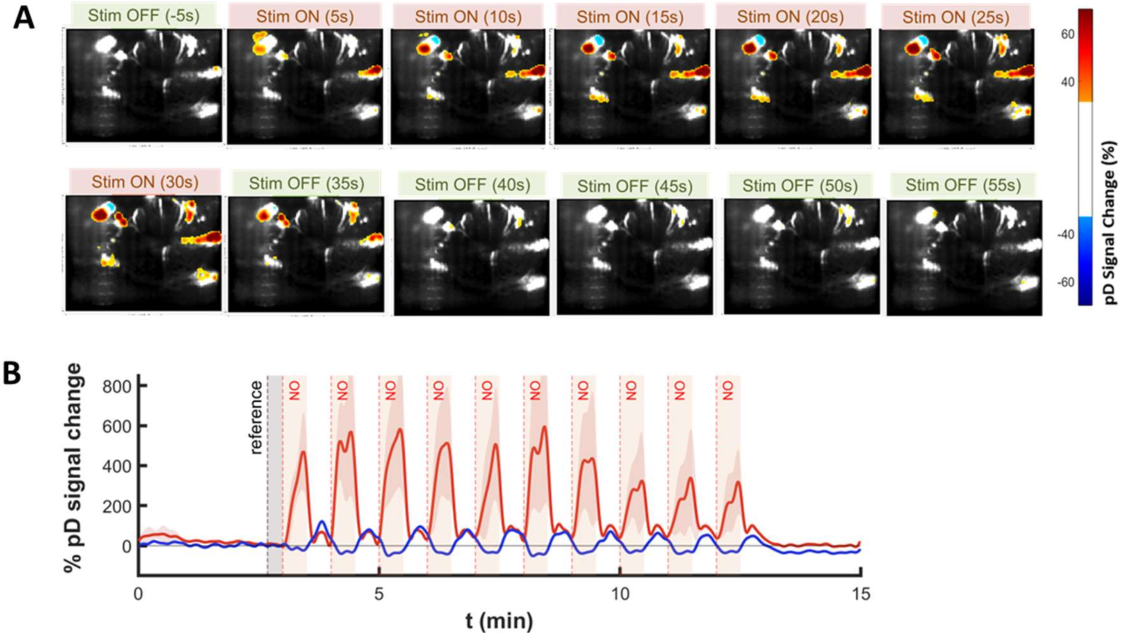

Figure 3.3 Hemodynamic response of the spinal cord induced by epidural electrical spinal cord stimulation within a trial in a typical patient. A) Spatiotemporal spinal cord blood volume change (ΔSCBV) greater than 30% relative to reference activity, color coded on the reference grayscale mean pD images at several time points starting 5 seconds before onset of the stimulation (Patient 4). The reference activity was computed as the average fUSI signal for 20 s prior to stimulation onset. B) Spinal cord temporal mean %pD signal change from trial-to-trial corresponding to pseudo global regions (activated regions with %pD signal change greater than 30%) that exhibit increase (red) and decrease (blue) in SCBV.

To better understand how ESCS evokes specific changes in spinal cord hemodynamics, we compute statistical parametric maps based on two-sided Student's t-test with false discovery rate correction (FDR). The SPMs identify regions recorded within the spinal cord that are strongly affected by electrical stimulation. One way to perform the SPM analysis is to compare the hemodynamic signal between the stimulation ON trials and the baseline activity – i.e., the spinal cord activity before we turn on the stimulation for the first time. The results showed that ESCS causes strong local hemodynamic changes in spinal cord (see Fig. 3.S.3). Importantly, the hemodynamic signal does not return to the baseline activity – i.e., the pre-stimulation activity – during the 30 s stimulation offset (except for P4). This is consistent with evidence that electrical stimulation can result in prolonged clinical and physiological changes after the stimulation is turned off [139,140]. The main pitfall with this analysis is that the baseline activity of the spinal cord no longer exists after the onset of the first stimulation trial. Given that fUSI can be utilized to assess several stimulation protocols within the limited time of spinal cord surgical procedures, we need to implement an alternative way to evaluate the effects of electrical stimulation to the spinal cord hemodynamics. To do so, we perform the SPM analysis between the stimulation ON and stimulation OFF trials. To minimize the washout effect of the electrical stimulation, we compute the SPMs using the signal acquired during the last 6 s of each stimulation OFF trial period – named reference period (Fig. 3.4 A). Additionally, we generate event related average waveforms of the spinal cord blood volume changes (ΔSCBV) as a percent change relative to the 6 s mean reference activity to elucidate the temporal patterns of the hemodynamic changes of the spinal cord during stimulation. The results show that electrical stimulation causes strong regional changes in blood flow in all 4 patients (Figs. 3.4 B–C). We assess the combined (pseudo-global, i.e., the mean activity across activated pixels) response as well as the response of selected ROIs in the SPM activated spinal cord regions. Notably, we observe rising (red and orange curves) and falling (blue curves) ERA curves for selected ROIs with regional-dependent peak responses and peak time induced by electrical stimulation for all patients (Fig. 3.4 A-B). This is followed by a subsequent return to baseline before or immediately after stimulation is ceased. Note that although the temporal responses are similar for the selected ROIs in each patient, they exhibit different peak response (i.e., magnitude of %pD signal change), peak time and recover time. The pD signal rises and peaks faster in certain regions, whereas it exhibits slower responses with peak-increase that occur after stimulation offset in other regions. We also present control curves that show no significant changes in SCBV during stimulation for selected ROIs (light gray Figs.

3.4 A-B). Fig. 3.4 C illustrates the pseudo-global response of the activated regions to summarize the effects of the electrical stimulation to the spinal cord hemodynamics.

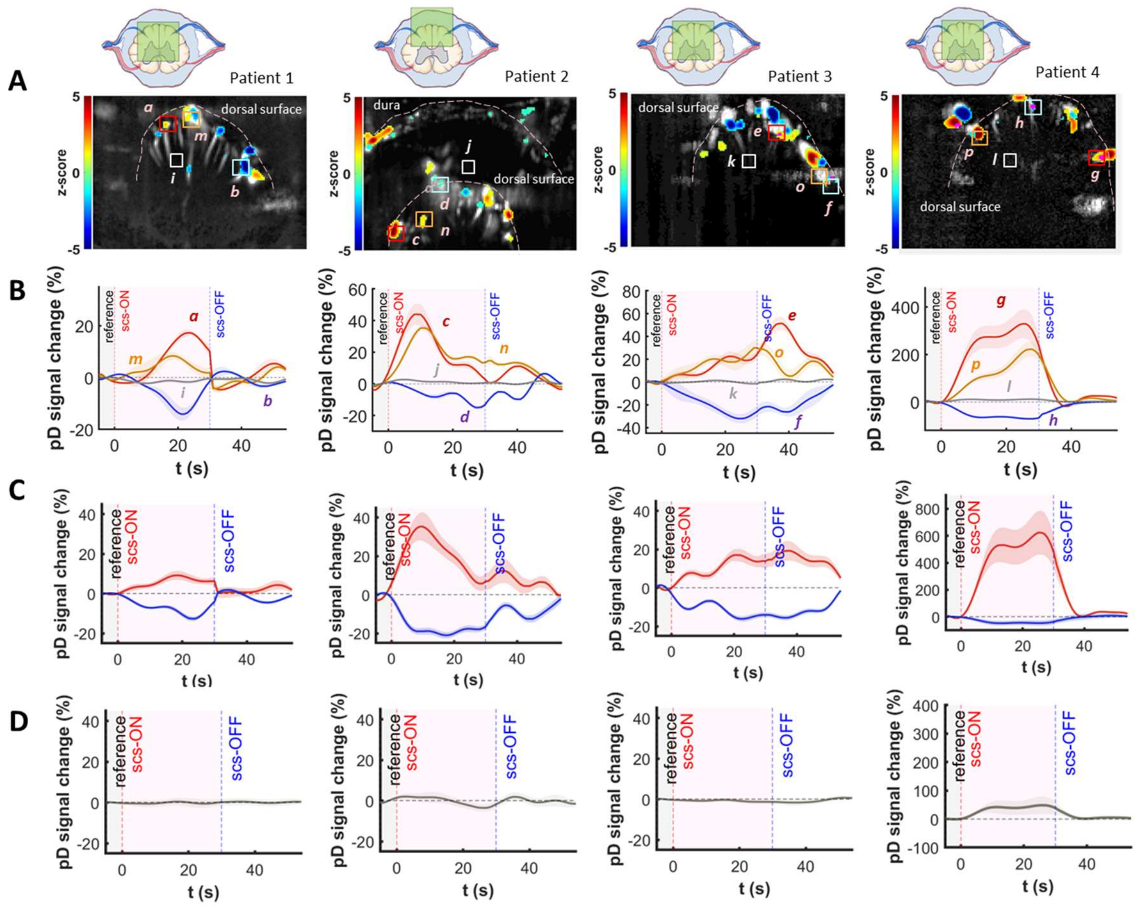

Figure 3.4 Statistical parametric map and event-related average waveforms (Four patients). A) Statistical map shows localized areas with significantly higher or lower SCBV with respect to reference activity during stimulation OFF (two-sided t test of area under the curve, $p < 0.05$, false discovery rate [FDR] corrected for number of pixels in image). SPMs are overlaid on grayscale baseline mean pD intensity images. The top panels illustrate approximately the field of view of the fUSI acquisition for each patient. B) ERA waveforms of selected regions of interest (ROIs) [as indicated with boxes and letters in SPMs – panels A] that exhibit strong increased changes of blood perfusion (red and yellow curves – red and orange boxes) or that exhibit strong decrease change of blood perfusion (blue curves – cyan boxes), after turning on the stimulator. The ERA waveforms corresponding to control ROIs that do not show significant changes in blood perfusion (gray curves – white boxes) after the stimulator is turned on are also displayed. Notice that some ROIs exhibit stronger changes of blood perfusion than others. The background grayscale vascular images in row A illustrate the average power Doppler signal of the spinal cord over the baseline acquisition. C) ERA waveforms of the pseudo-global activated pixels that exhibit strong increased changes of blood perfusion (reddish) or that exhibit strong decrease change of blood perfusion (blueish) in SPMs, after turning on the stimulator. The pseudo-global ERA waveform is determined as the mean %pD signal change across the SPM activated pixels above a threshold (z-score ≥ 0.7) with respect to the reference activity during stimulation OFF trials. D) ERA waveforms of the global SCBV changes of the 4 patients. The global SCBV is determined as percentage change in pD from reference activity of the total FOV of the spinal cord region recorded. The shaded regions around the curves on panels A, B and C correspond to the standard error (SEM) of the power Doppler signal change for averaged over the indicated ROIs across the 10 stimulation trials.

Next, we test the specificity of fUSI in terms of detecting changes in the hemodynamic signal associated with changes in the stimulation protocol. Note that this is a critical step towards developing an ultrasound-based clinical monitoring system to optimize the stimulation parameters. To do so, we recruited two patients (P5 and P6) that received 2 successive 5 ON-OFF stimulation cycles consisting of low (3.0 mA) and high (4.5 mA) current amplitudes, with 3 minutes pause between the two stimulation protocols. Additionally, we acquired fUSI spinal cord signal from one patient (P7) who received a non-invasive TSCS protocol, involving 8 cycles consisting of 4 cycles at 50 mA followed by 4 cycles at 100 mA (Fig. 3.6 A). We repeated the statistical analysis described above to visualize the SPM and the ERA waveforms of ΔSCBV in pixels that significantly increase (reddish regions) or decrease (blueish regions) the pD signal during stimulation (Fig. 3.5). The results showed that the spatial distribution of the activated spinal cord regions remains about the same when we increase the current amplitude of the stimulation from 3.0 mA to 4.5 mA (Figs. 3.5 A and 3.5 B for P5 and Figs. 3.5 C and 3.5 D for patient P6). However, the high current-amplitude stimulation induces stronger hemodynamic changes on the spinal cord (i.e., %pD signal changes) compared to the low current-amplitude stimulation (Fig. 3.5 E–F). These findings suggest that fUSI can differentiate spinal cord hemodynamic responses induced by low and high ESCS current amplitudes.

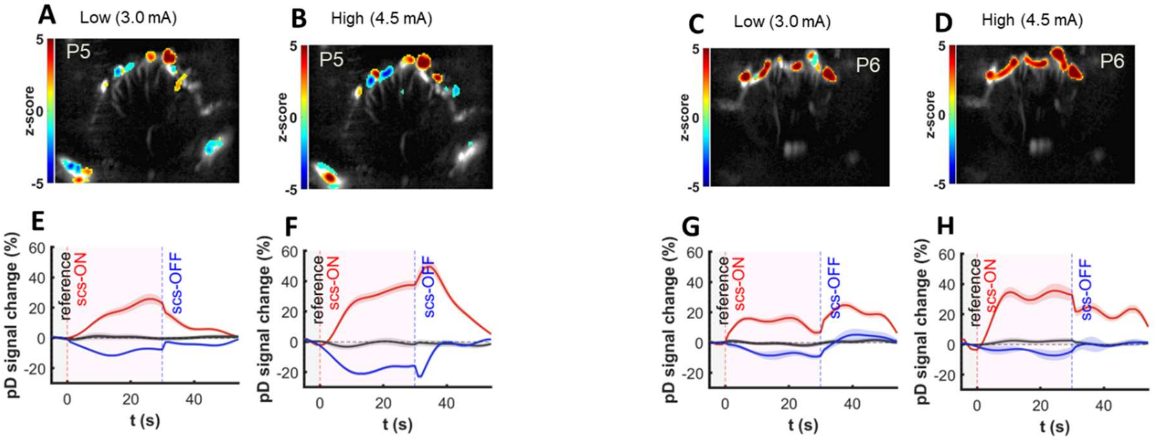

Figure 3.5 Spatial and temporal response to low and high ESCS current amplitudes (Two patients). A-D) Statistical parametric maps that show localized areas with significantly higher or lower SCBV with respect to reference activity during low (3.0 mA – panels A, C) or high (4.5 mA – panels B, D) ESCS (two-sided t test of area under the curve, $p < 0.05$, false discovery rate [FDR] corrected for number of pixels in image). SPMs overlaid on grayscale baseline mean pD intensity images show greater regions of activation (reddish orange) in the high amplitude ESCS (panels B, D), compared to the low amplitude ESCS (panels A, C). E–H) ERA waveforms of the pseudo-global activated pixels that exhibit strong increased changes of blood perfusion (reddish) or that exhibit strong decrease change of blood perfusion (blueish) in the SPMs after turning on the stimulator. The ERAs correspond to the low (panels E, G) and high (panels F, H) current intensity stimulation induced activated regions in the SPMs. The pseudo-global ERA curves correspond to the mean %pD signal change across the activated (reddish – increased SCBV and blueish – decreased SCBV) spinal cord regions and reveal ESCS intensity dependence in both patients. The high current amplitude ESCS achieves higher ERA peaks of the mean %pD signal change (approximately 40 % - panels F, H), compared to peaks of the low current amplitude ESCS ERA peaks (approximately, 20 % - panels E, G). Additionally, there is an intensity-dependence decrease in SCBV, with approximately 20 % peak-decrease in %pD signal change during the high current ESCS (panel F) compared to approximately 10 % peak-decrease in %pD signal change during the low current ESCS (panel E).

Similarly, we observed a stimulation current intensity dependence in the spatial and temporal patterns of the SPMs in the patient who received non-invasive TSCS (Fig. 3.6 B-F). The spatial distribution of the activated spinal cord regions appears to be in the same regions but is wider and more intense when we increase the current amplitude of the stimulation from 50.0 mA to 100.0 mA (Figs. 3.6 B and 3.6 C for P7). This is evident, based on the results that show that the high current-amplitude stimulation induces stronger hemodynamic changes on the spinal cord (i.e., %pD signal changes) compared to the low current-amplitude stimulation (Fig. 3.6 D–F). This finding is very encouraging as it suggests that fUSI can detect and differentiate spinal cord hemodynamic responses induced by a non-invasive TSCS protocol using low and high current amplitudes – demonstrating the specificity of fUSI.

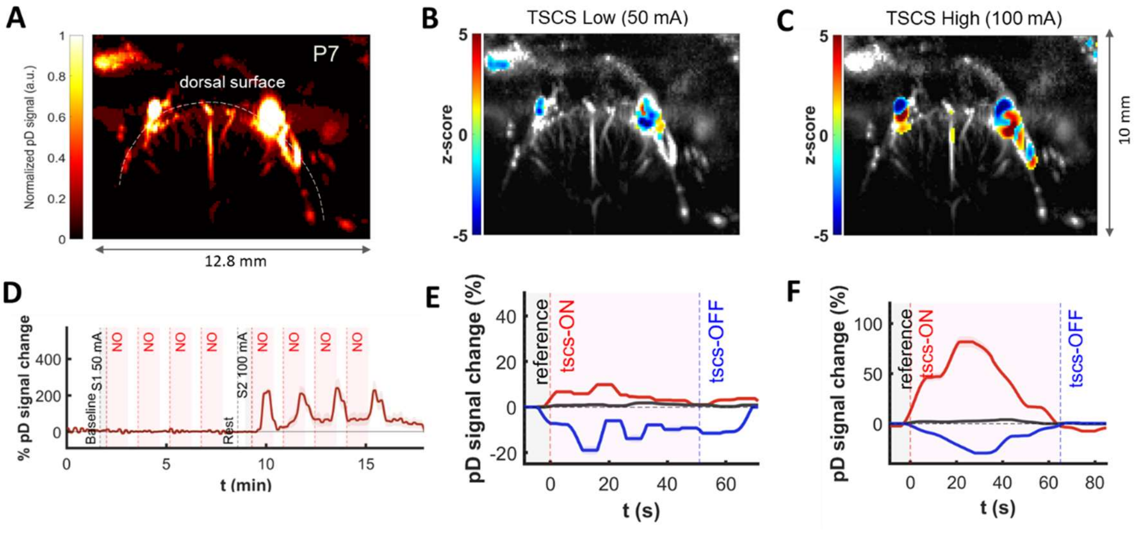

Figure 3.6 Spatial and temporal response to low and high TSCS current amplitudes (One patient). A) Power Doppler-based fUSI image showing the transverse section of the spinal cord (P7). B-C) Statistical parametric maps that show localized areas with significantly higher or lower SCBV with respect to reference activity during low (50.0 mA – panel B) or high (100.0 mA – panels C) TSCS (two-sided t test of area under the curve, $p < 0.05$, false discovery rate [FDR] corrected for number of pixels in image). SPMs are overlaid on grayscale baseline mean pD intensity images show greater regions of activation (reddish orange) in the high amplitude TSCS (panel C), compared to the low amplitude TSCS (panel B). D) Mean %pD signal change of spinal cord signal from trial-to-trial corresponding to pseudo global regions (activated regions) that exhibit increase (red) in SCBV. E–F) ERA waveforms of the pseudo-global activated pixels that exhibit strong increased changes of blood perfusion (reddish) or that exhibit strong decrease change of blood perfusion (blueish) in the SPMs after turning on the stimulator. The ERAs correspond to the low (panel E) and high (panel F) current intensity stimulation induced activated regions in the SPMs. The pseudo-global ERA curves correspond to the mean %pD signal change across the activated (reddish – increased SCBV and blueish – decreased SCBV) spinal cord regions and reveal ESCS intensity dependence. The high current amplitude TSCS achieves higher ERA peaks of the mean %pD signal change (approximately 75 % - panel F), compared to peaks of the low current amplitude TSCS ERA peaks (approximately, 10 % - panel E).

3.3.2 Single-trial decoding analysis.

The capability to evaluate the effects of ESCS on spinal cord hemodynamics without having to perform multiple stimulation trials, and modify the protocol if needed, could have tremendous translational clinical implications. Intuitively, the simplest way to evaluate whether a stimulation protocol evokes hemodynamic changes of the spinal cord would be to measure the ΔSCBV of the whole recorded spinal cord region (named global ΔSCBV). However, this seems to be problematic since the hemodynamic changes evoked by stimulation vary across spinal cord regions. Blood flow in certain regions takes longer to increase (or decrease), whereas other regions exhibit faster induced blood flow changes. Additionally, while some regions show increases, others show decreases in blood flow during stimulation. The ERA waveforms of the global ΔSCBV of the 4 patients (Fig. 3.4, row D), is consistent with our prediction that electrical stimulation does not always cause clear changes of the global SCBV, even after averaging across multiple trials. This suggests that the global ΔSCBV may not reflect a reliable measurement to assess whether a stimulation protocol causes hemodynamic changes on the spinal cord. Hence, a more sophisticated analysis is needed to characterize the electrical stimulation effects on hemodynamics.

One of the great advantages of fUSI is the ability to detect regional hemodynamic changes of only 2% without averaging over multiple trials [27]. Thus, we explored whether fUSI can predict the effect of electrical stimulation on hemodynamics of the spinal cord within a single trial. To do so, we implemented a class-wise principal component analysis (cPCA) to extract effective discriminant features (Fig. 3.7). That is, we reduced dimensionality of the fUSI images by selecting spinal cord regions that exhibit the highest pD signal difference between stimulation ON and stimulation OFF trials and optimally discarded shared information – i.e., noise between class 0: stimulation OFF and class 1: stimulation ON (Fig. 3.7). cPCA has been used to reduce sparsity and dimensionality while maintaining enough components to retain over 90% variance in the data (see Materials and Methods section for more details). It is ideally suited for discrimination problems with large dimension and small sample size including natural and biomedical images [141,142]. Finally, to predict the stimulation induced states of the spinal cord, we used linear discriminant analysis (LDA), where 75% of the event aligned (stimulation ON and stimulation OFF) trials fUSI images were randomly selected to train the model with 25% hold-out test dataset. Note that patients P5 and P6 were not involved in the single-trial analysis due to the low number of trials (i.e., 5 trials with 30 s stimulation ON and 30 s stimulation OFF, each) for each stimulation protocol. The results of bootstrapping (100 iterations) and cross-validated accuracy show that the performance accuracy of the decoding algorithm for the four patients is P1 = 87.1%, P2 = 73.2%, P3 = 82.7%, P4 = 94.4%, (Fig. 3.8A) – i.e., 84.0 ± 11.4 % across the 4 patients (MEAN ± STD). Interestingly, data from P2, where the size of the partial laminar opening did not permit deeper insertion of the fUSI transducer closer to the dorsal surface of the spinal cord, gave the lowest decoding accuracy. Conversely, P4 who showed the strongest ΔSCBV during stimulation period gives the best decoding accuracy.

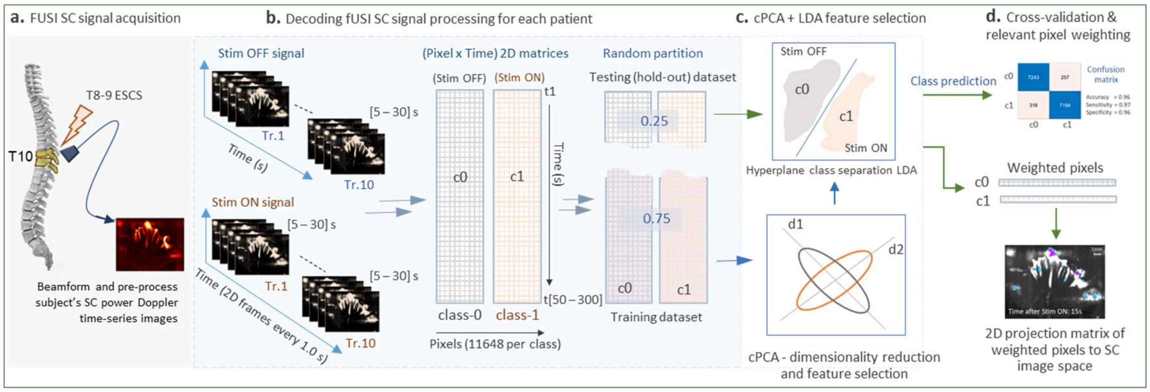

Figure 3.7 Flowchart for single-trial stimulation state decoding from the fUSI signal. Training images were separated from testing images based on the cross-validation technique used – i.e., 75% training data and 25% test data from each class. The state of the spinal cord was decoded from single trials based on a cPCA dimensionality reduction algorithm and a LDA classification model built by the training pD spinal cord imaging data with the corresponding class labels (i.e., C0: OFF stimulation, C1: ON stimulation).

To analyze the temporal evolution of the stimulation-related information in the spinal cord, we attempted to decode the state of the spinal cord across the stimulation time. We used a 1-s incremental window of data to train the classifier and then attempted to decode the state of the spinal cord using pD test images acquired within that window. For example, for t = 10 s, we trained the classifier using pD images of both classes from t=1-10 s (where t = 1 s corresponds to one second after stimulation onset for ON trials and after ceasing the stimulation for OFF trials), and then, we attempted to decode the state of the spinal cord using pD images acquired within that 10 s window. The resulting average cross-validation accuracy curve across patients shows that the classification performance increases with the stimulation time (i.e., training window), reaching a plateau at around 15 s after stimulation onset, but then decreases when more than 25 s imaging data are accumulated to train the classifier (Fig. 3.8 A). Note that the decoding accuracy curve represents the average decoding accuracy across the 4 patients. Fig. 3.S.4 A depicts the decoding accuracy as a function of the training window for each patient. The individual analysis showed that patients (i.e., P1, P2 and P4) in which the pD signal rises faster to the maximum value after turning on the stimulation, the decoding accuracy peaks when a shorter than 30 s time window is used to train the classifier. On the other hand, in patient P3 in which the pD signal exhibits a slower response and peaks after stimulation offset, the decoding accuracy increases with the size of the training window. Distinct spatial locations within the spinal cord encode stimulation-related information as reflected in the variable weighting assigned to each pixel in the decoding algorithm (Fig. 3.8 D). Notice that the spinal cord regions that encode stimulation-related information vary with stimulation duration (i.e., the amount of data used to train the classifier). Additionally, the activated maps generated by the SPM analysis (i.e., pixels with high z-scores) and the machine learning algorithm (i.e., pixels with high decoder weights) show some differences. We hypothesize that the reason is that the SPM method performs a pixel-by-pixel analysis using only the average pD signal between the two classes (stimulation OFF vs. stimulation OFF) to identify regions that exhibit the strongest hemodynamic signal induced by stimulation. On the other hand, the machine learning algorithm considers not only the amplitude of the %pD signal change, but also the spatiotemporal patterns of the whole pD image to extract features in a lower dimensional space that best separate the two classes (see supplementary materials for more details).

Together, these findings suggest that the amount of data used to train the classifier is critical for the decoding accuracy of the spinal cord state. As such, the next step is to determine the time point after stimulation onset when the classifier achieves the maximum decoding accuracy for a given amount of training data (i.e., training window). This analysis aims to find the time point after stimulation onset in which the pD images provide the best discrimination between the two classes. To do so, we used a 1-s incremental window of data to train the classifier as before, but now we attempted to decode the state of the spinal cord using pD test images acquired at a specific time point t within the time window that the classifier was trained. For instance, when the classifier is trained using pD images within a window t=1-5s, the decoding accuracy is evaluated at time t=1, 2, 3, 4, and 5s. The results of average decoding accuracy across patients for pD images (i.e., test data) acquired at specific time instants within the training window, show that the best decoding accuracy (98.3%) is achieved at t = 17 s after turning on the stimulation for a classifier trained using t=1-24s pD images (Fig. 3.8 B). Overall, these findings provide strong evidence that fUSI can evaluate the effectiveness of a stimulation protocol to induce hemodynamic changes within single trials, opening new avenues in closed-loop neuromodulation technologies.

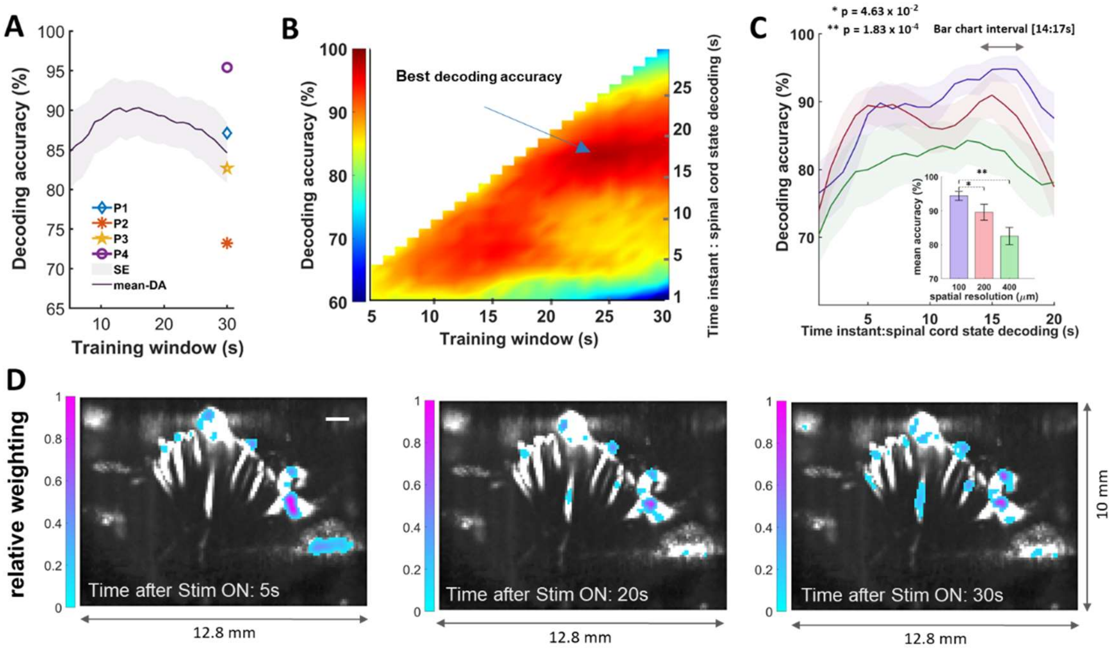

Figure 3.8 Single-trial decoding of the spinal cord state. A) Average decoding accuracy across patients as a function of the amount of data used to train the classifier – i.e., time after the stimulation onset - training window. Indicated are the decoding accuracies of each patient, when 30 s of stimulation ON and 30 s of stimulation OFF data, across the 10 trials, is used for the decoding algorithm (P1=87.1, P2=73.2, P3=82.7, P4=94.4 % – point plots). B) Decoding accuracy of the spinal cord state using pD images acquired at specific time points after turning on the stimulation (with time step 1 s) as a function of the amount of data used to train the classifier (i.e., training window). For instance, we train the classifier using a set of pD images between t=1-5 s and evaluate the decoding accuracy of each second – 1s, 2s, 3s, 4s, and 5s. C) Decoding accuracy of the spinal cord state for pD images acquired between 1s and 20s after turning on the stimulator – i.e., training window of 20s. Different traces correspond to the decoding accuracy of different spatial resolutions (100 μm, 200 μm and 400 μm) of the pD images, averaged across patients (n=4) The shaded regions around the curves correspond to the standard error of the decoding accuracy curves averaged across patients. Inner panel: Mean decoding accuracy as a function of spatial resolution determined over the 100 μm resolution interval of peak accuracy (14:17 s test time instants within the training window). The mean decoding accuracies across patients over this interval were compared. The 100 μm resolution pD images perform significantly better than the 200 μm ($p = 0.0463$) and 400 μm ($p = 0.000183$) resolution images over the selected interval. D) Representative decoder weighting maps (patient 1). The top 10% most heavily weighted pixels are illustrated as a function of space and time after the stimulation onset, overlaid on grayscale mean pD baseline intensity vascular map

3.3.3 Vascular signal and information content in the human spinal cord

To evaluate the benefits of enhanced spatial resolution in studying the human spinal cord, we attempted to decode the spinal cord state using 1-20 s window of pD images to train the classifier while decreasing the resolution of the images. We resized the images using a nearest neighbor interpolation approach to achieve spatial resolutions of 200 μm and 400 μm – the original resolution of the pD image is 100 μm. We then used the downsized images, which contained fewer pixels than the original images, to decode the spinal cord state. The results show that the decoding accuracy decreases as pixel size increases (Fig. 3.8 C). Additionally, we selected the interval of peak accuracy (i.e., between 14 to 17 s test time instants within the training window) for the 100 μm resolution pD images, to compare the mean decoding accuracy as a function of spatial resolution. One-sided Student t-test shows that the 100 μm resolution fUSI images perform significantly better than the 200 μm ($p = 0.0463$) and 400 μm ($p = 0.000183$) resolution images over the selected interval (Fig. 3.8 C, Inner panel). Together these findings highlight the importance of high spatial resolution in studying the human spinal cord.

We also assessed whether the most informative power-Doppler content, useful for decoding the spinal cord state, is found within small or large vessels. To do so, we ranked-ordering all pixels based on the reference (6 s signal acquired prior to onset of stimulation ON trials) fUSI recording mean pD signal in the spinal cord images and segmented them into deciles. This resulted in spatial maps of ranked deciles (Fig. 3.9 A), which indirectly correlate with spinal cord blood flow and vessel size – deciles 1-5 approximately capture small vessels, while deciles greater than 6 correspond to large arteries. We subsequently utilized each decile to independently classify the spinal cord state (i.e., stimulation OFF vs. stimulation ON) and then evaluated for corresponding normalized classification accuracy. In this analysis the classifier was trained using pD images acquired during 20 s acquisition period – i.e., time window 1-20s. We chose this time window, since it provides better decoding performance than using the total time of 30 s (see Fig. 3.8 A). The decoding accuracy increases with increasing deciles and declines when only large-artery deciles (> 6) are used for the classification analysis. Peak accuracy (0.93 ± 0.018; MEAN ± SEM) was observed when the 4th-mean pD ranked deciles are only used to classify the spinal cord state across patients (Fig. 3.9 B) – a 10.24% increase in the average across patients decoding accuracy, compared to when the entire spinal cord image is used. Fig. 3.S.4 B presents the decoding accuracy as a function of the pD signal intensity for each patient.

Additionally, we compared the mean decoding accuracies of decile-ranges 1-2, 3-5, 6-8, and 9-10, corresponding to the smallest, small-medium, medium-large, and largest-vessel groups imaged. We found the mean decoding accuracy of the 3rd to 5th deciles (small-medium vessels) is significantly greater than the mean accuracy of the largest vessels – 9th to 10th deciles ($p = 0.0041$, with correction for multiple comparisons), based on a one-sided Two-Sample t-test (Fig. 3.9 B, Inner panel: bar chart).

The results are consistent with our hypothesis that the most informative pD hemodynamic content is linked to smaller vessels (i.e., arterioles and capillaries, and potentially small arteries). This observation is a unique outcome that could generate important cues in optimizing human spinal cord neuromodulation, akin to observations in recent NHP [28], rodents [99], and ferrets [143] brain studies.

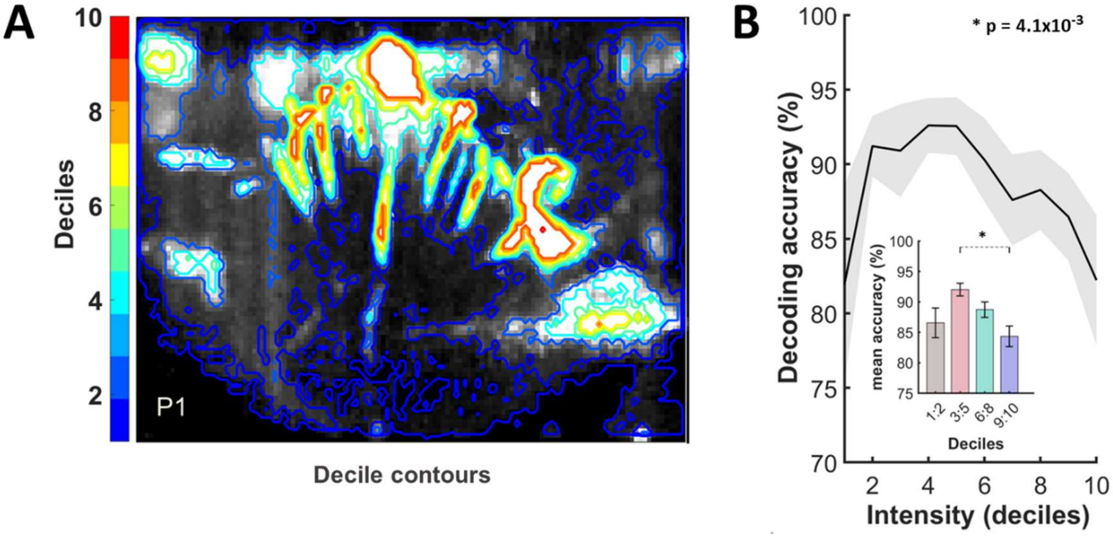

Figure 3.9 Effects of mean pD intensity in single-trial decoding analysis. A) A vascular map of patient 4 with contours dividing the image into deciles of mean pD intensity. B) Mean decoding accuracy (Stimulation ON vs. Stimulation OFF) as a function of deciles (pD intensity sub-divisions) across all patients (shaded area represents standard error [SEM]). Decoding accuracy peaks around quantile 4, which mostly contains small vasculature within the spinal cord. Smaller vessels and primary unit vasculature (i.e., deciles 1 and 10, respectively) carry less information about the effect of the ESCS on spinal cord blood flow. Mean decoding accuracy of decile-ranges (1-2, 3-5, 6-8, and 9-10: smallest, small-medium, medium-large, and largest vessels). The decoding accuracy of the 3rd to 5th deciles (small-medium vessels) is significantly greater than the mean accuracy of the largest vessels – 9th to 10th deciles ($p = 0.0041$).

3.4 Discussion

3.4.1 General

Functional neuroimaging has greatly expanded knowledge about brain function with significant scientific and clinical implications. In contrast, functional spinal cord neuroimaging is far less developed due to technical challenges. Here, we utilized fUSI to image physiological manipulation of the spinal cord through ESCS in patients who undergo spinal cord surgery for chronic low back pain treatment. In contrast to most spinal cord neuroimaging studies that focused on the cervical level [122,127,144–148], we imaged at T10 thoracic level which correlates with the rostral segments of the lumbar cord. It is the area where spinal locomotor networks are located, including interneurons that contribute to central pattern generators. These interneurons control much of the movement of the abdominal muscles and injury at this level can result in deficits in lower limbs, bladder, bowel, and sexual functions. Our results demonstrate that electrical stimulation causes regional changes in spinal cord hemodynamics, with certain regions that exhibit significant increases and others significant decreases in blood flow. By leveraging the enhanced combination of spatiotemporal resolution and sensitivity of fUSI, we show that this modality can accurately predict the effects of a stimulation protocol to the blood volume dynamics within a single trial.

3.4.2 Evaluating the effectiveness of spinal cord stimulation protocol

The ability to rely on the accuracy of a single-trial is necessary if one intends to use fUSI signals to monitor moment-to-moment hemodynamic changes. A single trial fUSI study was recently conducted to predict motor intention in NHPs that perform reaching and saccade (i.e., eye movements) to peripheral targets [28]. By recording hemodynamic activity over the posterior parietal cortex, an association cortical region that encodes planning of actions, fUSI detected which effector the animals intended to use (eye or hand) and which direction they intended to move. These results show that fUSI is capable of imaging hemodynamics in large animals with enough sensitivity to decode the timing and goals of an intended movement. Building on this study, we designed a linear classifier that decodes fUSI signals of the spinal cord to accurately predict the effectiveness of a stimulation protocol to induce hemodynamic changes within a single trial. Importantly, we showed that the best decoding accuracy of the spinal cord state is achieved using less than 30 s stimulation ON/OFF period data to train the classifier. This finding suggests that hemodynamic changes induced by ESCS peak before turning off the stimulator and become less potent with time, impairing the decoding accuracy of the spinal cord state. Overall, these findings provide proof-of-concept that fUSI can detect changes of spinal cord hemodynamic responses induced by electrical stimulation within single-trials.

3.4.3 Functional ultrasound imaging to guide neuromodulation treatment.

Detecting and characterizing the effects of electrical stimulation is crucial to unravelling the complex mechanisms of action subserving chronic back pain suppression. Chronic back pain represents the leading cause of disability worldwide, affecting an estimated 540 million people at any given time [149]. Over the past couple of decades ESCS has emerged as a neuromodulation tool to treat chronic pain conditions that are refractory to traditional therapies [150], such as opioid analgesics, and physical therapy [151–155]. While spinal cord stimulation is effective for many patients, it is often associated with suboptimal efficacy and short-lived therapeutic effects [156]. Some patients do not tolerate the persistent perception of paresthesia, while others do not obtain adequate pain relief from the stimulation. Predicting which patients will not have a resolution of pain remains challenging, mainly because the mechanism of action by which ESCS alleviates pain remains unclear [157]. Although our study does not aim to elucidate the MOA of ESCS for chronic back pain treatment, it suggests that fUSI has considerable potential in gaining a better understanding of the MOA, since the precise association between blood flow changes induced by ESCS and pain modulation is still under debate. A recent study examined the hemodynamic response of the spinal cord evoked by external stimulation and found that pain alters the provoked and unprovoked hemodynamic response of the spinal cord [137] . Hence, it is likely that ESCS treatment that reduces pain may also alter spinal cord hemodynamics. The ability to accurately quantify blood flow in the spinal cord and/or brain networks both temporally and spatially and the increasing numbers of technologies available to modulate neural circuitry seem to be a logical clinical strategy to define MOA of pain and enhance therapeutic efficacy. This may require critical monitoring of the spinal cord and/or brain during modulation with high spatiotemporal resolution and sensitivity systems. Additionally, fUSI could potentially play a major role in identifying the MOA through which functional bidirectional connectivity across a functionally “complete” spinal injury can be reestablished with spinal neuromodulation techniques [112]. Overall, fUSI is a technology that can image the spinal cord with high spatiotemporal resolution and high sensitivity to slow blood flow during surgical operations and can be proved as a useful tool to improve the efficacy of electrical stimulation by optimizing stimulation parameters based on the stimulation-evoked spinal cord hemodynamic signal.

3.4.4 Revealing functional organization of spinal cord in animal studies

While our study constitutes a novel characterization of the hemodynamic signal of the human spinal cord, recent animal studies have also utilized fUSI to characterize spinal cord hemodynamic response evoked by electrical and natural stimulations [33,136–138]. These studies showed that fUSI offers better sensitivity in detecting and characterizing the spinal cord hemodynamic response during subthreshold-to-threshold motor response compared to electrophysiological assessment. fUSI has also been utilized in exploring the effects of inflammatory chronic pain in the spinal cord hemodynamics [137], and in characterizing structural and functional vascular alterations after spinal cord injury in rats [158] Although these studies are insightful, they are based on animal models which limit the interpretability and the applicability of the findings to human populations. Our study is the first to successfully quantify fUSI activity in the human spinal cord with just a single trial of data. Compared to previous animal studies that used multi-trial detection of electrical spinal cord stimulation, detecting the effects of spinal cord stimulation from a single trial represents a new standard for closed-loop neuromodulation systems using fUSI technique.

Challenges and limitations in clinical neuroimaging using fUSI

3.4.5 Invasiveness nature of fUSI

While fUSI represents a novel and promising neuroimaging technique, it remains minimally invasive to invasive in most preclinical and clinical applications – with few exceptions such as in young mice (8-12 weeks old in which the skull is thin) [159] and in pediatric fontanelle-imaging [31]. Surgical procedures to produce a craniotomy [22] or thinned-skull window [26] or laminectomy in the spinal cord [137] is required to harness the full benefits of the enhancements in fUSI spatiotemporal resolution and sensitivity to slow blood flow. This can limit its application to certain studies in which invasive procedures are not allowed (e.g., healthy neurotypical populations). However, the promise of fully noninvasive fUSI is imminent. For instance, a recent fUSI study with intravenously injected microbubbles contrast agents and a phase array transducer with low (i.e., 2 MHz) center frequency enabled transcranial imaging of deep vasculature (6-7 cm) in the adult human brain and the quantification of the hemodynamic signal [160]. On the other hand, certain surgical operations, and clinical neuromodulation therapies, such as brain resection for controlling epileptic seizures, deep brain stimulation for Parkinson's disease and ESCS for failed back surgery syndrome (FBSS), involve surgical procedures in which a craniotomy or laminectomy is performed to expose the brain and the spinal cord, respectively. These invasive surgical procedures offer the unique opportunity to study the human nervous system using fUSI and to develop ultrasonic imaging-based techniques to guide the surgical and neuromodulation treatments.

3.4.6 Clinical challenges

While it is common in animal spinal cord studies to perform large laminectomies, retract back muscles and remove connecting tissues [33] to improve the quality of the ultrasound images, clinical studies are constrained by strict intraoperative surgical protocols. In our study, patients underwent standard-of-care implantation of a spinal cord stimulator for chronic back pain treatment, whereby modification to the surgical procedure (e.g., expand or change the orientation of the laminectomy) to improve the quality of the ultrasound images is not permitted. The surgical procedure involves only partial and small laminectomies to implant the paddle leads and avoid spine destabilization – the frequency of iatrogenic instability is proportional to the width of the laminectomy [161]. In particular, the width of the laminar opening (about 11 mm) was smaller than the width of the ultrasound probe (12.8 mm) and consequently the probe did not perfectly abut to the dura. Furthermore, the size of the laminectomy prevents us from using modern 2D ultrasound probes [99] that can generate 3D pD images, leading to improvement in coverage. Additionally, the orientation of the laminectomy under the clinical protocol only allows for acquisition of pD images in the transverse plane. On the other hand, most animal studies that explored the effects of external stimulation to spinal cord hemodynamics, acquired pD images along the sagittal plane – as Claron et al [137] pointed out "experiments of functional activation in the transverse plane are challenging to perform due to increase amount of background noise compared to the sagittal plane". This option was not available in our study. Together, these intrinsic intraoperative clinical constraints may explain why animal ultrasound imaging studies provide better quality spinal cord images.

Furthermore, clinical limitations prevent us from imaging the same 2D spinal cord plane across patients. Specifically, the depth of imaging planes in patients 1, 3, 4, 5 and 6 are deeper (approximately 6 mm) than the depth of the imaging plane in patient 2 (Fig. 3.4 A top row) and patient 7 (Fig. 3.6 A). The size of the partial laminar opening in patients 2 and 7 did not permit deeper insertion of the fUSI transducer closer to the dorsal surface of the spinal cord. However, although the imaging planes vary across patients, we were able to acquire pD images from the human spinal cord, characterize the hemodynamic changes induced by the ESCS and predict the state of the spinal cord within a single trial with more than 90% cross-validated accuracy. These findings highlight the strength of fUSI technique to overcome the potential to image different 2D slices between experimental sessions and patients.

3.4.7 Optimizing pulse sequence and data processing.

The current study was performed using the Iconeus One scanner in which the fUSI pulse sequence is optimized for rodent brain imaging. In the future, the pulse sequence and data processing can be optimized for human spinal cord imaging. In particular, the current pD images are generated by integration over 400 ms compounded ultrasound images (at 500 Hz). This 400 ms period has been optimized to cover about 5 heartbeats pD image in rodents, which allows for averaging of diastole-and-systole-related variations in the blood volume. To account for the human's heartbeat, which is around 5 times slower than the rodents' heartbeat, we can increase the integration time from 400 ms up to 1 s to generate the pD images. Additionally, the low-cutoff singular value threshold for tissue rejection in the singular-value-decomposition clutter filtering has been selected based on the rodent brain image quality. In the future, both the integration time and the low-cutoff singular value threshold will be calculated to optimize the contrast-to-noise ratio for the human spinal cord imaging based on the standardized approach proposed by Baranger et al [24]. Finally, it is important to design thinner ultrasound probes that fit better within the laminar window – which is about 11 mm in patients with FBSS – and abut to the dura.

Conclusions

We demonstrate the first in-human quantitative evaluation of spinal cord hemodynamics using functional ultrasound imaging. By combining fUSI and epidural ESCS it was possible to measure and characterize the spatially specific hemodynamics of the spinal cord. We describe a single-trial analysis to predict the effectiveness of a stimulation protocol to modulate the hemodynamic signal of the spinal cord. We also show that functional information useful for decoding the spinal cord state (i.e., stimulation ON vs. stimulation OFF) is primarily located in the small vessels within the imaging plane. As ongoing developments of fUSI hardware and software enable real-time imaging and processing, we can develop translational clinical monitoring systems that will help to evaluate the effectiveness of ESCS and other therapeutic neuromodulation strategies – a technology that currently does not exist. Overall, this work establishes fUSI as a promising platform for neuroscientific investigation with potential for profound clinical impact.

3.5 Materials and methods

3.5.1 Patients and surgical procedure

Seven patients underwent standard-of-care implantation of a SCS paddle lead (PentaTM model 3228) for treatment of chronic back pain conditions. Patients were recruited from the Department of Neurosurgery at the Keck School of Medicine of the University of Southern California (USC) and underwent a T10 partial laminectomy for insertion of a spinal cord stimulation paddle lead in the prone position, under general anesthesia. Once the location of the epidural lead was confirmed with fluoroscopy (lead spanning the T8-9 interspace) and x-ray imaging, the fUSI probe was attached to an articulating arm and placed over the spinal cord for transverse imaging (Fig. 3.1 A-C). The ESCS leads were then sterilely attached to an external pulse generator. Patients were eligible for inclusion if they were diagnosed with FBSS. MRI spinal cord anatomical images acquired from the patients before surgery to confirm that chronic back pain is not caused by spinal stenosis (for a typical spinal cord MRI image see Fig. 3.S.6). Informed consent was obtained from all patients after the nature of the study and possible risks were clearly explained. All experimental procedures were approved by the USC Institutional Review Board.

3.5.2 Functional ultrasound imaging procedure

We utilized a fully featured commercial functional ultrasound acquisition system, Iconeus One (Iconeus, Paris, France) to acquire fUSI spinal cord images via a transducer probe inserted through laminar openings (Fig. 3.1 B). A 128 elements linear array transducer (Fig. 3.1 B, inner panel), with 15 MHz center frequency, 0.1 mm pitch (Iconeus, Paris, France) was used to generate fUSI images with spatial resolution of 100 µm × 100 µm in-plane, slice thickness of 400 μm, FOV of 12.8 mm (width) × 10 (depth) mm and maximum penetration depth of about 20 mm. The penetration depth is sufficient to image the dorsal portion of the spinal cord on a transverse orientation. The probe was fixed steadily throughout experiments with the FOV transverse and intersecting the spinal cord central canal (Fig. 3.2 A). To increase imaging signal-to-noise-ratio, we obtained each image from 200 compounded frames acquired at 500 Hz frame rate, using 11 tilted plane waves separated by 2° (i.e., from -10° to +10° increment by 2°). Images were acquired with a 5500 Hz pulse repetition frequency. Imaging sessions were performed using a real-time continuous acquisition of successive blocks of 400 ms (with 600 ms pause between pulses) of compounded plane wave imaging. The acoustic amplitudes and intensities of the fUSI sequence remained below the Food and Drug Administration limits for ultrasonic diagnostic imaging (FDA, 510k, Trace 3).

3.5.3 Epidural electrical SCS parameters and protocol

A standard-of-care stimulation protocol was administered consisting of 10 ON-OFF cycles, with each cycle containing 30 s ON period (stimulation ON) and 30 s OFF period (stimulation OFF). The protocol involved bipolar stimulation at the middle contacts (spanning T8-T9 interspace) (Fig. 3.1 B), utilizing 40 Hz burst frequency, 250 μs pulse width and 3.0 or 4.5 mA current amplitudes. Four patients received ESCS protocol consisting of 10 ON-OFF cycles of low (3.0 mA) current stimulation, while 2 patients received 10 ON-OFF ESCS cycles consisting of successive 5 ON-OFF stimulation cycles of low (3.0 mA) current amplitude followed by another 5 ON-OFF high (4.5 mA) current amplitude stimulation (Fig. 3.1 D). Additionally, we acquired fUSI spinal cord signal from one patient (P7) who received a non-invasive TSCS protocol, involving 8 cycles consisting of 4 cycles at 50 mA followed by 4 cycles at 100 mA.

3.5.4 Data preprocessing

The Iconeus One acquisition system utilized in this study generates pD intensity images pre-processed with built-in phase-correlation based sub-pixel motion registration [162] and singular-value-decomposition based clutter filtering algorithms [105]. These algorithms are used to separate tissue motion signal from blood signal to generate relative fUSI pD signal intensity images [163]. To address potential physiological and motion artifacts unique to human spinal cord imaging, we adopt rigid motion correction techniques [108] that have successfully been used in fUSI [28] and other neuroimaging studies [106,107,164]. This was combined with in-house developed breathing, high frequency smoothing filtering and image stabilization approaches. We employed a lowpass filter with normalized passband frequency of 0.04 Hz, with a stopband attenuation of 60 dB that compensates for delay introduced by the filter, to remove high-frequency fluctuations in the fUSI pD signals (see Fig. 3.S.2 for the pre- and post-filtered spinal cord pD standard deviation using only the reference periods – i.e., 6 s prior to stimulation onset).

3.5.5 Statistical parametric maps and event-related average waveforms

We leverage conventional statistical analysis in functional brain imaging to compute SPMs to visualize regional spinal cord blood volume (SCBV) changes that are caused by ESCS. We identify regions with statistically significant changes ($p < 0.05$) on the fUSI signal between stimulation OFF and stimulation ON trials. Note that we used only the last 6 s of the stimulation OFF trials – i.e., 6 s prior to onset of stimulation ON trials – to minimize the potential washout effect of the electrical stimulation. We selected 6 s because we found that it can take up to about 20 s for the hemodynamic signal to return to baseline activity after cessation of the stimulation (see Figs. 3.4 B and 3.4 C). The SPMs are derived based on the

Student's t-test (two side with false discovery rate [FDR] correction based on the number of pixels tested) for each pixel in the fUSI image. That is, each individual pixel derived its own p-value which indicates the level of significant ΔSCBV induced by ESCS. Finally, we generate ERA waveforms of the SCBV changes as a percentage change from the reference activity for selected ROIs. To assess the effects of potential washout of ESCS on the stimulation OFF trial periods, we also generated the SPMs utilizing the mean signal of the entire 30 s of stimulation OFF trials as well as baseline activity preceding onset of any ESCS.

3.5.6 Predict effects of ESCS on spinal cord hemodynamics response at a single trial level.

We utilize conventional data analysis and interpretable machine learning techniques to examine whether evoked hemodynamic changes captured in single trial fUSI spinal cord images can be used to discriminate between stimulation ON and stimulation OFF states. We perform off-line decoding on the fUSI spinal cord images with a strategy that consists of three parts: 1) align the SCBV image time series with the stimulation status, 2) select features, reduce dimensionality, and discriminate classes, 3) cross validate and evaluate performance (Fig. 3.7). The 2D fUSI signals are extracted from the 10 cycles of stimulation OFF-ON trials into separate time series matrices for each patient (x, y, t) – one for stimulation ON and the other for stimulation OFF. Each pD image is flattened to create a 1D vector and is attached to a class label that represents the status of the stimulation (class 0: stimulation OFF and class 1: stimulation ON). The 1D vectors from each class are placed into a 2-dimensional matrix with dimension n x m, where n is the number of pixels for the flattened pD images and m is the total acquisition time for each group. A subset from each group is then randomly separated into training (75%) and testing (25%) sets for cross-validation analysis. We use whole fUSI spinal cord images to perform the single-trial analysis. For dimensionality reduction and class separation, we employ classwise principal component analysis (cPCA) [141] and LDA [165] respectively. We chose cPCA because of the small imaging sample size, large sparsity, and feature dimensions. It has successfully been used to reduce data sparsity and dimensionality while maintaining enough components to retain over 90% variance in imaging data such as ours [141,166,167]. We integrate cPCA with LDA to assess whether the cPCA-transformed fUSI images can predict an impending stimulation OFF (class 0) or stimulation ON (class 1). Mathematically the transformed feature for each trial can be represented by $f = T_{LDA}\Phi_{CPCA}(d)$, where $d \in \mathbb{R}$ are the flattened images, Φ_{CPCA} is the piecewise linear cPCA transformation, and T_{LDA} is the LDA transformation. Φ_{CPCA} is physically related to space and thus can be viewed within the context of physiological meaning (Fig. 3.8 D). We subsequently use Bayes rule to calculate the posterior probabilities of each class given the observed feature space. Because cPCA is a piecewise function, this is done twice, once for each class, resulting in four posterior likelihoods: $P_{OFF}(OFF|f^*)$, $P_{OFF}(ON|f^*)$, $P_{ON}(OFF|f^*)$ and $P_{ON}(ON|f^*)$ where f^* represents the observation, OFF and ON represent the posterior probabilities in the cPCA subspaces created with training data from stimulation OFF and stimulation ON trials, respectively. Finally, we store the optimal principal component (PC) vectors and the corresponding discriminant hyperplane from the subspace with the highest posterior probability. We then use these findings to predict the state of the spinal cord (i.e., stimulation OFF vs. stimulation ON) in the testing set. That is, we compute f^* from fUSI imaging data for each trial in the testing set to predict the state of the spinal cord. To cross-validate and test the robustness of the classifier models, we perform 100 iterations of bootstrapping randomized selection of 75% of the stimulation ON and OFF fUSI images for training our decoding model. The randomized bootstrap selection approach was utilized to accommodate the relatively small data size. All the data pre- and post-processing analysis were performed in MATLAB

R2020b (Matworks, Natick, MA). All the machine learning functions were performed in MATLAB R2022b with no special toolboxes. We customized the classwise principal component analysis implementation by Nenadic et. al. [141] to suit our analysis needs and paired it with linear discriminant analysis.

3.5.7 Spatial resolution and power Doppler quantiles

To evaluate the effect of spatial resolution on the decoding accuracy on ESCS evoked spinal cord states, we use 1-20 s window of pD images to train the classifier while decreasing the resolution of the images. We resized the original 100 µm resolution images using a nearest neighbor interpolation approach to achieve images with spatial resolutions of 200 µm and 400 µm. We then used the downsized images to independently decode the spinal cord states. Additionally, we performed a one-sided Student t-test to compare the mean decoding accuracy of the 100 µm, 200 µm and 400 µm resolution fUS images. We selected the interval of peak accuracy (14:17 s test time instants within the 20 s training window) of the 100 µm resolution images to perform the quantification analysis.

Next, to evaluate the source of hemodynamic information content relevant for classifying ESCS ON and OFF states, we ranked ordered pixels by their mean pD intensity, which is derived from averaging 6 s of fUSI recordings prior to the first stimulation trial and segmented by deciles resulting in a spatial map of ranked deciles. Higher deciles correspond to higher pD intensity and hence higher blood flow in the spinal cord. The cut-off between 5 and 6 was chosen to divide the lower half deciles from the upper half deciles and to approximately discriminate small from large vessels. We accounted for potential non-normality by transforming the mean pD intensity signals into approximately normal distributions, using the (boxcox) function in Matlab 2020b. The pixels within each decile were unique and did not overlap with other deciles. Using pixels from each segmented decile, we performed cross-validated classification analysis, as described before, to evaluate the classification accuracy across deciles. Additionally, we performed a one-sided Two-Sample t-test to compare the mean decoding accuracy of decile-ranges 1-2, 3-5, 6-8 and 9-10, corresponding to the smallest, small-medium, medium-large, and largest-vessel groups imaged.

3.6 Supplementary materials

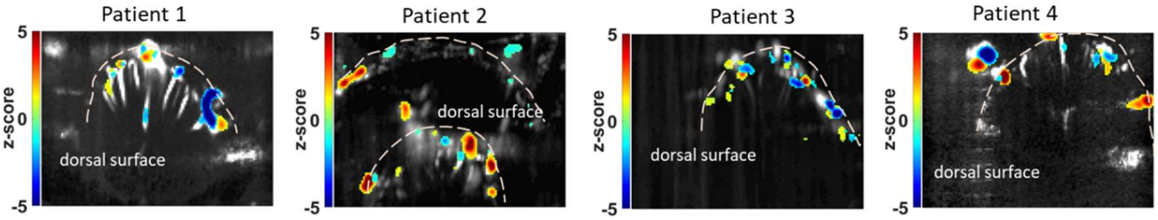

Figure 3.S.1 Statistical parametric maps without correcting for washout effects from the electrical stimulation. Statistical map shows localized areas with significantly higher SCBV during stimulation ON with respect to all 30 s of stimulation OFF reference activity (two-sided t-test of area under the curve, $p < 0.05$, false discovery rate [FDR] corrected for number of pixels in image). We do not correct for potential washout effect from the electrical stimulation – i.e., all 30 s of acquisition were used from the stimulation OFF trials.

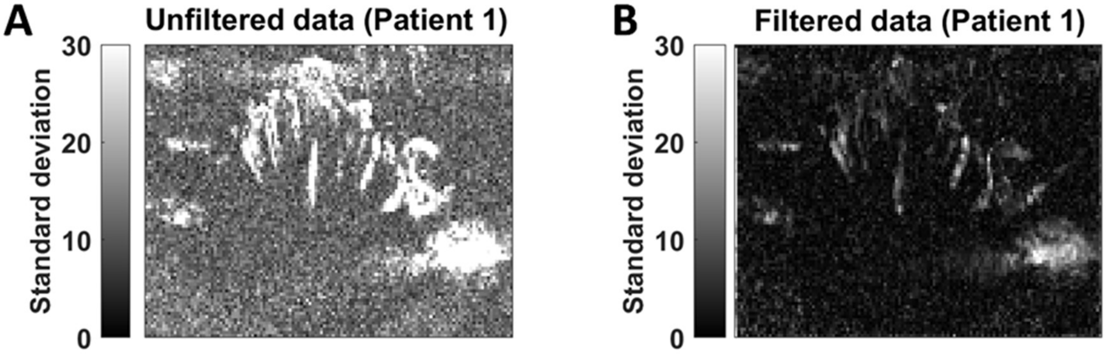

Figure 3.S.2 Variance of pD signal during baseline periods (i.e., 6 seconds prior to stimulation onset) in pre- and post-motion correction. A) Pixelwise standard deviation in unfiltered fUSI pD intensity signal during baseline periods (patient 1) B) Pixelwise standard deviation in filtered fUSI pD intensity signal during baseline periods (patient 1). Motion correction algorithms reduce the standard deviation of the power Doppler intensity signal during baseline, indicating that most of the motion artifacts are significantly removed from the fUSI image.

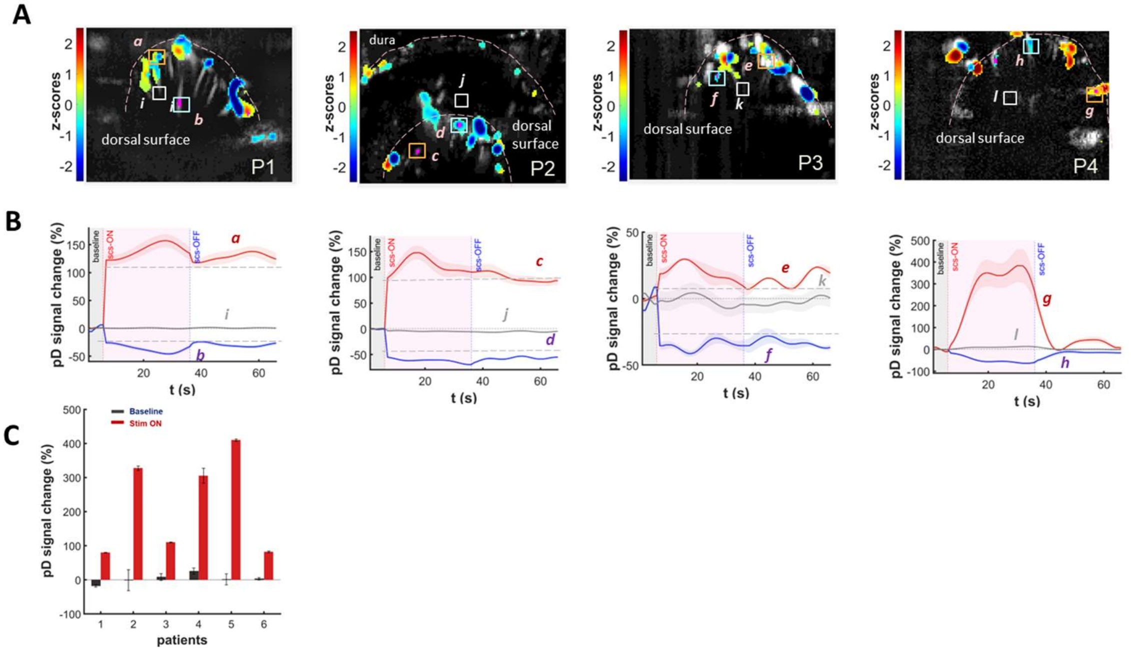

Figure 3.S.3 Statistical parametric map and event-related average waveforms. A) Statistical map shows localized areas with significantly higher or lower SCBV with respect to baseline – mean of 6 s signal activity before ESCS. SPMs are overlaid on grayscale baseline mean pD intensity images. B) ERA waveforms of selected ROIs [as indicated with boxes and letters in SPMs – panels A] that exhibit strong increased changes of blood perfusion (red curves – orange boxes) or that exhibit strong decrease change of blood perfusion (blue curves – cyan boxes), after turning on the stimulator. The ERA waveforms corresponding to control ROIs that do not show significant changes in blood perfusion (gray curves – white boxes) after the stimulator is turned on are also displayed. C) Baseline and trial-to-trial ERA waveforms.

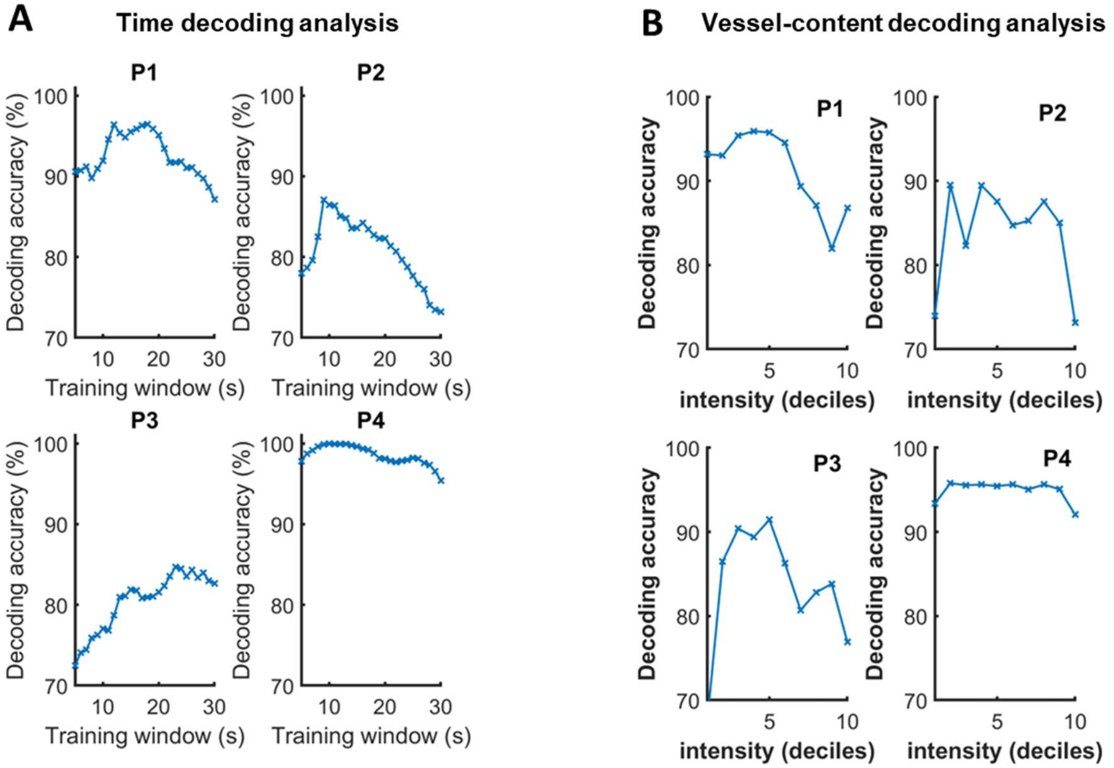

Figure 3.S.4 Patient decoding accuracy for time-data amount and vessel-content analysis. A) Data-amount analysis decoding accuracy for each patient (n=4) as a function of the amount of data used to train the classifier – i.e., time after the stimulation onset - training window. The accuracy increases with increasing data amount, peaks, and then decreases after various amounts of training window in all patients. B) Vessel-content analysis decoding accuracy (Stimulation ON vs. Stimulation OFF) as a function of deciles (pD intensity sub-divisions) for each patient (n=4). Decoding accuracy peaks around quantile 4 or 5 and then decreases in all patients. Deciles 4 and 5 mostly contain small to medium vasculatures within the spinal cord. The smaller vessels and primary unit vasculature (i.e., deciles 1 and 10, respectively) appear to carry less information about the effect of ESCS on spinal cord blood flow.

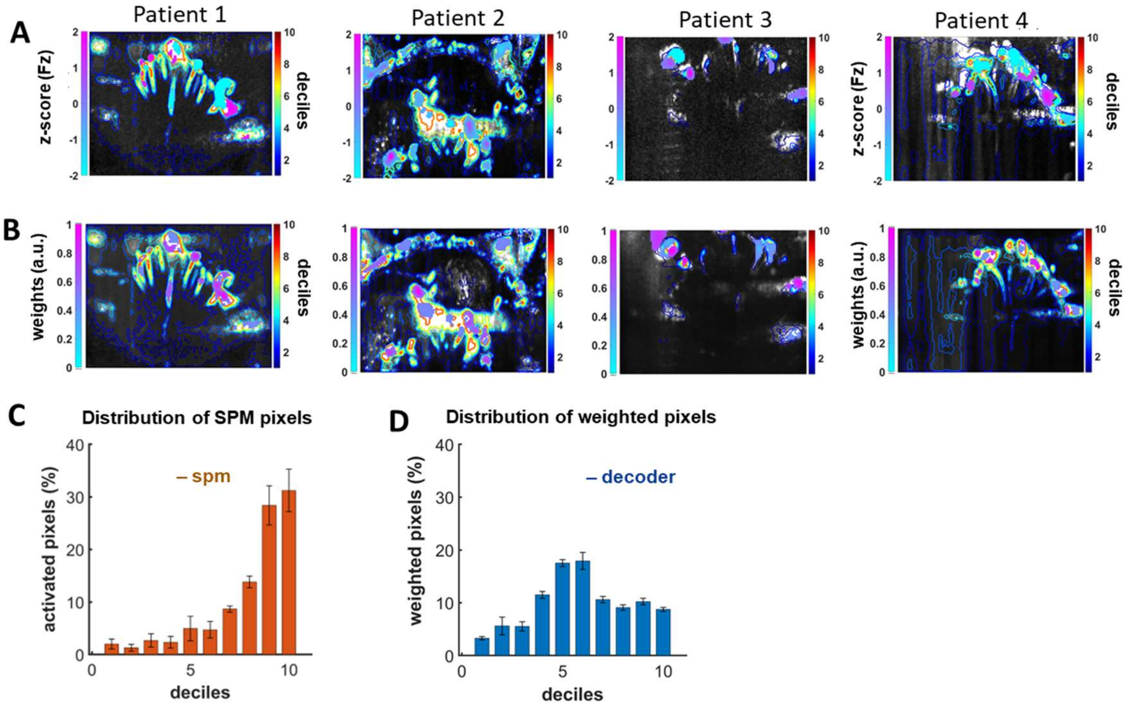

Figure 3.S.5 Distribution of SPM activated and decoder weighted pixels. A) Statistical map shows localized areas with significantly higher or lower SCBV with respect to reference activity during stimulation OFF. SPMs are overlaid on grayscale baseline mean pD intensity images and contours dividing the spinal cord image into deciles of mean pD intensity. B) Decoder weighting maps show pixels in the spinal cord image that are heavily weighted [-1, +1] with respect to relevance in discriminating between stimulation ON and OFF classes. Pixels with values close to +1 or -1 indicate high relevance components, while pixels with values close to 0 are less important and whose fluctuations are likely due to noise. The weighting maps are overlaid on grayscale baseline mean pD intensity images and contours dividing the spinal cord image into deciles of mean pD intensity. C) Distribution of the SPM activated pixels as a function of deciles (pD signal intensity sub-divisions) averaged across patients (n=4). A large proportion of the activated pixels in the SPMs are found in deciles 9 and 10 – corresponding to the larger vessels. D) Distribution of the decoder weighted pixels as a function of deciles (pD signal intensity sub-divisions) averaged across patients (n=4). The greatest proportions of the weighted pixels that are most relevant for decoding are found in deciles 5 and 6 – corresponding to small-medium vessels.

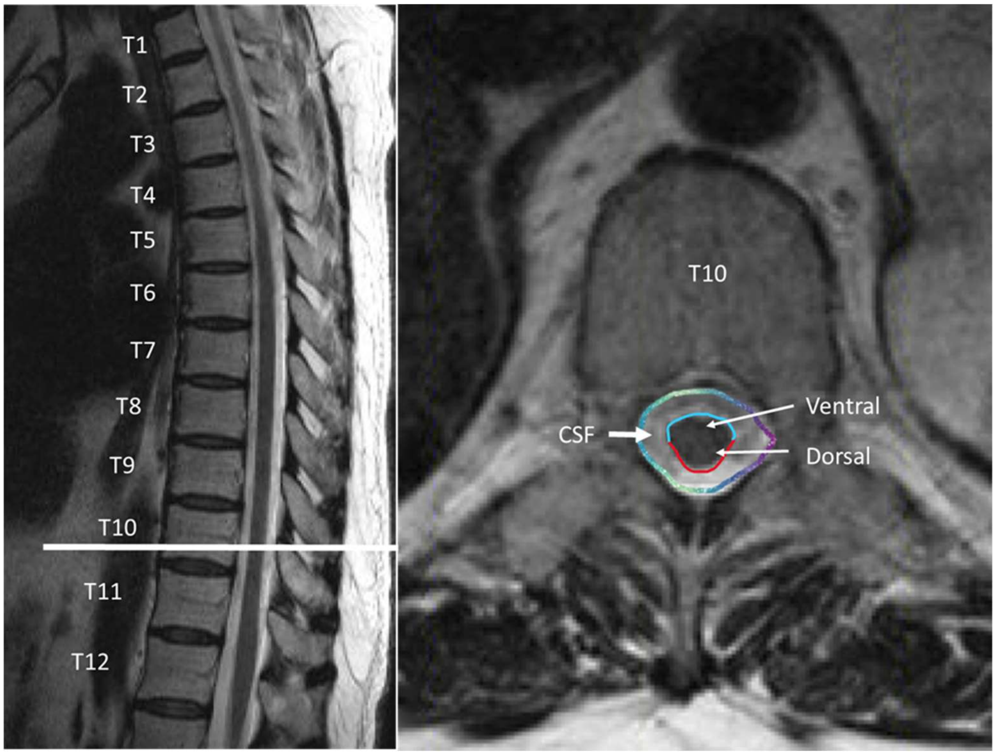

Figure 3.S.6 Sagittal (left) and axial (right) image of the spinal cord in patient P1. All patients underwent a preoperative MRI to ensure that there was no thoracic spinal cord stenosis that would prevent the implantation of the paddle electrode. The axial image mirrors that of the fUSI image. CSF: Cerebrospinal fluid, Ventral: Ventral horn, Dorsal: Dorsal horn.

Chapter 4

Unravelling Encoding of Urodynamics in the Human Spinal Cord using Functional Ultrasound Imaging

Reprinted with permission from Agyeman K, et. al.

4.1 Abstract

While strong evidence from preclinical work reveals the presence of regulatory neural-network-circuits that are responsible for vital motor, sensory and autonomic functions, its demonstration in humans has been challenging. The physiological location and small cross-section make the spinal cord susceptible to artifacts and an unfavorable target for traditional neuroimaging techniques. Functional ultrasound imaging is an emerging neuroimaging modality that provides high sensitivity, coverage, and spatiotemporal resolution. fUSI was recently extended to image the spinal cord in animals and humans. While these studies are significant, their primary focus is predominantly on the neuro-activation of the spinal cord in response to external sensory stimuli. Here, we combined fUSI with a controlled-urodynamics filling and emptying process to characterize the hemodynamic response of the human spinal cord to an end-organ physiological process. We characterize the spatial and temporal

responses to micturition using simultaneous spinal cord pD signal acquired through a partial lamina opening and intravesical bladder pressure recordings from six patients. We identified spinal cord regions in which the pD signal is strongly correlated with the bladder pressure. We extend these results to decode the bladder pressure dynamics with high accuracy solely using fUSI spinal cord pD signal. Overall, our study provides the first in-human application of fUSI to characterize hemodynamic responses of the spinal cord during urodynamics and offers direct evidence of the existence of spinal cord networks that control micturition. The high accuracy for decoding the state of the bladder based on the pD signal provides proof-of-concept that fUSI is an essential component for investigating function and building spinal cord machine interface for patients with urinary dysfunction.

4.2 Introduction

The spinal cord has been frequently neglected in the study of neural function. As a result, its anatomy and physiology are not as well understood as those of the brain. Yet, it represents the first evolutionary step in central nervous system development and houses the neural circuitry that controls and modulates some of the most important functions of life [109] . Neural networks capable of producing autonomous central commands – usually stereotyped and rhythmic motor behaviors – are presented throughout the rostral and the caudal parts of the spinal cord [168]. Actions such as chewing, swallowing, and breathing are thought to be partially produced by these networks in the rostral cord [169]. Similarly, autonomic functions such as urination and defecation are under control of neural networks located in the spinal cord [170].

Although evidence for the existence of neural network circuits that control and regulate certain body processes is strong, its demonstration in humans has been challenging to achieve. The bony, facial enclosure and small cross-section dimensions (approximately 12 mm in diameter) of the spinal cord combined with susceptibility artifacts due to local magnetic field inhomogeneities generated by interfaces between surrounding bones, ligaments, soft tissues, and cerebrospinal fluid make the spinal cord an unfavorable target for traditional neuroimaging techniques, such as functional magnetic resonance imaging [130–132,171]. As a result, the bulk of our understanding of spinal cord function comes from animal and lesioning studies [172]. There is little direct evidence for function-specific spinal cord activity in humans. fMRI, which has shed so much light on brain functions in humans, with regards to the spinal cord is only minimally developed and generally restricted to the cervical cord [171]. Given this context, there is a clear and distinct need for developing neuro-technologies that make the functional study of the human spinal cord more accessible.

Functional ultrasound imaging is an emerging neuroimaging technology that represents a new platform with high sensitivity, spatial coverage, and spatiotemporal resolution, enabling a range of new pre-clinical and clinical applications [1,3,20,22,28,30,32,173–175]. It was originally used for brain neuroimaging in small animals (i.e., rodents) [1]. Based on power Doppler imaging, fUSI measures changes in cerebral blood volume (CBV) by detecting backscattered echoes from red blood cells moving within its field of view [2,23]. While fUSI is a hemodynamic technique, its superior spatiotemporal performance (i.e., 100 μm and up to 10 ms) and sensitivity (~ 1 mm/s velocity of blood flow) offer substantially closer connection to the underlying neuronal signal than achievable with other hemodynamic methods such as fMRI. It is minimally invasive and requires trepanation in large organisms to enable the penetration of the ultrasound waves, as the skull attenuates the acoustic wave. fUSI does not penetrate well into the brain, but instead the ultrasound probe sits outside the dura mater. The fUSI scanner is like any clinical ultrasound machine, making the unit freely mobile between different settings and negates the need for extensive infrastructure inherent to fMRI.

Recently, fUSI was extended to study the spinal cord responses to electrical and mechanical stimulations in small animals and human patients [33,136–138]. Despite the significant contribution of these studies in understanding how spinal cord reacts to external sensory stimulations, none of them have demonstrated spinal cord circuits associated with physiological functions (i.e., body processes) in humans. In the current study, we utilize fUSI to study the hemodynamic response of the spinal cord during filling and emptying of the bladder in patients, who undergo general anesthesia and spinal cord surgery for chronic low back pain treatment. By combining fUSI recordings from the spinal cord with intravesical bladder pressure recordings, we identified spinal cord regions in which the hemodynamic signal is strongly correlated with the bladder pressure. Overall, our study provides the first in-human application of fUSI to characterize the hemodynamic response of the spinal cord during controlled-urodynamic bladder filling and emptying, opening avenues to better understand the mechanisms of control that the spinal cord exerts over micturition.

4.3 Results

To investigate how the human spinal cord hemodynamics respond to bladder filling and emptying process, we acquired fUSI images of the spinal cord from six (6) chronic low back pain patients, who underwent standard-of-care implantation of an epidural spinal cord stimulation device under general anesthesia (Fig. 4.1 A). Note that the urodynamic experiment was performed before ESCS implantation. A miniaturized 15.6-MHz, 128-channel, linear ultrasound transducer array was inserted through a partial laminar opening (Fig. 4.1 B) onto the dura at the level of the 10th thoracic vertebra (T10) with a transverse field of view (Fig. 4.1 D). We utilized a protocol that consisted of 26 min of continuous fUSI signal acquisition, including 5 min of baseline activity, followed by 2 bladder filling cycles and 1 emptying cycle, interspersed by 2 hold periods (about 1 min each) (Fig. 4.1 C). The bladder was filled and emptied, accompanied by continuous intravesical bladder pressure recordings using a Laborie Goby urodynamics system. The same protocol was employed for all patients. Fig. 4.1 E depicts the changes of the bladder pressure during filling and emptying for 4 (out of the 6) patients – we were unable to acquire bladder pressure signals from patients 2 and 3 due to technical challenges.

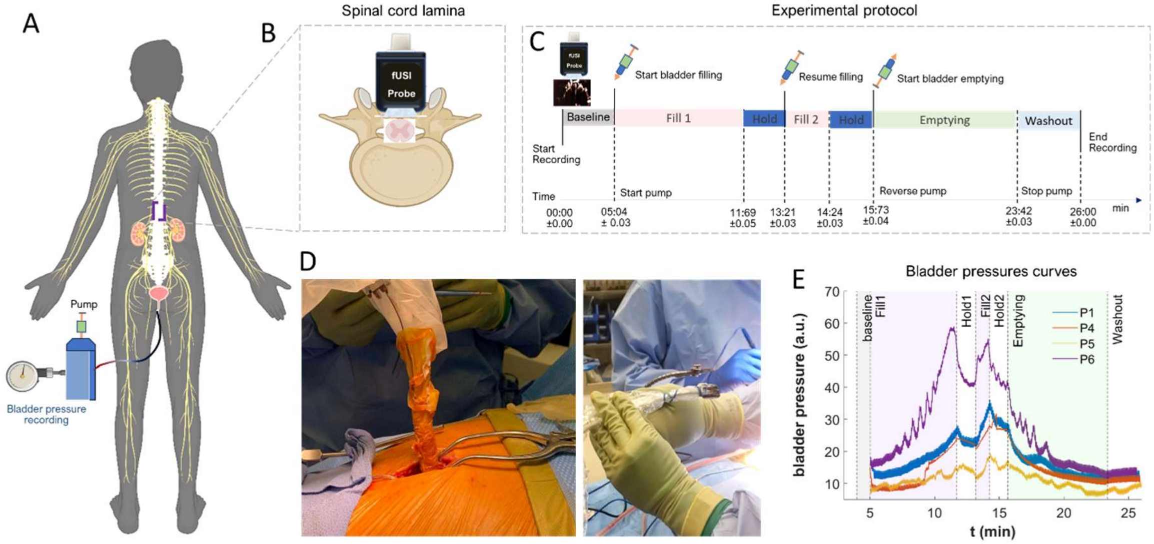

Figure 4.1 Experimental setup and fUSI acquisition protocol. A) A graphical representation of the human urodynamic model developed to study how the spinal cord activity is correlated with the bladder pressure. B) Schematic representation of the spinal cord fUSI acquisition through a laminar window. C) The experimental protocol for controlled-urodynamic filling and emptying of the bladder. D) Patients undergo a T10 partial laminectomy for standard-of-care implantation of an epidural spinal cord stimulator (ESCS) under general anesthesia. (E) Bladder pressure recordings across time during filling and emptying the bladder for the 4 (out of 6) patients. The bladder pressure signal was not acquired for 2 patients due to technical challenges.

4.3.1 Hemodynamic responses induced by bladder filling and emptying.

The fUSI signal acquisition from the spinal cord produced power Doppler-based functional ultrasound images (Fig. 4.2). We used the mean spinal cord pD signal (1 min just before filling onset) to capture the anatomical vascularization of the human spinal cord in all patients, with the dorsal surface indicated by the white discontinuous lines (Fig. 4.2 B-G). The pD images have spatial resolutions of 100 µm × 100 µm in-plane, plane thickness of about 400 µm, and a large field of view (FOV) 12.8 mm × 10 mm. The FOV captures the dorsal and portions of the ventral cross-section of the spinal cord – approximately indicated by the light-green rectangular overlay in Fig. 4.2 A.

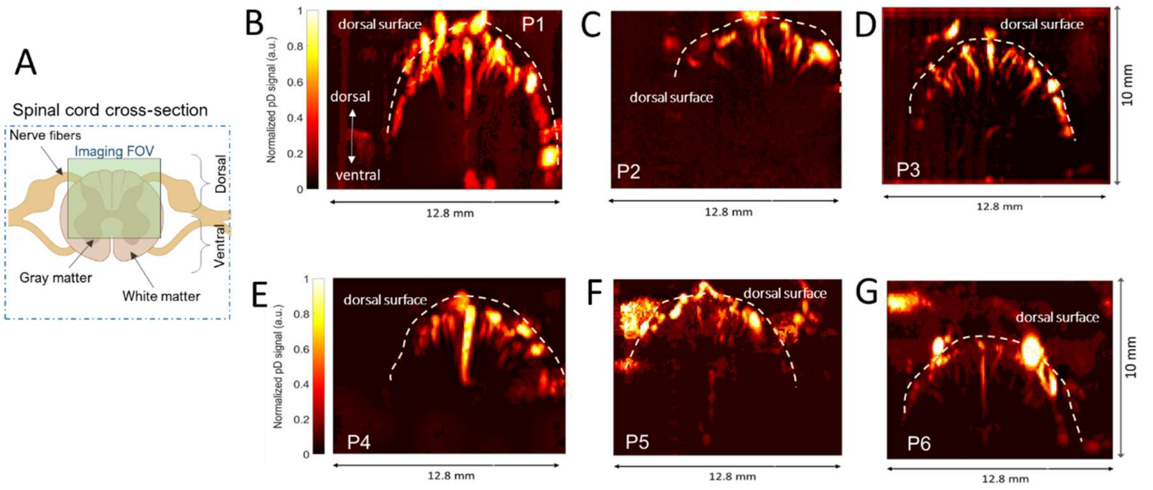

Figure 4.2 Functional ultrasound imaging of the spinal cord in a transverse plane. A) Cross section of spinal cord anatomy. The green area illustrates approximately the field of view of fUSI acquisition. (B-G) Power Doppler-based vascular maps showing the transverse section of the spinal cord of the six patients.

4.3.2 Effects of controlled urodynamics on spinal cord hemodynamics.

To assess how controlled-urodynamics in an end-organ evokes spatial and temporal changes in human spinal cord hemodynamics during filling and emptying of the bladder, we performed a dynamic statistical parametric map analysis (dSPM). The dSPMs are computed based on two-sided Student's t-test with false discovery rate correction (FDR) to identify regions recorded within the spinal cord that are strongly affected by filling and emptying of the bladder across time compared to baseline activity. To do so, we compare the mean fUSI %pD signal change in each pixel within a 20 s sliding window to the baseline activity signal at 5 s steps. We found specific regions within the spinal cords that are strongly activated with increase (red) and decrease (blue) in SCBV during filling and emptying of the bladder (see S-vid. 4.1 in supplementary materials for a movie of activation in the spinal cord at each sliding widow step. Also given is an animation of how the dSPMs are derived).

4.3.3 Correlation of fUSI spinal cord hemodynamic responses to bladder pressure signal

To characterize the spinal cord hemodynamic response during filling and emptying of the bladder, we compute the spinal cord blood volume changes (ΔSCBV) – i.e., % pD signal changes – relative to the baseline activity (i.e., average fUSI activity 1 min prior to the start of filling the bladder). The goal is to identify regions within the spinal cord that are correlated with bladder pressure. To do so, we compute an activation map for each patient, in which the bladder pressure measurement was available, by performing a Pearson's correlation analysis between the bladder pressure changes and ΔSCBV for each pixel in the recorded area. The activation maps reveal spinal cord regions that are positively (reddish areas, $r > 0.35$, $p < 0.01$)

and negatively (blueish areas, $r <- 0.35$, $p < 0.01$) correlated with bladder pressure during filling and emptying of the bladder (Fig. 4.3 A-D).

To assess the temporal pattern of activation of the bladder pressure-related regions, we compute the average ΔSCBV over the pixels of the positive and negative correlates to the bladder pressure, across time and patients. Since the magnitude of the hemodynamic response changes varies between patients, we normalized the ΔSCBV between [-1, 1]. Similarly, we normalized the bladder pressure between [0, 1] to account for the different magnitudes of the pressure curves across patients. The results presented in Fig. 4.3 E showed that bladder filling and emptying causes strong neuro-activation in the spinal cord. The positively correlated regions with the bladder pressure signal (i.e., red regions) exhibit a gradual increase in ΔSCBV during bladder filling with a subsequent gradual decrease in ΔSCBV during bladder emptying. Conversely, the negatively correlated regions with bladder pressure (i.e., blue regions) exhibit the opposite behavior – i.e., gradual decrease followed by increase of ΔSCBV during filling and emptying of the bladder, respectively. The gray curve depicts the average normalized bladder pressure changes across patients. The shaded regions around the bladder pressure and the ΔSCBV curves represent the standard error derived from averaging across patients. The correlation between the bladder pressure and ΔSCBV is 0.84 ± 0.023 (Mean ± SE) for the positively (reddish) and -0.78 ± 0.045 for the negatively (blueish) bladder pressure-related spinal cord regions across patients (Fig. 4.3 F, brown bars).

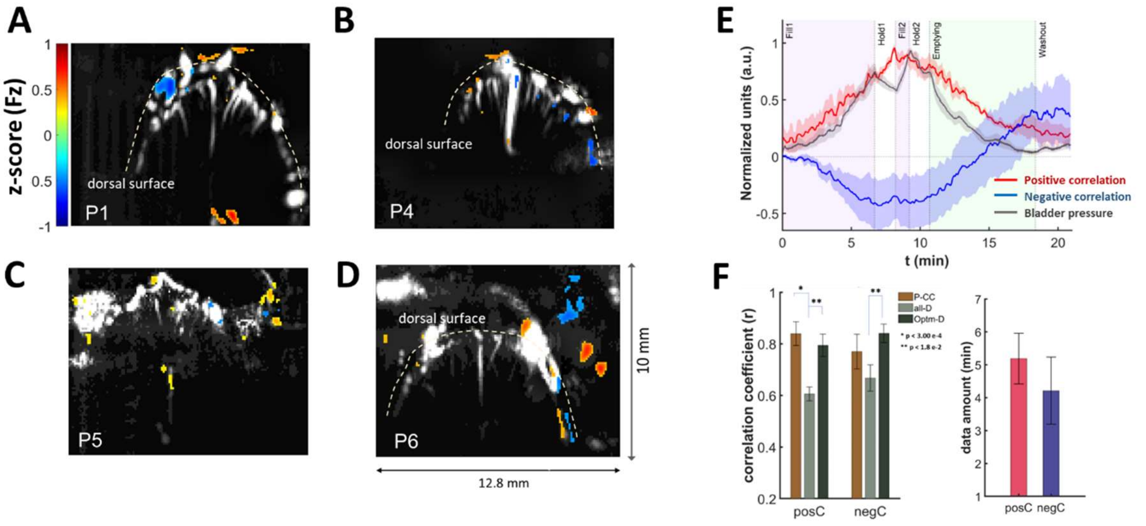

Figure 4.3 Activation maps of the correlation between ΔSCBV and bladder pressure during filling and emptying of the bladder. A-D) Activation maps that illustrate spinal cord regions that are positively (reddish) and negatively (blueish) correlated with the bladder pressure during filling and emptying of the bladder. E) Average normalized ΔSCBV (i.e., %pD signal change) of spinal cord regions that are positively (red curve) and negatively (blue curve) correlated with the bladder pressure across patients. The gray curve depicts the normalized changes of the bladder pressure during the urodynamic experiment. F) Left panel: Correlation coefficient values between the average ΔSCBV of bladder-pressure related regions and bladder pressure across the 4 patients whose bladder pressure was recorded. P-CC: Bladder-pressure related regions are extracted from the activation maps, all-D: Bladder-pressure related regions are extracted from the cPCA+SVM algorithm using all recorded fUSI images. Optm-D: Bladder-pressure related regions are extracted from the cPCA+SVM algorithm using the optimum sub-set of recorded fUSI images. Right Panel: The average optimum amount of fUSI data in the cPCA+SVM algorithm that produces the best correlation between ΔSCBV and the bladder pressure, across the 4 patients (P1, P4, P5 and P6) whose bladder pressure was recorded. posC and negC refer to pixels in which ΔSCBV is positively and negatively correlated with the bladder pressure.

4.3.4 Decoding bladder pressure dynamics from SCBV signal

The bladder pressure signal was not recorded in patients P2 and P3 due to technical challenges. Naturally, that excludes the data of these patients from the preceding bladder-pressure and ΔSCBV correlation analysis – a downside which decreases our sample size and power. We investigated whether we could detect spinal cord regions that encode the bladder pressure dynamics without directly monitoring the bladder pressure. To do so, we developed a machine learning algorithm to identify bladder pressure-related regions in the recorded image (Fig. 4.4). We first assessed the performance of the algorithm to the patients, whose bladder pressure was recorded during the experiment, so that we directly compare the results with the ones achieved by the Pearson's correlation analysis and the activation maps. After collecting the fUSI data from the human spinal cord (Fig. 4.4 A), we implemented a class-wise principal component analysis (cPCA) to reduce dimensionality of the spinal cord imaging data (91 ×128 pixels) and extracted effective discriminant features to dissociate between bladder filling (class:0, c0) and emptying (class:1, c1) classes (Fig. 4.4 B). The entire fUSI spinal cord time series data acquired during filling and emptying periods were utilized (the hold time periods were excluded). The analysis was performed separately for each patient in which the bladder pressure was successfully recorded (N=4). cPCA has been used to reduce sparsity and dimensionality while maintaining enough components to retain over 95% variance in the data (see Materials and Methods section for more details). It is ideally suited for discrimination problems with large dimensions and small sample size including natural and biomedical images [142,167] . We paired cPCA with a class-discriminant support vector machine (SVM) classifier to determine the best decision boundary that separates the two classes - i.e., filling vs. emptying (Fig. 4.4 C). A subset from each class is then separated into training (80%) and testing (20%) sets for cross-validation analysis. This approach results in a 1D low-dimension subspace that represents a feature extraction mapping from the 2D spinal cord image space. The subspace identifies pixels in the spinal cord fUSI images that encode differences between the filling (c0) and emptying (c1) classes, when projected back to the image space. Each pixel is assigned a relative weight of relevance normalized between [-1 1] – pixels with values close to +1 or -1 imply important components, while pixels with values close to 0 are less important with their fluctuations likely due to noise with respect to each class (Fig. 4.4 C). Physically, the weighted regions can be interpreted as spinal cord regions with ΔSCBV that encode differences between the filling and emptying classes. The positive and negative weights indicate that ΔSCBV contributes positively and negatively to the variation captured by the principal component, respectively. Hence, ΔSCBV of pixels that have positive and negative relative weights are positively and negatively correlated with the bladder pressure. The heat-map in Fig. 4.4 D (left column) represents a typical example of the decoding analysis that identifies the most relevant spinal cord image pixels associated with filling and emptying the bladder for patient 1 – the most positive (reddish) and negative (bluish) relative weighted pixels overlayed on a grayscale mean fUSI spinal cord vascular map. We found that cPCA+SVM algorithm identifies spinal cord regions where ΔSCBV is correlated with the bladder pressure with r = 0.58 ± 0.09, (mean ± SE) for the positive weights and r = -0.59 ± 0.08 for the negative weights across the 4 patients (Fig. 4.3 F left panel, light gray bars). These results showed that the cPCA+SVM algorithm can identify pixels where ΔSCBV significantly correlates with the bladder pressure, although the strength of this correlation is lower than what is achieved through the original Pearson's correlation analysis and the activation maps (Fig. 4.3).

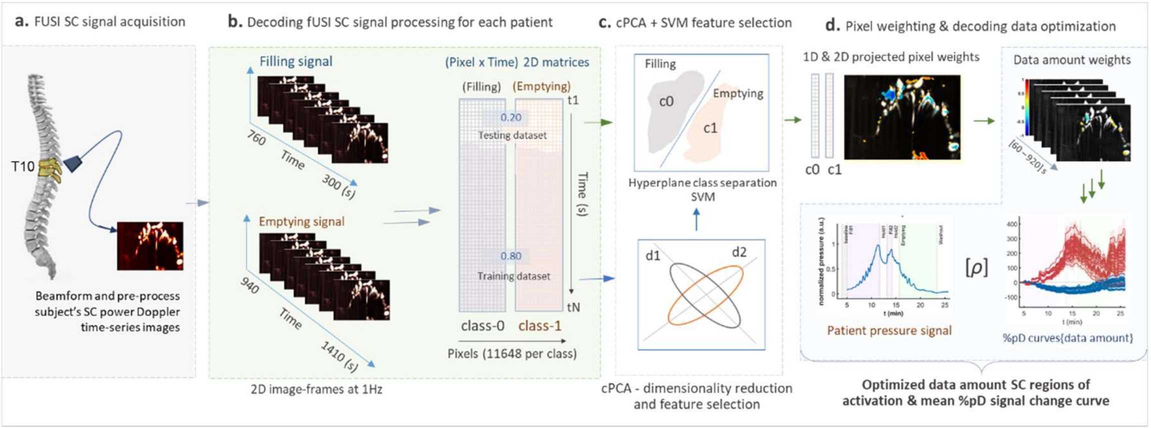

Figure 4.4 Flowchart of the cPCA+SVM algorithm developed to detect bladder pressure-related spinal cord regions. A) fUSI data during filling (class 0, c0) and emptying (class 1, c1) the bladder were recorded from the T10 and B) separated in training images and testing images based on the cross-validation technique used – 80% training data and 20% testing data. C) cPCA was paired with SVM to classify the state of the bladder (i.e., class 0 vs. class 1) using only the recorded pD signal from the spinal cord. D) This approach results in a 1-dimensional subspace the represents a feature extraction mapping from the 2D spinal cord image space. The subspace identifies pixels that are assigned with a relative weight between [-1, 1] and encodes the differences between the two classes – the higher the weight, the more significant the contribution of this pixel to the class separation. Highlighted panel shows the process for identifying the optimum amount of fUSI data that generate the best correlate between ΔSCBV and bladder pressure.

Next, we used the cPCA+SVM algorithm to identify bladder pressure-related spinal cord regions in the two patients (i.e., P2 and P3) whose bladder pressure was not recorded due to technical challenges (Fig. 4.5 A-C). The hemodynamic changes of the bladder pressure-related regions exhibit the same temporal pattern with the bladder pressure-related regions identified in the 4 other patients (Fig. 4.5 C). These results show the capability of cPCA+SVM to identify spinal cord regions that encode the bladder pressure dynamics, even when information about the bladder pressure is not available.

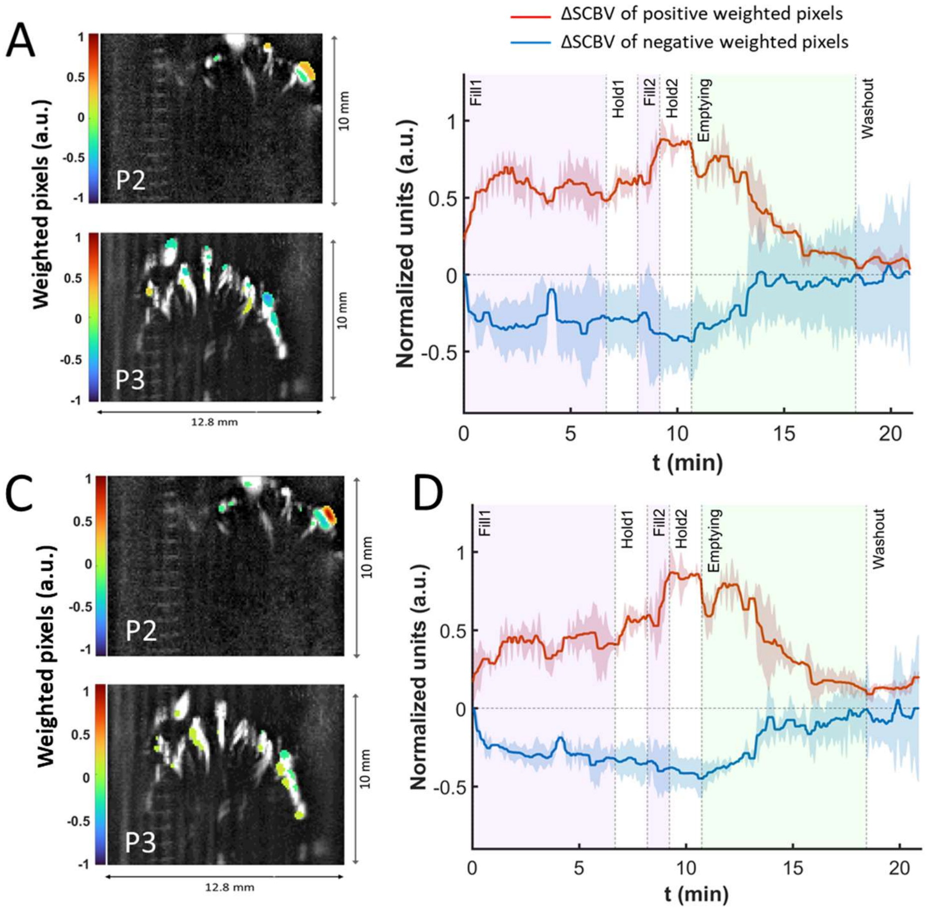

Figure 4.5 Bladder pressure-related spinal cord regions identified using cPCA+SVM in 2 patients whose bladder pressure recordings are not available. A-B) Weighted map of patients P2 and P3 extracted by the cPCA+SVM algorithm using all fUSI recorded data. C) Average normalized ΔSCBV (i.e., %pD signal change) of spinal cord regions with positive weights (red curve) and negative weights (blue curve) as extracted by the cPCA+SVM algorithm using all fUSI data, across the 2 patients. D-E) Weighted map of patients P2 and P3 extracted by the cPCA+SVM algorithm using the optimum amount of fUSI data. F) Similar to panel C but using the optimum amount of fUSI data.

4.3.5 Optimum data amount for decoding bladder pressure dynamics

Thus far, we have demonstrated that cPCA+SVM algorithm can identify bladder pressure-related spinal cord regions. However, the strength of the correlation between ΔSCBV and bladder pressure is lower than what is achieved through the original Pearson's correlation analysis. An interesting question is whether we can improve the cPCA+SVM performance using a subset of fUSI data – instead of the entire data set – to train the classifier. The goal is to determine the optimum amount of data needed to train the classifier to detect the spinal cord regions that produce the best performance – i.e., the highest correlation between ΔSCBV of the bladder-related spinal cord regions (i.e., as extracted by the cPCA+SVM algorithm) and the bladder pressure dynamics. To do so, we begin with the last 60 s period of fUSI data acquired during bladder filling for class c1, and the first 60 s period of fUSI data acquired during bladder emptying for class c0. We employed 10 s data increment for each class – i.e., positive increment for class c0, and negative increment for class c1 – to derive a cumulative set of fUSI images that is used to train and evaluate the performance of the algorithm. We utilized similar cPCA+SVM decoding steps as outlined above with increasing data amounts. Each subset of data produces weighted relevant pixels that best discriminate between the two classes. A characteristic example of the weighted relevant pixels with the corresponding average ΔSCBV time course curves is illustrated in Fig. 4.4 D (right column), in which the red and blue curves represent the average ΔSCBVs in areas with positive and negative weights, respectively. We then determine the optimum amount of fUSI data for each patient, in which the ΔSCBV of the weighted pixels exhibit the highest Pearson's correlation coefficient with the bladder pressure (Fig. 4.4 D highlighted area). The results show that the cPCA+SVM algorithm achieves better performance – i.e., higher correlation between ΔSCBV and bladder pressure – when a subset of the total amount of recorded fUSI data is used (Fig. 4.3 F dark gray bars). Specifically, we found that the correlation is significantly ($p > 0.01$) improved to $r = 0.80 \pm 0.03$ for the positive weights and to $r = -0.84 \pm 0.04$ for the negative weights, when 5.19 ± 0.46 s and 4.21 ± 1.3 s amount of data are utilized, respectively (Fig. 4.3 F, left panel, dark gray bars). Fig. 4.6 illustrates the positive and negative weighted relevant pixels derived by the cPCA+SVM algorithm using the optimum amount of data ($n = 4$) (Fig. 4.6

C). The average ΔSCBV curves across the 4 patients, derived from the positive (red) and negative (blue) weighted relevant pixels of the cPCA+SVM algorithm with optimum amount of data are presented in Fig. 4.6 D. Note that the cPCA+SVM algorithm achieves about the same performance with the Pearson's correlation analysis, in terms of the correlation between the average ΔSCBV and bladder pressure – i.e., no significant differences between the two techniques (see Fig. 4.3 F left panel). However, the variability of the average ΔSCBV for the negative correlated regions (blueish) is significantly reduced in the cPCA+SVM algorithm (Fig. 4.6 E) compared to the Pearson's correlation analysis (Fig. 4.3 E).

Next, we evaluated the cPCA+SVM algorithm using a subset of fUSI images in the two patients (n=2) whose bladder pressure signals were not recorded due to technical challenges. Since we did not have information about their bladder pressure to compute the optimum amount of fUSI data, we used the average optimum amount of fUSI data from the other 4 patients whose bladder pressure information was available. Figs. 4.5 D and 4.5 E show the bladder-related spinal cord regions identified from the cPCA+SVM algorithm with the optimum amount of data for patients P2 and P3, respectively. The average temporal course of ΔSCBV during filling and emptying the bladder for areas assigned with positive and negative relative weights are presented in Fig. 4.6 F. Consistent with the 4 previous patients, the results showed that the variability of ΔSCBV reduces for the negative relevant weighted pixels when using a subset of the recorded fUSI data.

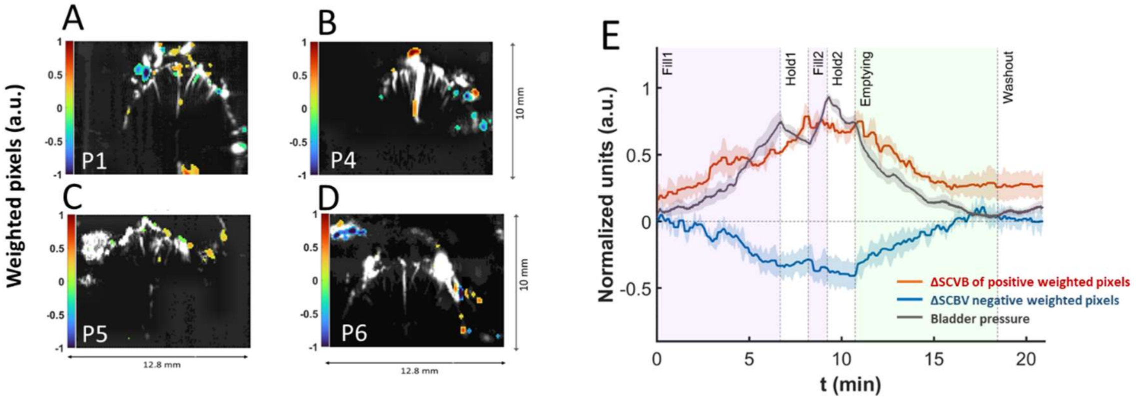

Figure 4.6 Bladder pressure-related spinal cord regions identified using cPCA+SVM in 4 patients with bladder pressure recordings. A-D) Weighted maps as extracted by the cPCA+SVM algorithm with optimum amount of fUSI data for the 4 patients (P1, P4, P5 and P6). E) Average normalized ΔSCBV (i.e., %pD signal change) of spinal cord regions with positive weights (red curve) and negative weights (blue curve) of relevance as extracted by the cPCA+SVM algorithm using the optimum amount of fUSI data, across the 4 patients.

4.4 Discussion

4.4.1 General

fUSI represents an emerging neuroimaging technology that utilizes ultrasound to monitor CBV changes as an indirect readout of neuronal activity with high spatiotemporal resolution, penetration depth and sensitivity to slow blood flow motion. Originally developed for brain neuroimaging, fUSI has been recently expanded to study spinal neurovascular responses in small animals and [33,136–138] and human patients [176]. Although these studies provide significant insights to better understand the physiology of the spinal cord in sensory integrations, they are limited to artificial external stimulations illustrating the capability of fUSI to detect binary discrete states of spinal cord activity – i.e., stimulation on vs. stimulation off). In the current study, we take the next major leap in fUSI spinal cord research by recording functional activity of the human spinal cord during controlled-urodynamics bladder filling and emptying. We show that fUSI can detect spinal cord regions in which the hemodynamic signal is highly correlated with the bladder pressure. We also introduced a machine learning algorithm that can detect bladder pressure-related spinal cord regions, even when information about the bladder pressure is not available. Our success to characterize and correlate spinal cord hemodynamics to micturition events holds promise to further understand functional and dysfunctional anatomy associated with lower urinary tract physiology.

4.4.2 New avenues for improving neuromodulation treatments for urinary incontinence.

Disease or injuries of the nervous system can cause re-emergence of involuntary urination, leading to urinary incontinence (UI). Especially, patients with spinal cord injury (SCI) frequently develop a wide gamut of urologic problems including UI and inability to empty the bladder volitionally and completely [177]. Epidural spinal cord stimulation (ESCS) of the lumbosacral spinal cord has shown potential to activate neural networks associated with bladder function in rodents with SCI [178,179]. Additionally, clinical trials have shown that transcutaneous electrical spinal cord stimulation (TSCS) – i.e., a non-invasive neuromodulation therapy that stimulates the spinal cord from the surface of the skin – can reengage the spinal circuits involved in bladder control and normalize bladder and urethral sphincter function in patients with SCI [180,181]. Although neuromodulation therapies offer a great promise for correcting or improving bladder control in patients with UI, their mechanism of action (MOA) remains elusive. This is mainly due to the lack of a monitoring modality that can characterize the effects of neuromodulation on spinal cord activity. Combining fUSI with neuromodulation of spinal networks has considerable potential in gaining a better understanding of the MOA of neuromodulation in improving bladder control in patients with UI. Additionally, fine tuning stimulation wave properties, such as amplitude, frequency, and shape will facilitate objective identification of the efficacy of neuromodulation using fUSI.

Challenges and limitations

4.4.3 Invasiveness nature of fUSI

While fUSI is a novel technology that enables monitoring of brain and spinal cord activity, the skull and the lamina bone attenuate and aberrate acoustic waves at high frequencies substantially reducing signal sensitivity. For this reason, most of the fUSI applications are minimally invasive – with few exceptions such as in young mice (8-12 weeks old with thin skull) [159] and in pediatric fontanelle-imaging [31,32]. Surgical procedures to produce a craniotomy17 or thinned-skull window [26] in brain research and laminectomy [137,176] in spinal cord research is required to harness the host of fUSI benefits. Hence, using fUSI to record spinal cord activity in awake adults is challenging and has yet to be proven. However, recent studies in brain research provide evidence that non-invasive fUSI is capable either through a permanent "acoustic window" installed as part of a skull replacement procedure following a decompressive hemicraniectomy (partial skull removal) [182] or by intravenously injecting microbubbles-contrast agents for enhancing the fUSI signal [160,183]. Although these approaches have not yet been tested in spinal cord research, the promise of fully noninvasive fUSI in spinal cord is imminent.

4.4.5 Clinical limitations

It is important to acknowledge that we recorded activity in the thoracic cord (T10), although the main control mechanism of the bladder is thought to reside in the sacral cord between S2-S4, with the major portion at S3 [168], [184]. This is a typical limitation in clinical studies that often we are not able to record activity directly from the desirable locations. In our study, we image the spinal cord during controlled-urodynamic micturition in patients who undergo ESCS surgery for chronic low back pain treatment. The midline of the spinal cord at T10 is the preferred location for this neuromodulation therapy and therefore the laminectomy allowed functional neuroimaging only at the T10 spinal cord region. However, this clinical limitation does not affect our main finding that the hemodynamic signal within the T10 area encodes bladder pressure. In fact, this finding supports the prevailing hypothesis that micturition is regulated by neural circuits in the brain and the spinal cord. When the sacral cord receives the sensory information from the bladder, this signal travels up the spinal cord to the higher centers in the pons and above [172]. Therefore, it is likely that the bladder pressure-related fUSI signal that we detect at T10 is initiated at the sacral cord and travels towards higher brain centers.

Furthermore, while it is common in animal spinal cord studies to perform large laminectomies, retract back muscles and remove connecting tissues [33,136–138], clinical studies do not allow modifications to the surgical protocol to improve the quality of the fUSI images. Instead, we can perform only partial and small laminectomies to avoid spine destabilization. In particular, the width of the laminar opening (about 11 mm) was smaller than the width of the ultrasound probe (12.8 mm) and consequently the probe did not perfectly abut to the dura. Therefore, it is challenging to image the same 2D plane across patients. Although the imaging planes slightly vary across the 6 patients, it does not affect the spatiotemporal pattern of the hemodynamic signal in the bladder-related regions. In fact, this highlights the strength and robustness of fUSI to overcome the potential to image different 2D slices of the spinal cord across patients.

Conclusions

Taken together, we present the first in-human characterization of spinal cord hemodynamics during physiological activation of the bladder. By combining fUSI with controlled-urodynamic bladder filling and emptying in human patients with spinal cord laminectomy, we identified spinal cord regions where the hemodynamic signal is strongly correlated with the bladder pressure. These findings demonstrate the existence of a network that is involved in micturition, and open new doors for further investigation of neural network circuits that control and regulate other body processes in healthy and disease conditions.

4.5 Materials and methods

4.5.1 Patients and surgical procedures

A total of six participants were imaged continuously during bladder filling and emptying in this study. The participants were recruited from patients who underwent standard-of-care implantation of a spinal cord stimulator paddle lead (PentaTM model 3228) at the Keck School of Medicine of the University of Southern California (USC). All patients were diagnosed with failed back syndrome, that required a T10 partial laminectomy for insertion of stimulation paddle lead in the prone position under general anesthesia (Fig. 4.1 C). Spinal cord hemodynamic responses to bladder filling and emptying were acquired via insertion of a fUSI probe into the T10 partial lamina opening (Fig. 4.1 A, B, C). Informed consent was obtained from all patients after the nature of the study and possible risks were clearly explained, in compliance with protocols and experimental procedures approved by the USC Institutional Review Board.

4.5.2 Patient bladder pressure signal acquisition

The urodynamic assessments in this study were conducted using the Laborie Goby urodynamics system to fill, empty and acquire continuous intravesical bladder pressure measurements of patients. A LaborieT-DOC catheter was inserted into the bladder, after patients were anesthetized. The position was confirmed by irrigation and aspiration. The infusion port of the catheter was connected to a drainage bag and the manometer port was connected to the Laborie UDS Roam Bluetooth transmitter. The patients were then positioned prone. To begin experiments, the infusion port of the catheter was connected to the infusion tubing and fUSI recordings were performed simultaneously with the urodynamics (See details of the experimental protocols below).

4.5.3 Functional ultrasound imaging data acquisition

The spinal cord hemodynamic signals were acquired with a fully featured commercial Iconeus One (Iconeus, Paris, France) fUSI system. A 128 elements linear array transducer probe with a 15 MHz center frequency, 0.1 mm pitch (Vermon, Tours, France) was inserted through laminar openings (Fig. 4.1 B) to generate fUSI pD intensity-based images. This approach enables image acquisition with spatial resolution of 100 μm × 100 μm in-plane, slice thickness of 400 μm, and field of view (FOV) of 12.8 mm (width) × 10 mm (depth). The penetration depth is sufficient to image almost the entire transverse cross-section of a human spinal cord, approximately 10-15 mm in diameter. The probe was fixed steadily throughout experiments with the field of view transverse and intersecting the spinal cord central canal (Fig. 4.1 A-C). Each image was obtained from 200 compounded frames using 11 tilted plane waves separated by 2° (i.e., from -10° to +10° increment by 2°), at a 500 Hz frame rate. Imaging sessions were performed using a real-time continuous acquisition of successive blocks of 400 ms (with 600 ms pause between pulses) of compounded plane wave images, with a 5500 Hz pulse repetition frequency. The acoustic amplitudes and intensities of the fUSI sequence remained below the Food and Drug Administration limits for ultrasonic diagnostic imaging (FDA, 510k, Trace 3).

4.5.4 Experimental protocol

A 26-minute continuous fUSI signal acquisition protocol was employed for all patients. The protocol consisted of 5 min baseline recording followed by simultaneous bladder intravesical pressure signal and spinal cord fUSI signal acquisition, including 2 bladder filling cycles and 1 emptying cycle, interspersed by 2 hold periods and a wash-out period at the end (Fig. 4.1 D). At the 5-minute mark, we filled the patients' bladder through a catheter with 600 ml of saline at a rate of 90 ml/min for approximately 6 min and 40 s, while simultaneously recording the bladder pressure. The filling is paused for 1 min and 30 s, followed by additional bladder filling with saline for 1 min. We stopped the pump for 1 min and 30 s and then reversed the pump to continuously withdraw saline via the catheter for 7 min and 40 s at a rate of 90 ml/min, with continuous recording of the bladder pressure. The pump is turned off, then followed by approximately 2 min and 20 s of additional fUSI spinal cord and bladder pressure signal recordings.

4.5.5 Data preprocessing

A built-in phase-correlation based sub-pixel motion registration [162] and singular-value-decomposition based clutter filtering algorithms [24,105], in the Iconeus One acquisition system were used to separate tissue motion signal from blood signal to generate relative fUSI pD signal intensity images [3]. We adopt rigid motion correction techniques [108] that have successfully been used in fUSI [28] and other neuroimaging studies [106,107,164] , to address potential physiological and motion artifacts unique to human spinal cord imaging. This was combined with in-house high frequency smoothing filtering. We utilized a lowpass filter with normalized passband frequency of 0.04 Hz, with a stopband attenuation of 60 dB that compensates for delay introduced by the filter, to remove high-frequency fluctuations in the pD signals.

4.5.6 Effects of bladder filling and emptying on SCBV

We assessed the spatial and temporal effects of bladder filling and emptying on spinal cord hemodynamics. In this regard, we generated pixel-wise activation time course curves of the SCBV changes as a percentage change of the pD signal relative to baseline activity for the whole spinal cord imaging FOV. The mean fUSI pD signal activity acquired 1min preceding the onset of the bladder filling was utilized as the baseline for the analysis. To visualize regional SCBV changes caused by the bladder filling and emptying processes, we computed SPMs to identify regions with statistically significant changes in pD signal during the filling and emptying periods relative to activity recorded from the baseline period. To account for the longer timescale (several minutes) of the urodynamics protocol, we performed a dynamic statistical parametric map analysis (dSPM). The dSPMs are computed based on two-sided Student's t-test with false discovery rate correction (FDR) to identify regions recorded within the spinal cord that are strongly affected by filling and emptying of the bladder across time compared to baseline activity. To do so, we compare the mean fUSI %pD signal change in each pixel within a 20 s sliding window to the baseline activity signal at 5 s steps.

4.5.7 Spatiotemporal correlation of bladder pressure changes to SCBV

We assessed the spatiotemporal effects of bladder filling and emptying on spinal cord hemodynamics. We generated pixel-wise activation time course curves of the spinal cord blood volume changes (ΔSCBV) as a percentage change of the pD signal relative to baseline activity for the whole spinal cord imaging field-of-view (FOV). The mean pD signal activity acquired 1 min preceding the onset of the bladder filling was utilized as the baseline for the analysis. We investigated whether there are spinal cord regions where ΔSCBV is correlated with the bladder pressure during filling and emptying. To test this hypothesis, we computed Pearson correlation coefficients for each pixel in the spinal cord fUSI image. To this end, the %pD signal intensity time series curve from each pixel is correlated with the bladder pressure signal across time to determine pixels with statistically significant correlation ($p < 0.01$, with FDR correction). We generate statistical correlation activation maps of the pixels that show significant positive and negative correlation above an r-coefficient threshold ($r > 0.35$ and $r < -0.35$). Finally, to visualize the temporal dynamics of the ΔSCVB, we derived the mean % pD signal change curves from averaging the signal over the pixels with significant correlation to the bladder pressure signal.

4.5.8 Decoding bladder pressure dynamics from SCBV

Next, we attempted to identify spinal cord regions with ΔSCBV that captures the temporal changes of the bladder pressure, without direct knowledge of the bladder pressure state. We utilized a machine learning algorithm cPCA+SVM that includes the following steps: 1) align the preprocessed SCBV signals extracted from the bladder filling and emptying time epochs, 2) reduce data dimensionality and select features that optimally allow discrimination between filling and emptying states, 3) dissociate and identify relevant spinal cord areas that encode the bladder pressure dynamics and 4) cross validate and evaluate the decoder performance (Fig. 4.4). To do so, we determined the percentage change in pD signal in each pixel of the fUSI images extracted during the filling and emptying epochs for each patient, relative to reference signal activity. The signals acquired 30 s just before the onset of filling and 30 s before onset of emptying were used as reference to calculate the %pD signal change for each pixel during the filling and emptying periods, respectively. The entire fUSI spinal cord 2D image space was utilized in the machine learning algorithm. Each 2D time series data was vectorized to 1D vectors and aligned in rows to form 2D (pixels × time) matrix classes (filling – class:0 and emptying – class:1) (Fig. 4.4b). We employed classwise principal component analysis (cPCA) [141,142] and support vector machines discrimination (SVM) [185,186], to reduce data sparsity and dimensionality while maintaining enough components to retain over 95% variance in the data and to select the most relevant subspaces to separate the classes. SVMs provide a set of supervised learning tools for classification that are effective for high dimensional spaces even when the feature dimensions are larger than the number of samples – such as the data employed in this study. We combined cPCA with SVM to classify the cPCA-transformed fUSI image into filling (class:0) and emptying (class:1) bladder pressure states. This analysis provides weights that reflect the most relevant pixels used for classifying between classes (Fig. 4.4 c). The relevant pixels represent a feature extraction mapping to the 2D spinal cord image space and are derived from the two 1D low-dimension subspaces that are optimized for each class. The subspaces identify pixels in the spinal cord fUSI images that encode the differences between the filling and emptying classes, when projected back to the image space. Each pixel is assigned a relative weight of relevance (normalized between [-1 1] – pixels with values close to +1 or -1 indicate high relevance components, while pixels with values close to 0 are less important and whose fluctuations are likely due to noise). ΔSCBV of pixels with positive and negative relative weights of relevance are positively and negatively correlated with bladder pressure changes, respectively.

4.5.9 Optimum data amount for decoder training

Next, to investigate the optimum amount of data needed to generate the best correlation between ΔSCBV and bladder pressure, we employed a similar cPCA+SVM analysis as outlined above with a sliding window of cumulative data amounts. We utilized 30 s of initial data followed by 10 s increments to derive the cumulative data used to train and cross-validate the classifier. We assumed that data acquired at the end of the filling period are more comparable to the data acquired at the onset of emptying and thus, we accumulated the filling data in reverse order (Fig. 4.4 D). We followed comparable cPCA and SVM classification steps as outlined above with the increasing data amounts. Each data amount produced a corresponding relevant weighted pixels-matrix and associated mean % pD signal change time course curve (Fig. 4.4 D, highlighted panel), relative to the reference activity. To determine the optimum amount of data and pixel weights, we utilized the mean % pD signal changes derived from the weighted regions for each patient to determine the correlation between the pD signal curve resulting for each cumulative data amount and the bladder pressure signal (Fig. 4.4 D). The data amount corresponding to the highest correlation coefficient is utilized to select the optimum pixel weights and % pD signal change curve. To cross-validate the classification analysis, we allocated a subset from each data class for training (80%) and testing (20%).

4.5.10 Software analysis

All data pre- and post-processing and statistical analysis were performed using Matlab Version 9.13.0.2193358 (R2022b).

Chapter 5

Effects of Aberrant Seizure Condition and Non-Invasive Neurostimulation on Local Brain Connectivity in Humans as Measured by Functional Ultrasound Imaging

Reprinted with permission from Agyeman K, et. al.

5.1 Abstract

Over 70 million people suffer from epilepsy syndrome and associated neurological conditions world-wide, with severe health and economic burdens. Neuromodulation therapy offers the only viable alternative for many patients whose epileptic conditions are refractory to medication or unsafe for surgical resection. While advances in neurostimulation therapy have resulted in clinically approved options such as deep brain stimulation of the anterior nucleus of the thalamus, vagus nerve stimulation, or responsive neurostimulation for treating

drug-resistant focal epilepsy, several intrinsic drawbacks remain. All are invasive, palliative, and sub-optimal with regards to long-term outcomes, primarily because the mechanisms of action of how these techniques control seizure conditions remains speculative at best. While common peroneal nerve stimulation (PNS) a non-invasive neurostimulation technique is gaining some attention to investigate and/or control cortical seizure activity, how it modulates cerebral hemodynamics and local connectivity remains a mystery. Here we leverage functional ultrasound imaging, a recently introduced neuroimaging technique that offers substantially closer connection to underlying neural signal to study the effects of aberrant seizure condition and PNS on local brain connectivity in humans. We acquired interictal brain fUSI pD intensity signal through a cranial window from patients undergoing standard-of-care surgical resection of aberrant seizure onset zones and demonstrate that aberrant epileptic-seizure brain state causes distinct changes to local brain connectivity and network activity via a reduction of cross-correlation coefficients. We extend the findings to show that a PNS protocol causes distinct disruption to local brain network-connectivity when the stimulator is turned on. The fact that PNS affects local brain connectivity establishes fUSI as a vital investigative tool that may potentially provide an analytical measure to localized aberrant seizure-prone brain areas and evaluate the effectiveness of a PNS protocol – ultimately opening avenues for further investigation and applications in research and clinical setting.

5.2 Introduction

Epilepsy is a neurological condition of the brain that causes patients to be more susceptible to having spontaneous unprovoked and recurrent seizures (two or more episodes) – not including seizures caused by conditions such as high fever, drug withdrawal or low blood sugar [187,188]. Neurologically, seizures are believed to occur when network connections in the brain malfunction leading to uncontrollable firing of neurons. While some epileptic seizure conditions can be treated with medication, over 30% of patients are antiepilepsy drug resistant [187,189,190] and thus patients may opt for neurostimulation therapy or surgery. Currently, surgical resection of the epileptogenic brain region remains the gold standard for long-term cessation of drug-resistant focal epilepsy [191,192]. However, if the epileptic source originates from eloquent or other untenable brain regions, then neurostimulation might be the only viable alternative for treatment [193].

Interest in the utilization of neuromodulation to treat conditions associated with neurological disorders is rapidly rising. Specifically, treatment of epilepsy-syndrome conditions has seen tremendous advancements over the past few decades. Patients whose epileptic seizure conditions are refractory to pharmacotherapy may opt for deep brain stimulation of the anterior nucleus of the thalamus (ANT-DBS) [194], vagus nerve stimulation (VNS) [195], or responsive neurostimulation (RNS) [196]. To date, ANT-DBS, VNS, and RNS are the only neurostimulation therapies approved by the FDA to treat the indication of refractory focal epilepsy. Until the recent introduction of a closed-loop version that automatically initiates stimulation based on pre-defined changes in heart rate, VNS was traditionally considered an open-loop method that operated by stimulating the left vagus nerve at a pre-defined schedule [195,197]. VNS is believed to modulate the brainstem, thalamic, and cortical afferent projections, including the catecholaminergic nuclei and limbic regions, based on acute and chronic stimulation [195198,199]. Other studies indicate that other mechanisms including alteration of GABAergic function, might mediate long-term improvement in seizure control by VNS [195,200–204]. RNS is a close loop neurostimulation technique that continuously monitors intracranial EEG at zones of suspected seizure onset or foci and delivers short bursts of high frequency electrical stimulation upon detection of aberrant EEG signal to quench potential impending seizure [193,205]. Although its MOA remains speculative, ANT-DBS is believed to modulate activity of the anterior nucleus of the thalamus and connecting Papez circuit [206–208]. While ANT-DBS, VNS and RNS treatment outcomes are promising and work well for certain patients, there are intrinsic drawbacks associated with each approach. All three techniques are palliative and not curative. The median reduction in seizure frequency 3 months post neurostimulation intervention is less than 50% in all three approaches. More importantly they share a unifying disadvantage that they are all invasive – requiring various degrees of surgery to implant stimulating electrodes. Material dysfunction, implantation-related intracranial hemorrhage as well as long term mood and memory disorders have been reported [194,196,209].

While most studies and application of common peroneal nerve stimulation (PNS) is largely associated with motor function impairment, chronic pain conditions, gait, or spinal cord injury rehabilitation [210–217], there are growing indications to believing that PNS may have utility for investigating and/or treating aberrant neurological seizure conditions. Related evidence from a preclinical rat model of epilepsy study shows a reduction in occurrence of behavioral seizures, upon electroacupuncture stimulation of the hindlimbs [218]. PNS is minimally invasive when precise targeting of nerve fibers is required but can be employed non-invasively in research and clinical settings, a tremendous advantage over existing seizure control neurostimulation approaches – ANT-DBS, VNS and RNS. As a mixed nerve, stimulation of the common peroneal is believed to activate motoneurons, cutaneous afferents and muscle afferents [216]. Stimulating the PN can induce, motor evoked potentials via efferent discharge that causes potentiation at the level of the spinal motoneuron or neuromuscular junction. Afferent input to the cortex may also induce disinhibition or increase excitability [215] – with cortical plastic implications. Long-lasting sensorimotor cortical reorganization have been reported in healthy subjects who receive repetitive electrical stimulation of the common peroneal nerve [215,217]. However how PNS affects cortical hemodynamic activity or local brain connectivity remains a mystery.

Functional ultrasound imaging is a relatively new neuroimaging technique that enables large-scale estimates of neural activity through measures of cerebral blood volume. fUSI provides closer connection to underlying neuronal signal than achievable with other hemodynamic methods and offers a unique combination of high spatiotemporal resolution and high sensitivity to blood flow across a large field of view. fUSI has already been proven to be an effective tool for imaging large-scale brain activity and epileptic activity in preclinical and clinical studies [1,30,31,219]. As such, it is well-positioned to improve our understanding of the impacts of aberrant seizure prone brain activity and PNS on large-scale brain networks before, during and after stimulation. While fUSI has been utilized to investigate epilepsy, ictal or ictal-interictal seizure activity states were assessed in these studies [30,31,219]. This required chemical or genetic induction of the ictal seizure conditions, with associated drawbacks which can be burdensome to subjects.

Here in this study, we characterize modulations to brain hemodynamics induced by aberrant seizure conditions in patients suffering chronic refractory severe epileptic seizures. We acquired interictal brain fUSI pD intensity signal through a cranial window from patients undergoing standard-of-care surgical resection of aberrant seizure onset or foci regions. We demonstrate that aberrant epileptic-seizure brain state causes distinct changes to local brain connectivity and network activity via a reduction of cross-correlation coefficients derived from neighboring healthy brain regions after surgical resection of aberrant seizure brain foci.

We extend the findings to assess how a non-invasive electrical stimulation of the common peroneal nerve of the lower limb evokes specific changes to cortical network-activity and show that a PNS protocol causes distinct disruption to local brain network-connectivity when the stimulator is turn on.

5.3 Results

To characterize modulations to brain hemodynamics induced in aberrant seizure-prone brain tissue and assess how electrical stimulation of the common peroneal nerve of the lower limb evokes specific changes to cortical network-activity, we recruited nine (9) patients who underwent surgery to remove drug-resistant severe epileptic-seizure zones (Fig. 5.1 A-B). We acquired interictal activity through a cranial window using a miniaturized 15.6-MHz fUSI linear array transducer placed to abut the dura or cortical surface of the brain (Fig. 5.2 A). fUSI signal acquired from healthy non-seizure (pre- and post-resection, N=6, n=10, each) and aberrant seizure-prone (pre-resection, N=5, n=11) brain regions (Fig. 5.1 D), produced pD intensity ultrasound images of the brain with spatial resolution of 100 μm x 100 μm in-plane, 400 μm slice thickness and an FOV of 12.8 mm x 10.0 mm. The duration of the recordings from each region was between 60 – 180 s (Fig. 5.1 C-D).

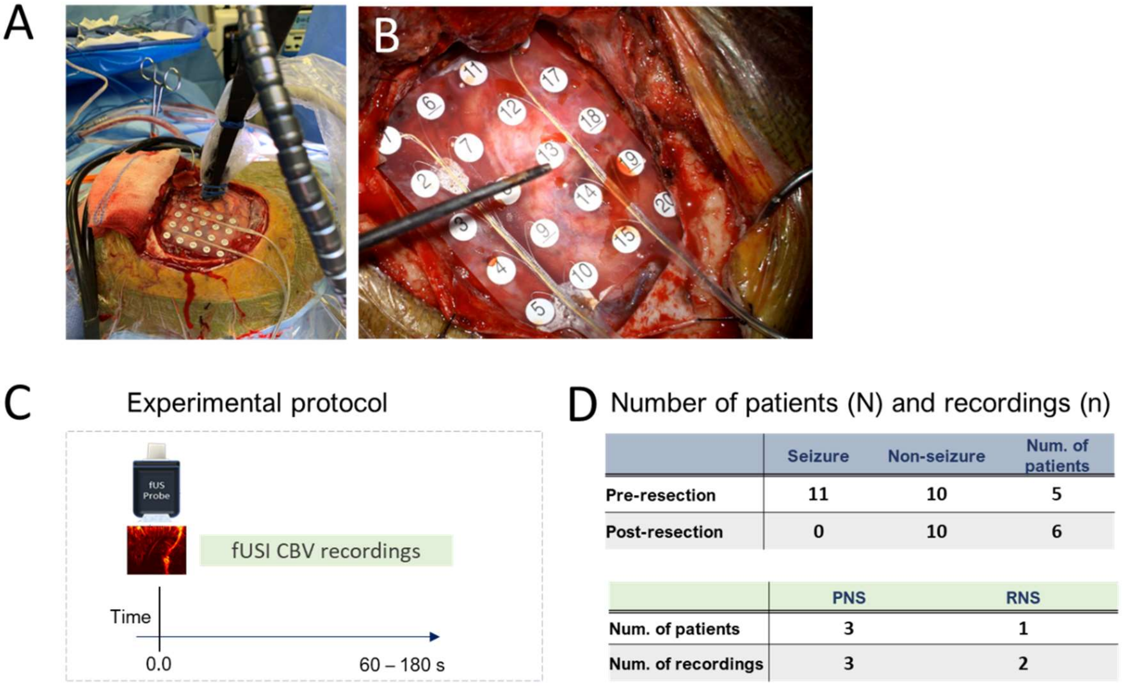

	Seizure	Non-seizure	Num. of patients
Pre-resection	11	10	5
Post-resection	0	10	6

	PNS	RNS
Num. of patients	3	1
Num. of recordings	3	2

Figure 5.1 Surgical procedure, fUSI acquisition and experimental protocol. A-B) Patients undergo a craniotomy under general anesthesia to surgically remove brain tissue from epileptics-seizure foci. Intra-electrocorticography brain mapping was employed for detection of aberrant seizure-active and normal healthy regions. C) Functional ultrasound imaging and experimental protocol for acquiring interictal signal from healthy and aberrant seizure brain regions pre- and post- resection – guided by ECoG brain mapping. D) Breakdown of acquisition protocol and the number of patients and recordings.

The pD intensity images reveal anatomical vascularization of the brain across all patients from the different recorded regions – typical recordings from each region shown (Fig. 5.2 B-D). Note that while the location of fUSI signal acquisition varies across patients, as it depends on the specific location of seizure onset zone, the recordings were mostly from motor-sensory cortical and hippocampal regions of the brain.

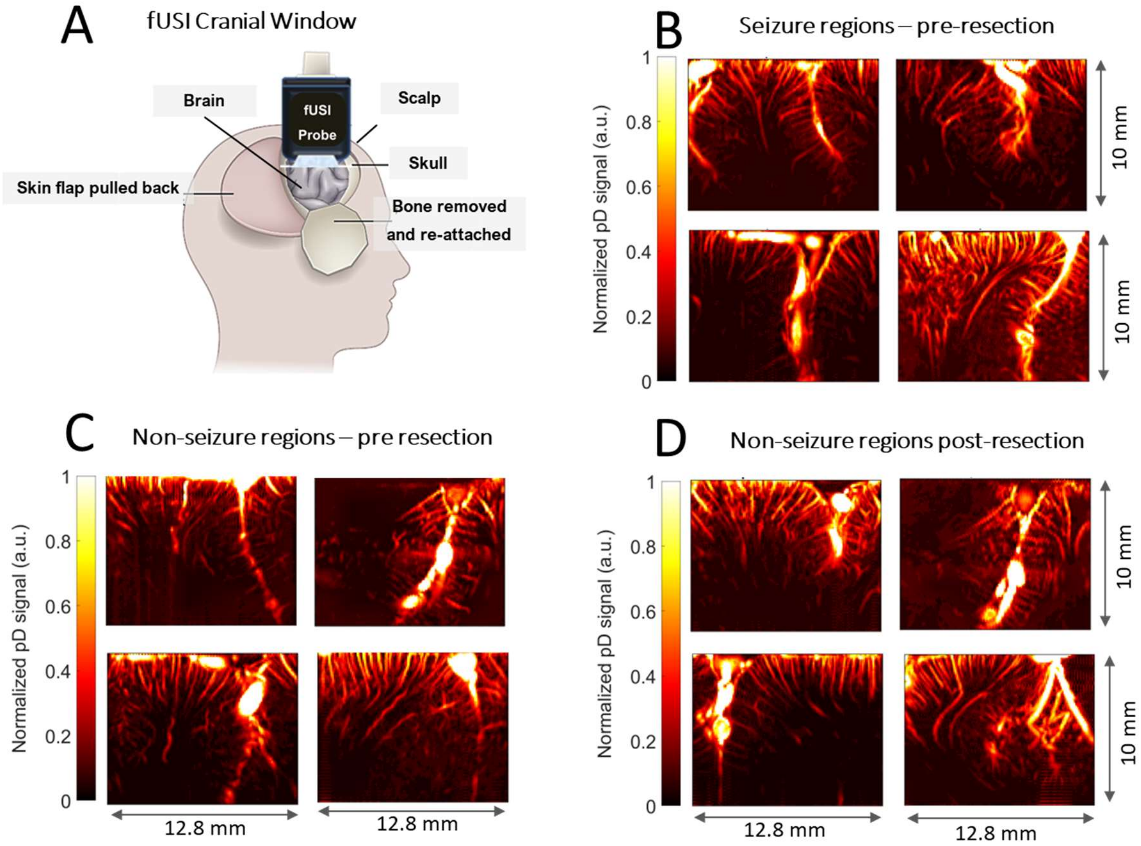

Figure 5.2 Functional ultrasound imaging of the brain interictal activity. A) Schematic representation of the fUSI of the cortex through a cranial window and a craniotomy brain anatomy. B-D) Power Doppler-based ultrafast ultrasound images acquired from seizure and non-seizure brain regions of patients in transverse view. The field of view captures part of the anatomical vascularization of the brain below the dura.

5.3.1 Aberrant seizure condition evokes changes to local brain connectivity.

To assess characteristic modulation to connectivity of local activity induced by aberrant seizure-prone brain tissue, we hypothesized that due to increased synchrony of activity in abnormal active seizure-prone regions, we expect differences in the levels of local regional autocorrelation between healthy and aberrant seizure brain regions – even during interictal state. To test our hypothesis, we conducted a Pearson's cross-correlation analysis separately on fUSI brain signals acquired from aberrant seizure brain regions before surgical resection, and signal from adjacent healthy brain regions near the abnormal regions before and post resection. The local interictal activity connectivity differences were evaluated by comparing the mean and median cross-correlation coefficients (CC) derived from seizure-onset regions and compared to CCs calculated from adjacent healthy regions. To do so, each image is discretized into equal 6 x 6 ROIs to extract the mean pD intensity signal across time (60 – 180 s) for each ROI, which is subsequently used to determine the Pearson's cross-correlation coefficient for each image (Fig. 5.3 A). While the mean and median CCs across fUSI images acquired from the healthy brain regions ($r_{Mn} = 0.55 \pm 0.06$ Mean ± SE, $r_{Mdn} = 0.58 \pm 0.08$ Median ± SE) show lower but not significant mean and median CCs, compared to the aberrant seizure regions ($r_{Mn} = 0.64 \pm 0.06$ Mean ± SE, $r_{Mdn} = 0.67 \pm 0.07$ Median ± SE) (Fig. 5.3 B), nonetheless the observed difference in connectivity is encouraging. The challenge in this approach is that we compare CCs derived from different brain regions.

To address this challenge and assess whether removal of aberrant seizure-prone brain tissue changes the local connectivity of nearby healthy regions, we compare the CCs of the same healthy regions pre- and post-resection of the aberrant brain tissue. We find a significant ($p < 0.05$) decrease in mean and median CCs derived from the neighboring healthy brain regions pre- ($r_{Mn} = 0.55 \pm 0.06$ Mean ± SE, $r_{Mdn} = 0.58 \pm 0.08$ Median ± SE) and post-resection ($r_{Mn} = 0.41 \pm 0.03$ Mean ± SE, $r_{Mdn} = 0.41 \pm 0.03$ Median ± SE) (Fig. 5.3 B). The mean CCs matrices show a clear decrease in the intensity from pre-resection (red orange) to post-resection (orange yellow) (Fig. 5.3 C, middle and right panels).

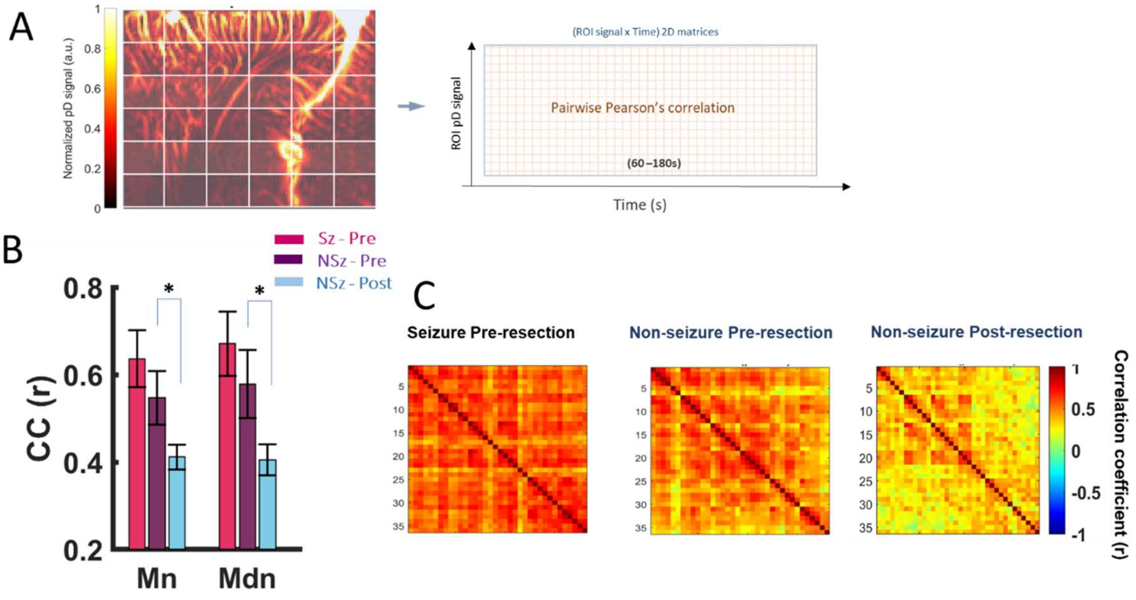

Figure 5.3 Flowchart of analysis used to assess brain local connectivity from fUSI signal and modulation to local connectivity induced by normal and aberrant brain states. A) The fUSI brain images are discretized into equal 6 x 6 ROIs and transformed into a 2D ROI mean pD signal across time. Local connectivity is evaluated from the mean and median Pearson's CC analysis between all ROIs and across each image. B) Mean (Mn) and median (Mdn) cross-correlation coefficients across fUSI signal acquired from aberrant seizure regions, pre-resection (Sz-pre) and neighboring healthy brain regions, pre- and post-resection (Nsz-Pre and Nsz-Post). There is a significant decrease in CCs for the healthy brain regions from pre- to post-resection. C) Mean Pearson's cross-correlation coefficient matrix showing the connectivity levels for fUSI signal acquired from seizure-prone regions (red), non-seizure regions, pre resection (red orange) and same non-seizure regions, post resection (orange yellow).

Together the results appear to indicate that aberrant seizure conditions modulate the local brain connectivity within and around abnormal seizure brain foci and is encoded in the correlation of local fUSI interictal pD intensity signals. The significant reduction in local brain connectivity after surgical removal of the aberrant seizure brain tissue appears to validate this conclusion.

5.3.2 Effects of PNS on cerebral hemodynamics

To investigate how common PNS evokes specific spatial and temporal hemodynamic changes, we utilized a stimulation protocol that consisted of 3 ON-OFF stimulation cycles, with each cycle containing a 2 min ON period (stimulation ON) and a 1 min OFF period (stimulation OFF), with simultaneous fUSI signal acquisition. The PNS was preceded by 3 min of baseline fUSI interictal recording. An FDA approved Geko common peroneal nerve stimulator was employed in which bi-polar electrodes were placed on the lower limbs to deliver stimulation at a burst frequency of 1.0 Hz and 140 or 280 µs pulse width, at sub- and motor-threshold levels (Fig. 5.4). All three patients received the same stimulation protocol.

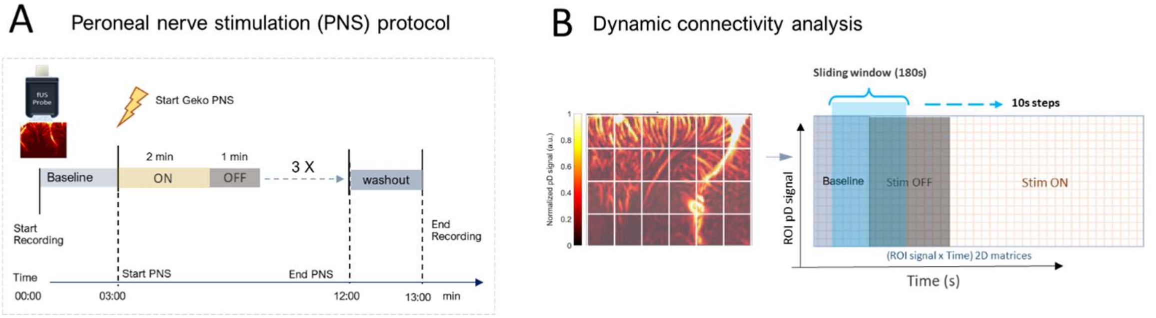

Figure 5.4 PNS protocol and flowchart for dynamic local connectivity modulation detection from the fUSI signal. A) Peroneal nerve stimulation protocol. A continuous fUSI recording protocol consisting of 3 min baseline signal recording, followed by acquisition during 3 cycles of PNS consisting of 2 min stimulation ON and 1 min stimulation OFF trials was utilized. This is followed by an additional 1 min of fUSI recording after offset of stimulation. B) fUSI brain images acquired from aberrant seizure onset regions during baseline, stimulation OFF and stimulation ON were time-aligned and discretized into equal 6 x 6 ROIs to extract mean pD signals across time. Using a sliding window, 180 s long with 10 s steps, changes to the mean and medium cross-correlation coefficients were assessed between the ROIs for each step.

To characterize how PNS induces changes in brain hemodynamics, we compute statistical parametric maps based on two-sided Student's t-test with false discovery rate correction. The SPMs were generated by comparing brain fUSI signal acquired during the stimulation ON trials to the signal acquired 20 s preceding the stimulation ON trials at the end of the stimulation OFF trials. The SPMs identify regions recorded within the brain that are strongly affected by the stimulation protocol. The results showed that PNS evokes strong spatial and local hemodynamic changes in the brain (Fig. 5.5 A). We detect changes to CBV within the sensory-motor cortical regions of the brain when the stimulator is turned on and a cessation of activation when the stimulator is off – see supplementary video (S-vid. 5.1). To assess the temporal dynamics of the activated brain regions, we also generate event related average waveforms. The waveforms represent the brain cerebral blood volume changes, that is derived as a percent change relative to the 20 s mean reference activity across time. They illuminate the temporal patterns of the hemodynamic changes of the brain during stimulation. We assess the combined (pseudo-global, i.e., the mean activity across activated pixels) response. The patterns reveal that stimulation causes strong regional changes in blood flow in all 3 patients (Figs. 5.5). Notably, we observe rising (red curves) and falling (blue curves) ERA curves for the activated regions when the stimulator is turned on – both returning to the reference activity level when the stimulator is turned off. (See S-vid. 5.1 in supplementary materials for a movie showing the activation in sensory and motor regions of the brain when the PN stimulation is turned on). While one may argue that the stimulation ON signal should be compared to the baseline activity before the onset of PNS, we compared stimulation ON to the last 20 s of simulation OFF trials signals to minimize potential washout effects – as the duration of time that it takes for that hemodynamic signal to return to baseline activity is unclear.

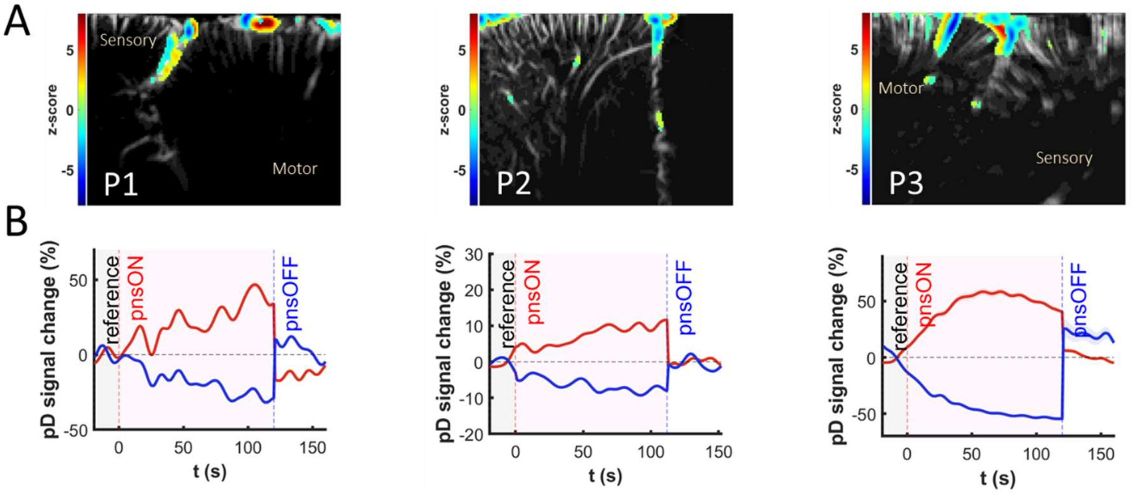

Figure 5.5 Statistical parametric map and event-related average waveforms. A) Statistical map shows localized areas with significantly higher or lower CBV with respect to reference activity during stimulation OFF (two-sided t test of area under the curve, $p < 0.05$, FDR corrected for number of pixels in image). The SPMs are overlaid on grayscale baseline mean pD intensity images. B) ERA waveforms of the pseudo-global activated pixels in the SPMs that exhibit strong increased changes of blood perfusion (red curve) or that exhibit strong decrease change of blood perfusion (blue curve), after turning on the stimulator. The pseudo-global ERA waveform is determined as the mean %pD signal change across the SPM activated pixels above a threshold (z-score ≥ 0.6) with respect to the reference activity during stimulation OFF trials.

5.3.3 Peroneal nerve stimulation reduces local brain connectivity.

The capability to assess the effects of PNS on local brain connectivity from interictal fUSI signal could have tremendous consequences for clinical translation. One way to evaluate whether a PNS protocol causes changes to local brain hemodynamic connectivity would be to measure how the Pearson's CCs local connectivity measure developed in the previous section changes during the stimulation ON and OFF trials. To implement this, we developed a dynamic local brain connectivity analysis approach to determine the evolution of local connectivity over time – measured by the mean and median CCs as a function of time. We time-aligned the fUSI signal acquired during baseline, the stimulation OFF and ON trial periods into a 3D (image-space x time) matrix (Fig. 5.4 B). Note the fUSI signal utilized for this analysis were acquired from aberrant seizure-prone brain regions before resection. Following a similar approach as outlined above we discretized the image space into equal 6 x 6 ROIs and transformed the matrix into a 2D space consisting of each ROI's mean pD intensity signal across time. Then employing a sliding window consisting of 180 s long data, with 10 s steps, we derived the Pearson's cross-correlation coefficient for each section of data, at each step (Fig. 5.4 B). We begin with the baseline data and progressively assess the connectivity through the concatenated stimulation OFF and ON trials signals. The analysis shows that PNS evokes distinct changes to the local brain connectivity. We observe strong CCs ($r>0.5$) during the baseline activity and periods when the PNS stimulator is turned off. However, there is a clear, sharp, and consistent drop in the CCs ($r< 0.5$) during the periods when the PNS stimulator is turned on, across all patients (Fig. 5.6 A-B, see supplementary video, S-vid 5.2). The decrease in cross-correlation coefficients during the stimulation ON trials suggests that PNS causes a disruption to the local brain hemodynamic signal connectivity.

Together these results demonstrate the capability of fUSI to detect and characterize specific interictal hemodynamic characteristics associated with pD signal acquired from normal and aberrant seizure-prone regions in epileptic-seizure patients. The fact the common PNS non-invasive neuromodulation affects the local connectivity measure is a novel and promising outcome that establishes fUSI as a vital investigative tool that may potentially provide an analytical measure to localized aberrant seizure brain areas and evaluate the effectiveness of a common peroneal nerve stimulation protocol.

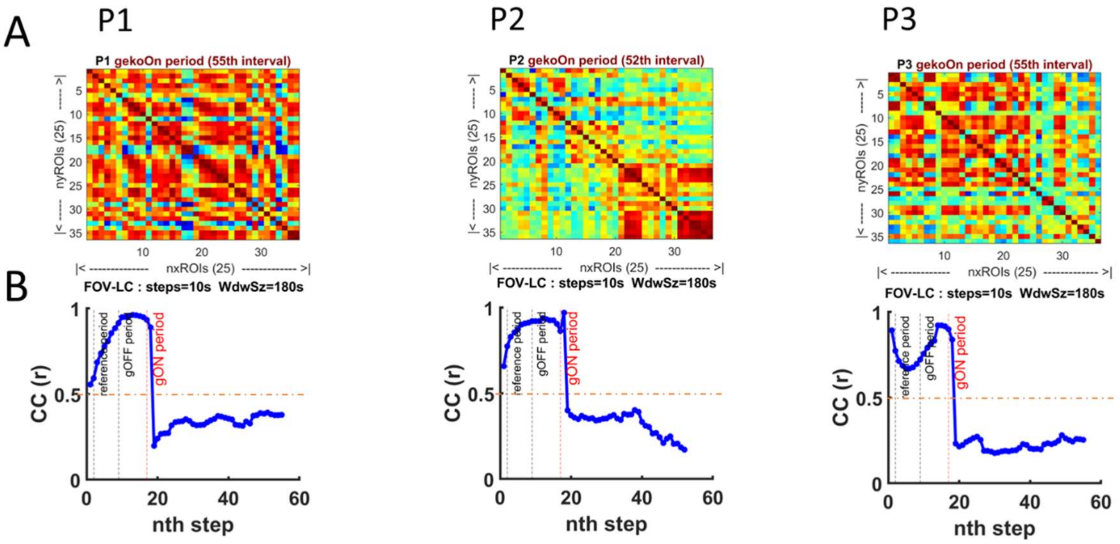

Figure 5.6 Dynamic local connectivity of the brain evoked by PNS (N=3). A) Representative local connectivity Pearson's cross-correlation matrix. A 36 x 36 matrix that shows the CCs for the cross-correlation calculation between the 36 ROIs in the fUSI brain image space. B) Changes of the local brain connectivity, measured as CCs over time – at each sliding window of data step. There is a drop in CCs going from baseline and PN stimulation OFF to ON trial periods below a threshold ($r < 0.5$). The image space was discretized into equal 6 x 6 ROIs in the 3D (image x time) matrix which is transformed into a 2D space consisting of each ROI's mean pD intensity signal across time. A sliding window consisting of 180 s long data, with 10 s steps, was used to derive a Pearson's cross-correlation coefficient for each section of data, at each step across time.

5.4 Discussion

4.4.1 General

fUSI is an emerging neuro-monitoring modality that enables large-scale estimates of neural activity through measures of cerebral blood volume. Spatiotemporal and sensitivity enhancements to fUSI now provide closer connection to underlying neural activity signal than achievable with other hemodynamic methods [1,2]. Therefore, it is well-positioned to improve our understanding of the impacts of epileptic-seizure conditions on brain hemodynamics and peroneal nerve stimulation on local brain network activity before, during and post stimulation. In fact, fUSI has already been proven to be an effective tool for imaging large-scale brain activity and epileptic activity in preclinical and clinical studies [1,30,31,219]. While these studies have improved our understanding and shed light on brain dynamics during seizure, most of the studies where limited to preclinical animal models and their findings relied on the assessment of ictal seizure events. In this study, we extend fUSI in epilepsy-seizure research by recording interictal characteristics of aberrant and normal brain conditions as well as non-invasive peroneal nerve stimulation on local brain connectivity. We demonstrate that aberrant epileptic-seizure brain state causes distinct changes to local brain connectivity and network activity, measured via a reduction of cross-correlation coefficients between fUSI interictal brain signal. We extend the findings to show that a PNS protocol causes distinct disruption to local brain network-connectivity when the stimulator is turned on. Our capability to characterize differences in local brain connectivity and to demonstrate that PNS modulates the local brain connectivity measure, establishes fUSI as a vital research and clinical tool to investigate further, functional, and dysfunctional epileptic brain anatomy that may potentially localized aberrant seizure brain zones and to evaluate the effectiveness of a PNS protocol.

4.4.2 Novel avenues for treating and improving neurostimulation therapeutics for drug-resistant focal epilepsy.

Epilepsy syndrome and its associated neurological conditions affect over 70 million people world-wide, with devastating health and economic burdens [187,188]. Patients suffer recurrent unprovoked seizures when network connections in the brain malfunction. Deep brain stimulation of the anterior nucleus of the thalamus [194], vagus nerve stimulation [195,220], and responsive neurostimulation[196]are promising alternative FDA approved neurostimulation treatment options for chronic drug-resistant focal epilepsy. While ANT-DBS, VNS and RNS neurostimulation treatments offer potential as palliative epileptic seizure-control in patients suffering from severe drug-resistant focal epilepsy, their mechanism of action remains speculative. Although, VNS is believed to modulate the brainstem, thalamic, and cortical afferent projections, including the catecholaminergic nuclei and limbic regions, based on acute and chronic stimulation [195,198–204,221] and ANT-DBS is believed to modulate activity of the anterior nucleus of the thalamus and connecting Papez circuit[206–208,222], the MOA of RNS is largely unknown. Primarily, this is due to the lack of a neuromonitoring modality that can characterize the effects of neurostimulation on epileptic ictal and interictal brain activity. Combining fUSI with neurostimulation of epileptic brain has considerable promise in gaining a better understanding of the MOA subserving how neurostimulation suppresses seizure conditions in patients with severe focal epilepsy.

Additionally, ANT-DBS, VNS and RNS neurostimulation therapies are invasive. All require surgery at various degrees of invasiveness to implant the stimulating electrodes –

resulting in several reported complications, including material dysfunction, implantation-related intracranial hemorrhage as well as long term mood and memory disorder [194,196,209]. The possibility of a non-invasive neurostimulation treatment option for epilepsy will be groundbreaking. The utilization of fUSI to study the effects of non-invasive neurostimulation techniques such as the common peroneal nerve stimulation on brain hemodynamics and local brain connectivity dynamics may have utility for assessing the potential of non-invasive neurostimulation therapy for epilepsy and for improving the efficacy of existing invasive neurostimulation techniques.

Challenges and limitations

4.4.3 Invasiveness nature of fUSI

While enhancements to fUSI allow a closer access to large-scale local neural activity in brain and spinal cord functional studies, fully leveraging the sensitivity improvements require the removal of brain skull or spinal cord lamina bones [26137,176] – as they attenuate and distort acoustic waves transmitted at high frequencies. Consequently, most preclinical, and clinical applications of fUSI thus far are minimally invasive – unless in young mice (8-12 weeks old) [159] or in pediatrics (fontanelle-imaging) [31,32]. Therefore, signal acquisition of ictal and interictal brain activity with or without neurostimulation in awake patients without a craniotomy is challenging and has yet to be demonstrated. Alternatively, the recent evidence of the capability of fUSI to record brain activity through a permanently implanted cranial “acoustic window”, suggests that non-invasive brain activity signal acquisition appears to be feasible [182]. Additionally, by intravenously injecting microbubble contrast-agents to enhance fUSI signal sensitivity, non-invasive intraoperative brain signal acquisition was recently demonstrated

[160,183]. These approaches establish the imminence and wide-spread utilization of fully noninvasive fUSI for brain studies. Here in this study, while the use of microbubble enhancement was not permitted due to strict operating room protocols, it was not needed as the patients required a standard-of-care craniotomy surgical procedure to resect epilepsy seizure onset zones or foci. This enabled direct access to the underlying cortical brain tissue. Nonetheless, the ability to assess the effects of aberrant seizure condition and non-invasive stimulation in awake subjects will enrich our understanding tremendously.

Conclusions

In total, we present the first in-human characterization of brain hemodynamics in response to pathophysiological epilepsy condition and non-invasive common peroneal nerve stimulation. By combining fUSI with cycles of electrical stimulation in severe drug-resistant focal epilepsy patients with craniotomy, we detected characteristic changes to local brain connectivity in aberrant seizure-prone and pre- and post-resection healthy neighboring cortical regions, as well as identified brain regions where the hemodynamic signal is strongly activated when a non-invasive peroneal nerve stimulator is turned on. These findings open new avenues for further investigation of function and dysfunction associated with aberrant epilepsy-syndrome conditions, their detection and treatment.

5.5 Materials and methods

5.5.1 Patients and surgical procedures

In this study nine subjects were recruited to acquire fUSI signal of the brain during stimulation and surgery. The participants were drug-resistant severe epileptic patients who underwent a standard-of-care craniotomy surgical procedure to remove aberrant seizure brain foci tissue at the Keck School of Medicine of the University of Southern California. The patients were diagnosed with anti-epilepsy drug-resistant seizure status that required resection. fUSI brain hemodynamic activity was acquired via insertion of the transducer probe through a cranial opening onto the cortical surface (Fig. 5.2 A). Informed consent was obtained from all patients after the nature of the study and possible risks were clearly explained, in compliance with protocols and experimental procedures approved by the USC Institutional Review Board.

5.5.2 ECoG intraoperative brain mapping

The assessment of brain epileptic-seizure state and mapping to identify candidate aberrant seizure foci tissue, were conducted using intraoperative ECoG electrode placement for cortical mapping. Electrode grids of the ECoG brain activity mapping system was placed onto the epi- or inserted into sub-dural brain spaces to record synchronous and asynchronous activity (Fig. 5.1 A-B) to discriminate active and aberrant seizure-prone brain regions from normal brain regions. The patients were anesthetized. The results of the ECoG brain mapping were utilized to guide placement of the fUSI probe for interictal activity recordings with and without stimulation.

5.5.3 Experimental protocol

All the patients received two modes of fUSI:

a) interictal fUSI of active seizure regions simultaneously with non-invasive electrical stimulation

b) interictal fUSI of aberrant active seizure brain regions – pre-resection, and interictal fUSI on neighboring healthy non-active brain regions – pre- and post- resection.

In the second fUSI mode, the interictal brain signals were acquired for 60 s – 180 s (Fig. 5.1 C). The brain's seizure activity states were confirmed with ECoG intraoperative brain mapping in both modes. We employed simultaneous stimulation and continuous signal acquisition protocol beginning with 3 min fUSI baseline recording, followed by a 3 ON-OFF cycles of common peroneal nerve stimulation protocol, with each cycle containing 2 min ON period (stimulation ON) and 1 min OFF period (stimulation OFF). This was followed by 1 min additional fUSI recording after the stimulation offset (Fig. 5.4 A). The protocol involved bipolar stimulation of the lower limb region at the middle contacts, utilizing 1.0 Hz burst frequency, 140 or 280 μs pulse width and 27 mA current amplitudes. Three patients received the PNS protocol.

5.5.4 Functional ultrasound imaging data acquisition

A commercial functional ultrasound acquisition system, Iconeus One (Iconeus, Paris, France) was utilized to acquire fUSI brain activity images via a transducer probe inserted through a cranial window (Fig. 5.2 A). A 128 elements linear array transducer with 15 MHz center frequency, 0.1 mm pitch (Iconeus, Paris, France) was used to generate fUSI images with spatial resolution of 100 μm × 100 μm in-plane, slice thickness of 400 μm, FOV of 12.8 mm (width) × 10 mm (depth) and maximum penetration depth of about 20 mm. The probe was fixed steadily throughout experiments with the FOV transverse to the dural or cortical surfaces (Fig. 5.2 A). To increase the signal-to-noise-ratio, we obtained each image from 200 compounded frames acquired at 500 Hz frame rate, using 11 tilted plane waves separated by 2° (i.e., from -10° to +10° increment by 2°). Images were acquired with a 5500 Hz pulse repetition frequency. Imaging sessions were performed using a real-time continuous acquisition of successive blocks of 400 ms (with 600 ms pause between pulses) of compounded plane wave imaging. The acoustic amplitudes and intensities of the fUSI sequence remained below the Food and Drug Administration limits for ultrasonic diagnostic imaging (FDA, 510k, Trace 3).

5.5.5 Data processing

A built-in phase-correlation based sub-pixel motion registration [162] and singular-value-decomposition based clutter filtering algorithms [24,25,105], in the Iconeus One acquisition system were used to separate tissue motion signal from blood signal to generate relative fUSI pD signal intensity images [2]. We employed rigid motion correction techniques [108] that have successfully been used in fUSI [28] and other neuroimaging studies [106,107], to address potential physiological and motion artifacts unique to human spinal cord imaging. This was combined with in-house high frequency smoothing filtering. We utilized a lowpass filter with normalized passband frequency of 0.04 Hz, with a stopband attenuation of 60 dB that compensates for delay introduced by the filter, to remove high-frequency fluctuations in the pD signals.

5.5.6 Local connectivity analysis

To investigate how aberrant seizure-prone brain regions induces characteristic modulation to local brain network-connectivity, we acquired fUSI brain pD signal from aberrant brain regions before resection and adjacent close-by healthy regions near regions earmarked for resection. The same healthy regions were imaged before and after surgical removal of the aberrant brain regions. To assess the local brain connectivity differences between aberrant and healthy brain regions, we conducted a Pearson's cross-correlation analysis on fUSI interictal signals acquired from aberrant seizure-prone and adjacent healthy brain regions before resection. To do so, each image is discretized into equal 6 x 6 ROIs to extract the mean pD intensity signal across time (60 – 180 s) for each ROI, which is transformed from the 3D image x time space to a 2D ROI signal x time space (Fig. 5.3 A). We determine the Pearson's cross-correlation coefficients between the 36 ROIs and then subsequently average the mean and median CCs across all images for the healthy and aberrant brain regions (Fig. 5.3 A). The local interictal activity connectivity differences were evaluated by comparing the mean and median cross-correlation coefficients derived from seizure prone regions and compared to CCs calculated from adjacent healthy regions.

Next to assess whether resection of aberrant seizure-prone brain tissue changes the local connectivity of nearby healthy regions, we repeat the analysis as outlined above using the fUSI interictal signal acquired from the healthy regions. We compare the CCs of the same healthy regions pre- and post-resection of the aberrant brain tissue. The difference in the regional local connectivity is evaluated by comparing the mean and median CCs using ANOVA and post-hoc Students t-test analysis with multiple comparison correction.

5.5.7 Effects of PNS on CBV and local connectivity

We derive statistical parametric maps to characterize the spatial and temporal changes to interictal brain activity due to a non-invasive PNS of the peripheral lower limb. The SPMs provide visualization of the regions with significant ($p < 0.05$, with FDR correction) cerebral blood volume changes caused by PNS. We compare fUSI interictal signal acquired during stimulation ON trials to the stimulation OFF trials. Note that to account for potential washout effect – uncertainty in how long it takes for the signal to return to baseline, we use only the last 20 s of the stimulation OFF trials signal preceding each stimulation ON trial. The SPMs are generated based on a pixelwise Student's *t*-test (two-sided with false discovery rate correction) comparison between the two fUSI image groups. This results in a p-value for each pixel in the fUSI image space that reflects the level of activation significance caused by PNS for the pixel. To assess the temporal evolution of the CBV changes in the activated brain regions, we generate ERA time course curves as a percentage change with respect to the stimulation OFF reference activity across all trials. We derive the combined stimulation effect (pseudo-global) across all activated pixels above a threshold (z-score > 0.6). The pseudo-global ERA waveform is determined as the mean %pD signal change across the SPM activated pixels with respect to the reference activity during stimulation OFF trials.

Next, we investigate how a common PNS protocol affects local brain network connectivity from continuous fUSI interictal activity recorded simultaneously with stimulation. We implemented a dynamic local activity connectivity analysis scheme to evaluate the evolution of local connectivity over time – measured as changes in the mean and median CCs as a function of time. We time-aligned the fUSI signal acquired during baseline, the stimulation OFF (3 trials, 3 min long) and the stimulation ON (3 trials, 6 min long) periods into a 3D (image-space x time) matrix (Fig. 5.4 B). Note the fUSI signal utilized for this analysis were acquired from aberrant seizure brain regions before surgical resection. Following a similar approach as outlined above we discretized the image space into equal 6 x 6 ROIs and transformed the matrix into a 2D space consisting of each ROI's mean pD intensity signal across time. Then employing a sliding window consisting of 180 s long data, with 10 s steps, we derived the Pearson's cross-correlation coefficient for each section of data, at each step (Fig. 5.4 B). We begin with the baseline data and progressively assess the connectivity through the concatenated baseline and stimulation OFF and ON trials signals.

Appendix

6.1 Data and software availability

The datasets generated and analyzed during this dissertation are available from the author upon reasonable request. Additionally, the algorithms and software utilized to analyze the datasets will be made available via a link to a GitHub repository.

Bibliography

1. Macé, E. *et al.* Functional ultrasound imaging of the brain. *Nat Methods* **8**, 662–664 (2011).

2. Mace, E. *et al.* Functional ultrasound imaging of the brain: theory and basic principles. *IEEE Trans Ultrason Ferroelectr Freq Control* **60**, 492–506 (2013).

3. Tanter, M. & Fink, M. Ultrafast imaging in biomedical ultrasound. *IEEE Trans Ultrason Ferroelectr Freq Control* **61**, 102–119 (2014).

4. Vertes, R. P. & Allen, T. *Electrophysiological recording techniques*. vol. 192 (Springer Nature, 2022).

5. Aminoff, M. J. Electroencephalography: general principles and clinical applications. *Aminoff's Electrodiagnosis in Clinical Neurology; Saunders, WB, Ed.; Elsevier BV: Amsterdam, The Netherlands* 37–84 (2012).

6. Kim, S.-M., Kim, S. H., Seo, D.-W. & Lee, K.-W. Intraoperative neurophysiologic monitoring: basic principles and recent update. *J Korean Med Sci* **28**, 1261–1269 (2013).

7. Bronzino, J. D. & Peterson, D. R. Principles of electroencephalography. in *Biomedical Engineering Fundamentals* 445–456 (CRC press, 2006).

8. Niedermeyer, E. & da Silva, F. H. L. *Electroencephalography: basic principles, clinical applications, and related fields*. (Lippincott Williams & Wilkins, 2005).

9. Ritaccio, A. L., Brunner, P. & Schalk, G. Electrical stimulation mapping of the brain: basic principles and emerging alternatives. *J Clin Neurophysiol* **35**, 86 (2018).

10. Yang, T., Hakimian, S. & Schwartz, T. H. Intraoperative ElectroCorticoGraphy (ECog): indications, techniques, and utility in epilepsy surgery. *Epileptic Disorders* **16**, 271–279 (2014).

11. Grienberger, C. & Konnerth, A. Imaging calcium in neurons. *Neuron* **73**, 862–885 (2012).

12. Gobel, W. & Helmchen, F. In vivo calcium imaging of neural network function. *Physiology* **22**, 358–365 (2007).

13. Gore, J. C. & others. Principles and practice of functional MRI of the human brain. *J Clin Invest* **112**, 4–9 (2003).

14. Logothetis, N. K. What we can do and what we cannot do with fMRI. *Nature* **453**, 869–878 (2008).

15. León-Carrión, J. & León-Dom\'\inguez, U. Functional near-infrared spectroscopy (fNIRS): principles and neuroscientific applications. *Neuroimaging methods* 48–74 (2012).

16. Zanzonico, P. Positron emission tomography: a review of basic principles, scanner design and performance, and current systems. in *Seminars in nuclear medicine* vol. 34 87–111 (2004).

17. Raichle, M. E. Positron emission tomography. *Annu Rev Neurosci* **6**, 249–267 (1983).

18. Beard, P. Biomedical photoacoustic imaging. *Interface Focus* **1**, 602–631 (2011).

19. Wang, L. V. *Photoacoustic imaging and spectroscopy*. (CRC press, 2017).

20. Deffieux, T., Demene, C., Pernot, M. & Tanter, M. Functional ultrasound neuroimaging: a review of the preclinical and clinical state of the art. *Curr Opin Neurobiol* **50**, 128–135 (2018).

21. Song, P. *et al.* Functional ultrasound imaging of spinal cord hemodynamic responses to epidural electrical stimulation: a feasibility study. *Front Neurol* **10**, 279 (2019).

22. Sieu, L.-A. *et al.* EEG and functional ultrasound imaging in mobile rats. *Nat Methods* **12**, 831–834 (2015).

23. Bercoff, J. *et al.* Ultrafast compound Doppler imaging: Providing full blood flow characterization. *IEEE Trans Ultrason Ferroelectr Freq Control* **58**, 134–147 (2011).

24. Baranger, J. *et al.* Adaptive spatiotemporal SVD clutter filtering for ultrafast Doppler imaging using similarity of spatial singular vectors. *IEEE Trans Med Imaging* **37**, 1574–1586 (2018).

25. Klema, V. & Laub, A. The singular value decomposition: Its computation and some applications. *IEEE Trans Automat Contr* **25**, 164–176 (1980).

26. Osmanski, B.-F., Pezet, S., Ricobaraza, A., Lenkei, Z. & Tanter, M. Functional ultrasound imaging of intrinsic connectivity in the living rat brain with high spatiotemporal resolution. *Nat Commun* **5**, 1–14 (2014).

27. Dizeux, A. *et al.* Functional ultrasound imaging of the brain reveals propagation of task-related brain activity in behaving primates. *Nat Commun* **10**, 1–9 (2019).

28. Norman, S. L. *et al.* Single-trial decoding of movement intentions using functional ultrasound neuroimaging. *Neuron* **109**, 1554–1566 (2021).

29. Soloukey, S. *et al.* Functional ultrasound (fUS) during awake brain surgery: the clinical potential of intra-operative functional and vascular brain mapping. *Front Neurosci* **13**, 1384 (2020).

30. Imbault, M., Chauvet, D., Gennisson, J.-L., Capelle, L. & Tanter, M. Intraoperative functional ultrasound imaging of human brain activity. *Sci Rep* **7**, 1–7 (2017).

31. Demene, C. *et al.* Functional ultrasound imaging of brain activity in human newborns. *Sci Transl Med* **9**, eaah6756 (2017).

32. Baranger, J. *et al.* Bedside functional monitoring of the dynamic brain connectivity in human neonates. *Nat Commun* **12**, 1080 (2021).

33. Song, P. *et al.* Functional ultrasound imaging of spinal cord hemodynamic responses to epidural electrical stimulation: a feasibility study. *Front Neurol* **10**, 279 (2019).

34. Ranasinghe, K. G. *et al.* Reduced synchrony in alpha oscillations during life predicts postmortem neurofibrillary tangle density in early-onset and atypical Alzheimer's disease. *Alzheimer's & Dementia* **17**, 2009–2019 (2021).

35. Tu, M.-C., Chung, H.-W., Hsu, Y.-H., Yang, J.-J. & Wu, W.-C. Stage-Dependent Cerebral Blood Flow and Leukoaraiosis Couplings in Subcortical Ischemic Vascular Disease and Alzheimer's Disease. *Journal of Alzheimer's Disease* **86**, 729–739 (2022).

36. Dougherty, D. D. *et al.* Acute deep brain stimulation changes in regional cerebral blood flow in obsessive-compulsive disorder. *J Neurosurg* **125**, 1087–1093 (2016).

37. Laxton, A. W. *et al.* A phase I trial of deep brain stimulation of memory circuits in Alzheimer's disease. *Ann Neurol* **68**, 521–534 (2010).

38. Moraes, F. V., Ferreira, S. de F. B., de Souza, Â. M. C. & Diniz, D. S. Neuromodulation using transcranial magnetic stimulation (TMS): effective cognitive rehabilitation after stroke. *J Bras Neurocirurg* **27**, 149–154 (2016).

39. Bashir, S., Mizrahi, I., Weaver, K., Fregni, F. & Pascual-Leone, A. Assessment and modulation of neural plasticity in rehabilitation with transcranial magnetic stimulation. *PM&R* **2**, S253–S268 (2010).

40. Cortes, M., Black-Schaffer, R. M. & Edwards, D. J. Transcranial magnetic stimulation as an investigative tool for motor dysfunction and recovery in stroke: an overview for neurorehabilitation clinicians. *Neuromodulation: Technology at the Neural Interface* **15**, 316–325 (2012).

41. Iannone, A., Cruz, A. P. de M., Brasil-Neto, J. P. & Boechat-Barros, R. Transcranial magnetic stimulation and transcranial direct current stimulation appear to be safe neuromodulatory techniques useful in the treatment of anxiety disorders and other neuropsychiatric disorders. *Arq Neuropsiquiatr* **74**, 829–835 (2016).

42. Dionisio, A., Duarte, I. C., Patricio, M. & Castelo-Branco, M. The use of repetitive transcranial magnetic stimulation for stroke rehabilitation: a systematic review. *Journal of stroke and cerebrovascular diseases* **27**, 1–31 (2018).

43. Gouveia, F. V. *et al.* Treating post-traumatic stress disorder with neuromodulation therapies: transcranial magnetic stimulation, transcranial direct current stimulation, and deep brain stimulation. *Neurotherapeutics* **17**, 1747–1756 (2020).

44. Boon, P., De Cock, E., Mertens, A. & Trinka, E. Neurostimulation for drug-resistant epilepsy: a systematic review of clinical evidence for efficacy, safety, contraindications and predictors for response. *Curr Opin Neurol* **31**, 198–210 (2018).

45. Rabut, C. *et al.* Pharmaco-fUS: Quantification of pharmacologically-induced dynamic changes in brain perfusion and connectivity by functional ultrasound imaging in awake mice. *Neuroimage* **222**, 117231 (2020).

46. Berman, R. M. *et al.* Antidepressant effects of ketamine in depressed patients. *Biol Psychiatry* **47**, 351–354 (2000).

47. Schwartz, J., Murrough, J. W. & Iosifescu, D. V. Ketamine for treatment-resistant depression: recent developments and clinical applications. *BMJ Ment Health* **19**, 35–38 (2016).

48. Murrough, J. W. *et al.* Rapid and longer-term antidepressant effects of repeated ketamine infusions in treatment-resistant major depression. *Biol Psychiatry* **74**, 250–256 (2013).

49. Wilkinson, S. T. *et al.* The effect of a single dose of intravenous ketamine on suicidal ideation: a systematic review and individual participant data meta-analysis. *American journal of psychiatry* **175**, 150–158 (2018).

50. Newcomer, J. W. *et al.* Ketamine-induced NMDA receptor hypofunction as a model of memory impairment and psychosis. *Neuropsychopharmacology* **20**, 106–118 (1999).

51. Stone, J. M. *et al.* Relationship between ketamine-induced psychotic symptoms and NMDA receptor occupancy—a [123 I] CNS-1261 SPET study. *Psychopharmacology (Berl)* **197**, 401–408 (2008).

52. Jiang, W. *et al.* Subthreshold repetitive transcranial magnetic stimulation suppresses ketamine-induced poly population spikes in rat sensorimotor cortex. *Front Neurosci* **16**, 998704 (2022).

53. Frohlich, J. & Van Horn, J. D. Reviewing the ketamine model for schizophrenia. *Journal of psychopharmacology* **28**, 287–302 (2014).

54. Sleigh, J., Harvey, M., Voss, L. & Denny, B. Ketamine–More mechanisms of action than just NMDA blockade. *Trends in anaesthesia and critical care* **4**, 76–81 (2014).

55. Driesen, N. R. *et al.* Relationship of resting brain hyperconnectivity and schizophrenia-like symptoms produced by the NMDA receptor antagonist ketamine in humans. *Mol Psychiatry* **18**, 1199–1204 (2013).

56. Niesters, M. *et al.* Effect of subanesthetic ketamine on intrinsic functional brain connectivity: a placebo-controlled functional magnetic resonance imaging study in healthy male volunteers. *The Journal of the American Society of Anesthesiologists* **117**, 868–877 (2012).

57. Uhlhaas, P. J. & Singer, W. Abnormal neural oscillations and synchrony in schizophrenia. *Nat Rev Neurosci* **11**, 100–113 (2010).

58. Barr, M. S. *et al.* Impaired theta-gamma coupling during working memory performance in schizophrenia. *Schizophr Res* **189**, 104–110 (2017).

59. Jafari, Z., Kolb, B. E. & Mohajerani, M. H. Neural oscillations and brain stimulation in Alzheimer's disease. *Prog Neurobiol* **194**, 101878 (2020).

60. Gonzalez-Burgos, G. & Lewis, D. A. NMDA receptor hypofunction, parvalbumin-positive neurons, and cortical gamma oscillations in schizophrenia. *Schizophr Bull* **38**, 950–957 (2012).

61. Gu, Z., Alexander, G. M., Dudek, S. M. & Yakel, J. L. Hippocampus and entorhinal cortex recruit cholinergic and NMDA receptors separately to generate hippocampal theta oscillations. *Cell Rep* **21**, 3585–3595 (2017).

62. Collingridge, G. The role of NMDA receptors in learning and memory. *Nature* **330**, 604–605 (1987).

63. Spangler, E. L. *et al.* NMDA receptor channel antagonism by dizocilpine (MK-801) impairs performance of rats in aversively motivated complex maze tasks. *Pharmacol Biochem Behav* **40**, 949–958 (1991).

64. Korotkova, T., Fuchs, E. C., Ponomarenko, A., von Engelhardt, J. & Monyer, H. NMDA receptor ablation on parvalbumin-positive interneurons impairs hippocampal synchrony, spatial representations, and working memory. *Neuron* **68**, 557–569 (2010).

65. Saunders, J. A., Gandal, M. J. & Siegel, S. J. NMDA antagonists recreate signal-to-noise ratio and timing perturbations present in schizophrenia. *Neurobiol Dis* **46**, 93–100 (2012).

66. Billingslea, E. N. *et al.* Parvalbumin cell ablation of NMDA-R1 causes increased resting network excitability with associated social and self-care deficits. *Neuropsychopharmacology* **39**, 1603–1613 (2014).

67. Fuhrmann, F. *et al.* Locomotion, theta oscillations, and the speed-correlated firing of hippocampal neurons are controlled by a medial septal glutamatergic circuit. *Neuron* **86**, 1253–1264 (2015).

68. Leão, R. N., Targino, Z. H., Colom, L. V & Fisahn, A. Interconnection and synchronization of neuronal populations in the mouse medial septum/diagonal band of Broca. *J Neurophysiol* **113**, 971–980 (2015).

69. Takeuchi, Y. *et al.* The medial septum as a potential target for treating brain disorders associated with oscillopathies. *Front Neural Circuits* **15**, 701080 (2021).

70. Lee, D. J. *et al.* Medial septal nucleus theta frequency deep brain stimulation improves spatial working memory after traumatic brain injury. *J Neurotrauma* **30**, 131–139 (2013).

71. Lee, D. J. *et al.* Septohippocampal neuromodulation improves cognition after traumatic brain injury. *J Neurotrauma* **32**, 1822–1832 (2015).

72. Lee, D. J. *et al.* Stimulation of the medial septum improves performance in spatial learning following pilocarpine-induced status epilepticus. *Epilepsy Res* **130**, 53–63 (2017).

73. Cole, E. R. *et al.* Evidence supporting deep brain stimulation of the medial septum in the treatment of temporal lobe epilepsy. *Epilepsia* **63**, 2192–2213 (2022).

74. Zepeda, N. C. *et al.* Frequency-specific medial septal nucleus deep brain stimulation improves spatial memory in MK-801-treated male rats. *Neurobiol Dis* **170**, 105756 (2022).

75. Liu, X. S. *Statistical power analysis for the social and behavioral sciences: Basic and advanced techniques*. (Routledge, 2013).

76. Balu, D. T. The NMDA receptor and schizophrenia: from pathophysiology to treatment. *Adv Pharmacol* **76**, 351–382 (2016).

77. Farber, N. B. The NMDA receptor hypofunction model of psychosis. *Ann N Y Acad Sci* **1003**, 119–130 (2003).

78. MacDonald, S. W. S., Nyberg, L. & Bäckman, L. Intra-individual variability in behavior: links to brain structure, neurotransmission and neuronal activity. *Trends Neurosci* **29**, 474–480 (2006).

79. Gur, R. E. & Gur, R. C. Functional magnetic resonance imaging in schizophrenia. *Dialogues Clin Neurosci* (2022).

80. Bedford, N. J., Surguladze, S., Giampietro, V., Brammer, M. J. & David, A. S. Self-evaluation in schizophrenia: an fMRI study with implications for the understanding of insight. *BMC Psychiatry* **12**, 1–14 (2012).

81. Moghaddam, B. & Javitt, D. From revolution to evolution: the glutamate hypothesis of schizophrenia and its implication for treatment. *Neuropsychopharmacology* **37**, 4–15 (2012).

82. Stark, E. *et al.* Inhibition-induced theta resonance in cortical circuits. *Neuron* **80**, 1263–1276 (2013).

83. Lin, C.-H., Huang, Y.-J., Lin, C.-J., Lane, H.-Y. & E Tsai, G. NMDA neurotransmission dysfunction in mild cognitive impairment and Alzheimer’s disease. *Curr Pharm Des* **20**, 5169–5179 (2014).

84. Ward, K. R. *et al.* Src deficient mice demonstrate behavioral and electrophysiological alterations relevant to psychiatric and developmental disease. *Prog Neuropsychopharmacol Biol Psychiatry* **93**, 84–92 (2019).

85. Boido, D. *et al.* Mesoscopic and microscopic imaging of sensory responses in the same animal. *Nat Commun* **10**, 1110 (2019).

86. Aydin, A.-K. *et al.* Transfer functions linking neural calcium to single voxel functional ultrasound signal. *Nat Commun* **11**, 2954 (2020).

87. Nunez-Elizalde, A. O. *et al.* Neural correlates of blood flow measured by ultrasound. *Neuron* **110**, 1631–1640 (2022).

88. Buzsáki, G. & Schomburg, E. W. What does gamma coherence tell us about inter-regional neural communication? *Nat Neurosci* **18**, 484–489 (2015).

89. Mar\’\in, O. Interneuron dysfunction in psychiatric disorders. *Nat Rev Neurosci* **13**, 107–120 (2012).

90. Homayoun, H. & Moghaddam, B. NMDA receptor hypofunction produces opposite effects on prefrontal cortex interneurons and pyramidal neurons. *Journal of Neuroscience* **27**, 11496–11500 (2007).

91. Cohen, S. M., Tsien, R. W., Goff, D. C. & Halassa, M. M. The impact of NMDA receptor hypofunction on GABAergic neurons in the pathophysiology of schizophrenia. *Schizophr Res* **167**, 98–107 (2015).

92. Anenberg, E., Chan, A. W., Xie, Y., LeDue, J. M. & Murphy, T. H. Optogenetic stimulation of GABA neurons can decrease local neuronal activity while increasing cortical blood flow. *Journal of Cerebral Blood Flow & Metabolism* **35**, 1579–1586 (2015).

93. Espinoza, R. T. & Kellner, C. H. Electroconvulsive therapy. *New England Journal of Medicine* **386**, 667–672 (2022).

94. Singh, A. & Kar, S. K. How electroconvulsive therapy works?: understanding the neurobiological mechanisms. *Clinical Psychopharmacology and Neuroscience* **15**, 210 (2017).

95. Andrade, C., Arumugham, S. S. & Thirthalli, J. Adverse effects of electroconvulsive therapy. *Psychiatric Clinics* **39**, 513–530 (2016).

96. Gersner, R., Kravetz, E., Feil, J., Pell, G. & Zangen, A. Long-term effects of repetitive transcranial magnetic stimulation on markers for neuroplasticity: differential outcomes in anesthetized and awake animals. *Journal of Neuroscience* **31**, 7521–7526 (2011).

97. Xu, T. *et al.* Interindividual variability of functional connectivity in awake and anesthetized rhesus macaque monkeys. *Biol Psychiatry Cogn Neurosci Neuroimaging* **4**, 543–553 (2019).

98. Bertolo, A. *et al.* Whole-brain 3D activation and functional connectivity mapping in mice using transcranial functional ultrasound imaging. *JoVE (Journal of Visualized Experiments)* e62267 (2021).

99. Rabut, C. *et al.* 4D functional ultrasound imaging of whole-brain activity in rodents. *Nat Methods* **16**, 994–997 (2019).

100. Grubbs, F. E. Procedures for detecting outlying observations in samples. *Technometrics* **11**, 1–21 (1969).

101. Stefansky, W. Rejecting outliers in factorial designs. *Technometrics* **14**, 469–479 (1972).

102. Paknahad, J. *et al.* Modeling ON cone bipolar cells for electrical stimulation. in *2021 43rd Annual International Conference of the IEEE Engineering in Medicine & Biology Society (EMBC)* 6547–6550 (2021).

103. Wegener, N. *et al.* Evaluation of brain pharmacokinetics of (+) MK-801 in relation to behaviour. *Neurosci Lett* **503**, 68–72 (2011).

104. Wang, Q. *et al.* The Allen Mouse Brain Common Coordinate Framework: A 3D Reference Atlas. *Cell* **181**, 936-953.e20 (2020).

105. Ledoux, L. A. F., Brands, P. J. & Hoeks, A. P. G. Reduction of the clutter component in Doppler ultrasound signals based on singular value decomposition: A simulation study. *Ultrason Imaging* **19**, 1–18 (1997).

106. Stringer, C. & Pachitariu, M. Computational processing of neural recordings from calcium imaging data. *Curr Opin Neurobiol* **55**, 22–31 (2019).

107. Friedrich, J., Giovannucci, A. & Pnevmatikakis, E. A. Online analysis of microendoscopic 1-photon calcium imaging data streams. *PLoS Comput Biol* **17**, e1008565 (2021).

108. Pnevmatikakis, E. A. & Giovannucci, A. NoRMCorre: An online algorithm for piecewise rigid motion correction of calcium imaging data. *J Neurosci Methods* **291**, 83–94 (2017).

109. Cramer, G. D. & Darby, S. A. Clinical anatomy of the spine, spinal cord, and ANS-e-book. (2017).

110. Nielsen, J. B. Sensorimotor integration at spinal level as a basis for muscle coordination during voluntary movement in humans. *J Appl Physiol* **96**, 1961–1967 (2004).

111. Grillner, S. Control of locomotion in bipeds, tetrapods, and fish. *Compr Physiol* 1179–1236 (2011).

112. Harkema, S. *et al.* Effect of epidural stimulation of the lumbosacral spinal cord on voluntary movement, standing, and assisted stepping after motor complete paraplegia: a case study. *The Lancet* **377**, 1938–1947 (2011).

113. Kiehn, O. Locomotor circuits in the mammalian spinal cord. *Annu. Rev. Neurosci.* **29**, 279–306 (2006).

114. Ahuja, C. S. *et al.* Traumatic spinal cord injury. *Nat Rev Dis Primers* **3**, 1–21 (2017).

115. Anderson, K. D., Borisoff, J. F., Johnson, R. D., Stiens, S. A. & Elliott, S. L. The impact of spinal cord injury on sexual function: concerns of the general population. *Spinal Cord* **45**, 328–337 (2007).

116. Anderson, K. D. Targeting recovery: priorities of the spinal cord-injured population. *J Neurotrauma* **21**, 1371–1383 (2004).

117. McDonald, J. W. & Sadowsky, C. Spinal-cord injury. *The Lancet* **359**, 417–425 (2002).

118. Watrous, J. R. *et al.* Low back pain, mental health symptoms, and quality of life among injured service members. *Health Psychology* **39**, 549 (2020).

119. Savic, G., Frankel, H. L., Jamous, M. A., Soni, B. M. & Charlifue, S. Long-term bladder and bowel management after spinal cord injury: a 20-year longitudinal study. *Spinal Cord* **56**, 575–581 (2018).

120. Sadowsky, C. L. & Margherita, A. The cost of spinal cord injury care. *Spine (Phila Pa 1976)* **13**, 593–606 (1999).

121. Yoshizawa, T., Nose, T., Moore, G. J. & Sillerud, L. O. Functional magnetic resonance imaging of motor activation in the human cervical spinal cord. *Neuroimage* **4**, 174–182 (1996).

122. Stroman, P. W., Nance, P. W. & Ryner, L. N. BOLD MRI of the human cervical spinal cord at 3 tesla. *Magnetic Resonance in Medicine: An Official Journal of the International Society for Magnetic Resonance in Medicine* **42**, 571–576 (1999).

123. San Emeterio Nateras, O. *et al.* Intrinsic resting-state functional connectivity in the human spinal cord at 3.0 T. *Radiology* **279**, 262–268 (2016).

124. Liu, X. *et al.* Organization of the intrinsic functional network in the cervical spinal cord: A resting state functional MRI study. *Neuroscience* **336**, 30–38 (2016).

125. Chen, L. M., Mishra, A., Yang, P.-F., Wang, F. & Gore, J. C. Injury alters intrinsic functional connectivity within the primate spinal cord. *Proceedings of the National Academy of Sciences* **112**, 5991–5996 (2015).

126. Kong, Y. *et al.* Intrinsically organized resting state networks in the human spinal cord. *Proceedings of the National Academy of Sciences* **111**, 18067–18072 (2014).

127. Kinany, N., Pirondini, E., Micera, S. & Van De Ville, D. Dynamic functional connectivity of resting-state spinal cord fMRI reveals fine-grained intrinsic architecture. *Neuron* **108**, 424–435 (2020).

128. Barry, R. L., Smith, S. A., Dula, A. N. & Gore, J. C. Resting state functional connectivity in the human spinal cord. *Elife* **3**, e02812 (2014).

129. Wu, T.-L. *et al.* Intrinsic functional architecture of the non-human primate spinal cord derived from fMRI and electrophysiology. *Nat Commun* **10**, 1–10 (2019).

130. Giove, F. *et al.* Issues about the fMRI of the human spinal cord. *Magn Reson Imaging* **22**, 1505–1516 (2004).

131. Eippert, F., Kong, Y., Jenkinson, M., Tracey, I. & Brooks, J. C. W. Denoising spinal cord fMRI data: Approaches to acquisition and analysis. *Neuroimage* **154**, 255–266 (2017).

132. Stroman, P. W. *et al.* The current state-of-the-art of spinal cord imaging: methods. *Neuroimage* **84**, 1070–1081 (2014).

133. Vahdat, S. *et al.* Resting-state brain and spinal cord networks in humans are functionally integrated. *PLoS Biol* **18**, e3000789 (2020).

134. Jacques, S. L. Optical properties of biological tissues: a review. *Phys Med Biol* **58**, R37 (2013).

135. Costantini, I., Cicchi, R., Silvestri, L., Vanzi, F. & Pavone, F. S. In-vivo and ex-vivo optical clearing methods for biological tissues. *Biomed Opt Express* **10**, 5251–5267 (2019).

136. Tang, S. *et al.* Changes in spinal cord hemodynamics reflect modulation of spinal network with different parameters of epidural stimulation. *Neuroimage* **221**, 117183 (2020).

137. Claron, J. *et al.* Large-scale functional ultrasound imaging of the spinal cord reveals in-depth spatiotemporal responses of spinal nociceptive circuits in both normal and inflammatory states. *Pain* **162**, 1047 (2021).

138. Soloukey, S. *et al.* Towards high-resolution functional ultrasound (fUS) imaging of the murine spinal cord. in *2019 IEEE International Ultrasonics Symposium (IUS)* 2259–2262 (2019).

139. Koetsier, E. *et al.* Dorsal root ganglion stimulation in experimental painful diabetic polyneuropathy: delayed wash-out of pain relief after low-frequency (1Hz) stimulation. *Neuromodulation: Technology at the Neural Interface* **23**, 177–184 (2020).

140. Moro, E. *et al.* The impact on Parkinson's disease of electrical parameter settings in STN stimulation. *Neurology* **59**, 706–713 (2002).

141. Nenadic, Z. Classwise principal component analysis. (2010).

142. Das, K., Osechinskiy, S. & Nenadic, Z. A classwise PCA-based recognition of neural data for brain-computer interfaces. in *2007 29th Annual International Conference of the IEEE Engineering in Medicine and Biology Society* 6519–6522 (2007).

143. Bimbard, C. *et al.* Multi-scale mapping along the auditory hierarchy using high-resolution functional UltraSound in the awake ferret. *Elife* **7**, e35028 (2018).

144. Backes, W. H., Mess, W. H. & Wilmink, J. T. Functional MR imaging of the cervical spinal cord by use of median nerve stimulation and fist clenching. *American journal of neuroradiology* **22**, 1854–1859 (2001).

145. Islam, H., Law, C. S. W., Weber, K. A., Mackey, S. C. & Glover, G. H. Dynamic per slice shimming for simultaneous brain and spinal cord fMRI. *Magn Reson Med* **81**, 825–838 (2019).

146. Smith, S. D. & Kornelsen, J. Emotion-dependent responses in spinal cord neurons: a spinal fMRI study. *Neuroimage* **58**, 269–274 (2011).

147. Stroman, P. W. & Ryner, L. N. Functional MRI of motor and sensory activation in the human spinal cord. *Magn Reson Imaging* **19**, 27–32 (2001).

148. Vahdat, S. *et al.* Simultaneous brain–cervical cord fMRI reveals intrinsic spinal cord plasticity during motor sequence learning. *PLoS Biol* **13**, e1002186 (2015).

149. Hartvigsen, J. *et al.* What low back pain is and why we need to pay attention. *The Lancet* **391**, 2356–2367 (2018).

150. Carter, M. L. Spinal cord stimulation in chronic pain: a review of the evidence. *Anaesth Intensive Care* **32**, 11–21 (2004).

151. Deyo, R. A., Von Korff, M. & Duhrkoop, D. Opioids for low back pain. *Bmj* **350**, (2015).

152. Staal, J. B., de Bie, R., de Vet, H. C. W., Hildebrandt, J. & Nelemans, P. Injection therapy for subacute and chronic low-back pain. *Cochrane Database of Systematic Reviews* (2008).

153. Center, C. A. & Manchikanti, L. Epidural injections for lumbar radiculopathy and spinal stenosis: a comparative systematic review and meta-analysis. *Pain Physician* **19**, E365–E410 (2016).

154. Shealy, C. N. Percutaneous radiofrequency denervation of spinal facets: treatment for chronic back pain and sciatica. *J Neurosurg* **43**, 448–451 (1975).

155. Yi, P. & Pryzbylkowski, P. Opioid induced hyperalgesia. *Pain Medicine* **16**, S32–S36 (2015).

156. Guan, Y., Bradley, K., Parker, J. L., Krames, E. S. & Linderoth, B. Spinal cord stimulation: mechanisms of action. in *Neuromodulation* 161–178 (Elsevier, 2018).

157. Jensen, M. P. & Brownstone, R. M. Mechanisms of spinal cord stimulation for the treatment of pain: Still in the dark after 50 years. *European Journal of Pain* **23**, 652–659 (2019).

158. Soares, S. *et al.* Ultrafast Doppler imaging and Ultrasound Localization Microscopy reveal vascular rearrangement's complexity in chronic spinal lesion. in *FENS* (2022).

159. Tiran, E. *et al.* Transcranial functional ultrasound imaging in freely moving awake mice and anesthetized young rats without contrast agent. *Ultrasound Med Biol* **43**, 1679–1689 (2017).

160. Demené, C. *et al.* Transcranial ultrafast ultrasound localization microscopy of brain vasculature in patients. *Nat Biomed Eng* **5**, 219–228 (2021).

161. Zileli, M., Dalbayrak, S. & Benzel, E. C. Iatrogenic spine destabilization. in *Benzel's Spine Surgery, 2-Volume Set* 362–371 (Elsevier, 2017).

162. Foroosh, H., Zerubia, J. B. & Berthod, M. Extension of phase correlation to subpixel registration. *IEEE transactions on image processing* **11**, 188–200 (2002).

163. Demené, C. *et al.* Spatiotemporal clutter filtering of ultrafast ultrasound data highly increases Doppler and fUltrasound sensitivity. *IEEE Trans Med Imaging* **34**, 2271–2285 (2015).

164. Chen, K., Kogan, J. F. & Fontanini, A. Spatially distributed representation of taste quality in the gustatory insular cortex of behaving mice. *Current Biology* **31**, 247–256 (2021).

165. Xanthopoulos, P., Pardalos, P. M. & Trafalis, T. B. Linear discriminant analysis. in *Robust data mining* 27–33 (Springer, 2013).

166. Das, K. & Nenadic, Z. Approximate information discriminant analysis: A computationally simple heteroscedastic feature extraction technique. *Pattern Recognit* **41**, 1548–1557 (2008).

167. Das, K. & Nenadic, Z. An efficient discriminant-based solution for small sample size problem. *Pattern Recognit* **42**, 857–866 (2009).

168. Steuer, I. & Guertin, P. A. Central pattern generators in the brainstem and spinal cord: an overview of basic principles, similarities and differences. *Rev Neurosci* **30**, 107–164 (2019).

169. Frigon, A. Central pattern generators of the mammalian spinal cord. *The Neuroscientist* **18**, 56–69 (2012).

170. Roy, H. A. & Green, A. L. The central autonomic network and regulation of bladder function. *Front Neurosci* **13**, 535 (2019).

171. Powers, J. M., Ioachim, G. & Stroman, P. W. Ten key insights into the use of spinal cord fMRI. *Brain Sci* **8**, 173 (2018).

172. Fowler, C. J., Griffiths, D. & De Groat, W. C. The neural control of micturition. *Nat Rev Neurosci* **9**, 453–466 (2008).

173. Demené, C. *et al.* 4D microvascular imaging based on ultrafast Doppler tomography. *Neuroimage* **127**, 472–483 (2016).

174. Osmanski, B.-F. *et al.* Functional ultrasound imaging reveals different odor-evoked patterns of vascular activity in the main olfactory bulb and the anterior piriform cortex. *Neuroimage* **95**, 176–184 (2014).

175. Griggs, W. S. *et al.* Decoding Motor Plans Using a Closed-Loop Ultrasonic Brain-Machine Interface. *bioRxiv* 2011–2022 (2022).

176. Agyeman, K. A. *et al.* Functional ultrasound imaging of the human spinal cord. *bioRxiv* 2022–2028 (2022).

177. Ginsberg, D. A. *et al.* The AUA/SUFU guideline on adult neurogenic lower urinary tract dysfunction: diagnosis and evaluation. *J Urol* **206**, 1097–1105 (2021).

178. Gad, P. N. *et al.* Initiation of bladder voiding with epidural stimulation in paralyzed, step trained rats. *PLoS One* **9**, e108184 (2014).

179. Abud, E. M., Ichiyama, R. M., Havton, L. A. & Chang, H. H. Spinal stimulation of the upper lumbar spinal cord modulates urethral sphincter activity in rats after spinal cord injury. *American Journal of Physiology-Renal Physiology* **308**, F1032–F1040 (2015).

180. Gad, P. N., Kreydin, E., Zhong, H., Latack, K. & Edgerton, V. R. Non-invasive neuromodulation of spinal cord restores lower urinary tract function after paralysis. *Front Neurosci* **12**, 432 (2018).

181. Kreydin, E. *et al.* Transcutaneous electrical spinal cord neuromodulator (TESCoN) improves symptoms of overactive bladder. *Front Syst Neurosci* **14**, 1 (2020).

182. Rabut, C. *et al.* A window to the brain: ultrasound imaging of human neural activity through a permanent acoustic window. *bioRxiv* 2023–2026 (2023).

183. Errico, C. *et al.* Transcranial functional ultrasound imaging of the brain using microbubble-enhanced ultrasensitive Doppler. *Neuroimage* **124**, 752–761 (2016).

184. Wein, A. J. & Moy, M. L. Voiding function and dysfunction; urinary incontinence. in *Penn clinical manual of urology* 341–478 (Elsevier, 2007).

185. Hearst, M. A., Dumais, S. T., Osuna, E., Platt, J. & Scholkopf, B. Support vector machines. *IEEE Intelligent Systems and their applications* **13**, 18–28 (1998).

186. Steinwart, I. & Christmann, A. *Support vector machines.* (Springer Science & Business Media, 2008).

187. Thijs, R. D., Surges, R., O'Brien, T. J. & Sander, J. W. Epilepsy in adults. *The Lancet* **393**, 689–701 (2019).

188. Helbig, I., Scheffer, I. E. & Berkovic, S. F. 24 - Genetic Epilepsies. in *Molecular Neurology* (ed. Waxman, S. G.) 371–383 (Academic Press, 2007). doi:https://doi.org/10.1016/B978-012369509-3.50026-3.

189. Mohammadzadeh, P. & Nazarbaghi, S. The prevalence of drug-resistant-epilepsy and its associated factors in patients with epilepsy. *Clin Neurol Neurosurg* **213**, 107086 (2022).

190. Brodie, M. J., Barry, S. J. E., Bamagous, G. A., Norrie, J. D. & Kwan, P. Patterns of treatment response in newly diagnosed epilepsy. *Neurology* **78**, 1548–1554 (2012).

191. Cascino, G. D. Surgical treatment for epilepsy. *Epilepsy Res* **60**, 179–186 (2004).

192. Mathon, B. *et al.* Surgical treatment for mesial temporal lobe epilepsy associated with hippocampal sclerosis. *Rev Neurol (Paris)* **171**, 315–325 (2015).

193. Ryvlin, P., Rheims, S., Hirsch, L. J., Sokolov, A. & Jehi, L. Neuromodulation in epilepsy: state-of-the-art approved therapies. *Lancet Neurol* **20**, 1038–1047 (2021).

194. Fisher, R. *et al.* Electrical stimulation of the anterior nucleus of thalamus for treatment of refractory epilepsy. *Epilepsia* **51**, 899–908 (2010).

195. Ben-Menachem, E. Vagus-nerve stimulation for the treatment of epilepsy. *Lancet Neurol* **1**, 477–482 (2002).

196. Morrell, M. J. Responsive cortical stimulation for the treatment of medically intractable partial epilepsy. *Neurology* **77**, 1295–1304 (2011).

197. Fisher, R. S. *et al.* Automatic vagus nerve stimulation triggered by ictal tachycardia: clinical outcomes and device performance—the US E-37 trial. *Neuromodulation: Technology at the Neural Interface* **19**, 188–195 (2016).

198. Krahl, S. E., Clark, K. B., Smith, D. C. & Browning, R. A. Locus coeruleus lesions suppress the seizure-attenuating effects of vagus nerve stimulation. *Epilepsia* **39**, 709–714 (1998).

199. Raedt, R. *et al.* Increased hippocampal noradrenaline is a biomarker for efficacy of vagus nerve stimulation in a limbic seizure model. *J Neurochem* **117**, 461–469 (2011).

200. Jaseja, H. EEG-desynchronization as the major mechanism of anti-epileptic action of vagal nerve stimulation in patients with intractable seizures: clinical neurophysiological evidence. *Med Hypotheses* **74**, 855–856 (2010).

201. Nichols, J. A. *et al.* Vagus nerve stimulation modulates cortical synchrony and excitability through the activation of muscarinic receptors. *Neuroscience* **189**, 207–214 (2011).

202. Fraschini, M. *et al.* VNS induced desynchronization in gamma bands correlates with positive clinical outcome in temporal lobe pharmacoresistant epilepsy. *Neurosci Lett* **536**, 14–18 (2013).

203. Marrosu, F. *et al.* Correlation between GABAA receptor density and vagus nerve stimulation in individuals with drug-resistant partial epilepsy. *Epilepsy Res* **55**, 59–70 (2003).

204. Kwan, H. *et al.* Vagus nerve stimulation for treatment of inflammation: systematic review of animal models and clinical studies. *Bioelectron Med* **3**, 1–6 (2016).

205. Kokkinos, V., Sisterson, N. D., Wozny, T. A. & Richardson, R. M. Association of closed-loop brain stimulation neurophysiological features with seizure control among patients with focal epilepsy. *JAMA Neurol* **76**, 800–808 (2019).

206. Shi, L. *et al.* Favorable modulation in neurotransmitters: effects of chronic anterior thalamic nuclei stimulation observed in epileptic monkeys. *Exp Neurol* **265**, 94–101 (2015).

207. Yu, T. *et al.* High-frequency stimulation of anterior nucleus of thalamus desynchronizes epileptic network in humans. *Brain* **141**, 2631–2643 (2018).

208. Middlebrooks, E. H. *et al.* Functional activation patterns of deep brain stimulation of the anterior nucleus of the thalamus. *World Neurosurg* **136**, 357–363 (2020).

209. Handforth, A. *et al.* Vagus nerve stimulation therapy for partial-onset seizures: a randomized active-control trial. *Neurology* **51**, 48–55 (1998).

210. Severinsen, K. *et al.* Implanted Peroneal Nerve Stimulator Treatment for Drop Foot Caused by Central Nervous System Lesion: A Twelve-Month Follow-up of 21 Patients. *J Rehabil Med* **54**, (2022).

211. Kottink, A. I. R. *et al.* Therapeutic effect of an implantable peroneal nerve stimulator in subjects with chronic stroke and footdrop: a randomized controlled trial. *Phys Ther* **88**, 437–448 (2008).

212. Sheffler, L. R., Hennessey, M. T., Knutson, J. S. & Chae, J. Neuroprosthetic effect of peroneal nerve stimulation in multiple sclerosis: a preliminary study. *Arch Phys Med Rehabil* **90**, 362–365 (2009).

213. Lin, T., Gargya, A., Singh, H., Sivanesan, E. & Gulati, A. Mechanism of peripheral nerve stimulation in chronic pain. *Pain Medicine* **21**, S6–S12 (2020).

214. Hanyu-Deutmeyer, A. & Pritzlaff, S. G. Peripheral nerve stimulation for the 21st century: sural, superficial peroneal, and tibial nerves. *Pain Medicine* **21**, S64–S67 (2020).

215. Khaslavskaia, S., Ladouceur, M. & Sinkjaer, T. Increase in tibialis anterior motor cortex excitability following repetitive electrical stimulation of the common peroneal nerve. *Exp Brain Res* **145**, 309–315 (2002).

216. Knash, M. E., Kido, A., Gorassini, M., Chan, K. M. & Stein, R. B. Electrical stimulation of the human common peroneal nerve elicits lasting facilitation of cortical motor-evoked potentials. *Exp Brain Res* **153**, 366–377 (2003).

217. Khaslavskaia, S. & Sinkjaer, T. Motor cortex excitability following repetitive electrical stimulation of the common peroneal nerve depends on the voluntary drive. *Exp Brain Res* **162**, 497–502 (2005).

218. Guo, J. *et al.* Effect of electroacupuncture stimulation of hindlimb on seizure incidence and supragranular mossy fiber sprouting in a rat model of epilepsy. *The Journal of Physiological Sciences* **58**, 309–315 (2008).

219. Deffieux, T., Demené, C. & Tanter, M. Functional Ultrasound Imaging: A New Imaging Modality for Neuroscience. *Neuroscience* **474**, 110–121 (2021).

220. Group, V. N. S. S. & others. A randomized controlled trial of chronic vagus nerve stimulation for treatment of medically intractable seizures. *Neurology* **45**, 224–230 (1995).

221. Roosevelt, R. W., Smith, D. C., Clough, R. W., Jensen, R. A. & Browning, R. A. Increased extracellular concentrations of norepinephrine in cortex and hippocampus following vagus nerve stimulation in the rat. *Brain Res* **1119**, 124–132 (2006).

222. Evangelista, E. *et al.* Does the thalamo-cortical synchrony play a role in seizure termination? *Front Neurol* **6**, 192 (2015).